THE UNIVERSITY *of* EDINBURGH

Design, Modelling and Fabrication of Micro-Scale Electrode Arrays (MEAs) for Micro-Bioimpedance Tomography

Nadira Jamil

Thesis submitted for the degree of Doctor of Philosophy

The University of Edinburgh

2019

Abstract

This research involves the design and fabrication of micro-scale electrodes and optimisation of image reconstruction techniques. It aims to explore the use of bioimpedance tomography techniques in extracting some structured information on three-dimensional (3D) cell growth for the purpose of identifying cancer development, such as, cancer cell spheroids. Electrical impedance tomography (EIT) is a non-invasive imaging technique that maps the variation in conductivity of a sample, in the form of two or three dimensions. This technique has been successfully used in many clinical applications, for example, in detection of breast cancer, acute stroke differentiation, detection of bleeding due to traumatic brain injury, and detection of bacterial infection during surgery. The capability of EIT to spatially map biological development process enables it to be used in monitoring cell growth in three-dimensional formation. The work presented in this thesis includes miniaturising the electrode designs from a millimetre-scale on a PCB to a micrometre-scale on a glass substrate, and on a flexible material. Apart from the fabrication and experimental work, sensitivity analysis was performed using COMSOL Multiphysics® modelling. The final electrode design, the flexible micro-scale electrode array (Flex-MEA), is fabricated on a flexible printed circuit board (PCB). The development of Flex-MEA technology with improved imaging reconstruction on micro-scale has produced an improved high-throughput and showed great potential as a research aid in drug discovery. The research has proven that Flex-MEA enables improved electrode arrangement compared with planar Pt electrodes making it a superior choice as a portable, non-invasive technique to image the growth of microbial cultures.

Successful measurements of cell growth and proliferation propounded by this research will have a definite potential not only in the biomedical field, example, in therapeutic drug monitoring, but also in bioprocessing technology.

Declaration of Authorship

I declare that this thesis has been composed solely by myself and that it has not been submitted, in whole or in part, in any previous application for a degree. Except where stated otherwise by reference or acknowledgement, the work presented is entirely my own.

Nadira Jamil

27/05/2019

Acknowledgements

In the name of Allah, the most merciful and master of all knowledge. My deepest gratitude and love belong to my parents, Jamil Hashim and Siti Ainon Shukor, who have provided me with moral and emotional support throughout my life.

Extraordinary gratitude goes to my supervisors; Dr Stewart Smith, Professor Alan Murray and Professor Anthony Walton for their assistance, guidance, help and the time they have provided me throughout my study. With a special mention to Mr Iain Gold, Mr Kevin Tierney, Mr Mark Mason and Mr Steven Gourlay from the electronics and mechanical workshops, Mr Stewart Ramsay, Mr Richard Blair, and Mr Ewan Macdonald for the electrodes microfabrication. Not forgetting, thank you to all the people with whom I have worked with over the past four years; Dr Andreas Tsiamis, Dr Vlastimil Srsen, Dr Yunjie Yang, Dr Eva González-Fernández, Dr Camelia Dunare, Dr Wesam Gamal, Dr Ewen Blair, Dr Pierre Bagnaninchi, Dr Jiabin Jia, Dr Carol Ward, colleagues from Stokes Research Group, especially Dr Anthony Buchoux and Mr Stephen Mahon, and Miss Diane Reid. I am profoundly grateful to Professor Salter who expressed his interest in the research at the School of Engineering Postgraduate Conference three years ago (April 2016) and his wife, Professor Margaret Donaldson, for their invaluable ideas and time.

I am also thankful to my sister, Nadia Jamil and best friend, Nurulhusna Md Jan. Thank you for your love, patience, advice and support, and to my lovely friends who patiently listen to my rants, Dr Asaad Al-Masha'al, Jennifer Dodoo, Karina

Jeronimo, Dr Hanning Mai, and Dr Atif Syed. This research would have been impossible without the financial support of EPSRC (EP/K034510/1) IMPACT programme grant for funding this research, and People's Trust Council of Malaysia (Majlis Amanah Rakyat, Malaysia) for funding my PhD study.

Finally, last but by no means least, to everyone in the Scottish Microelectronics Centre, Chemistry, Division of Pathology in Western General Hospital Edinburgh, and Alrick/Becomin labs, it was fantastic sharing cleanroom and laboratory facilities with all of you during the last four years!

Thank you for all your inspirations. May this research work benefit all.

Contents

Nomenclature **vii**

Abbreviations **x**

List of Figures **xii**

List of Tables **xx**

1 Introduction **1**

1.1 Thesis Motivation 2

1.2 Problem Statement 2

1.3 Thesis Objectives 3

1.4 Thesis Structure 4

1.5 Contribution to Knowledge 5

2 Mammalian cells: An overview and applications in the biopharmaceutical industry 6

2.1 Introduction 6

2.2 Importance of cell culture 9

2.3 Basics of cancer 10

2.4 Disease models 13

2.4.1 The 3Rs concept 13

2.4.2 New drug discoveries 13

2.5 3D cell culture versus 2D cell culture 14

2.6 The applications of cell spheroids 18

2.6.1 The use of spheroids in cancer research 18

2.6.2 Tissue culture and engineering 19

2.6.3 Vaccines 20

2.7 Tissue culture techniques protocol 20

2.7.1 Culturing adherent cells 21

2.7.2 Maintaining cells in culture media 22

2.7.3 Manipulation of cultured cells 23

2.8 Summary 25

3 Electrical Impedance Tomography (EIT) in biomedical and clinical applications 26

3.1 Introduction 26

3.2 Historical background of EIT 28

3.3 Biomedical and clinical applications of EIT 29

3.4 Theory 32

3.4.1 Electrical Impedance Tomography (EIT) 32

3.4.2 Measurement techniques 32

3.4.3 Image reconstruction techniques 39

3.5 Summary 43

4 Finite Element Modelling (FEM) of micro-scale electrodes 44

4.1 Introduction 44

4.2 Motivation of Modelling and Simulation 45

4.3 Simulation models 46

4.3.1 Micro-scale electrode morphologies 46

4.3.2 Simulation setup 47

4.4 Summary 56

5 Electrode design and fabrication for micro-bioimpedance tomography 57

5.1 Introduction 57

5.2 Electrodes design on a PCB 57

5.2.1 Electrode design on EAGLE version 7.6.0 and rapid prototyping to produce Cu electrodes 58

5.2.2 Nickel (Ni) and Au electroplating for biocompatible electrodes . . 60

5.2.3 Aims of plating the electrode tips 62

5.2.4 Electroplating 63

5.2.5 Au plating 65

5.2.6 Limitations of electrodes on PCB 68

5.3 Micro-scale electrode design on glass substrate 69

5.3.1 Micro-scale electrode fabrication techniques 69

5.3.2 PCB for Pt micro-scale electrodes connection 75

5.3.3 Biocompatibility tests on passivation materials 76

5.4 Flexible Micro-scale Electrode Arrays (Flex-MEAs) design 78

5.4.1 PCBs to EIT system adapter PCB 83

5.4.2 Fluid chamber and plate 87

5.5 Sterilisation technique 88

5.6 Summary 89

6 Micro-bioimpedance tomography measurements and analysis 91

6.1 Introduction 91

6.2 Micro-bioimpedance tomography of *in vitro* characterisation on cell spheroids on Pt electrodes 92

6.2.1 Experimental work 92

6.2.2 Regularisation methods in image reconstruction for micro-bioimpedance tomography 102

6.2.3 EIT measurements on MCF7 spheroids using Au micro-scale electrodes on glass substrate 106

6.2.4 Analysis method 108

6.2.5 EIT measurements on MCF7 spheroids using Flex-MEA 109

6.3 Micro-bioimpedance tomography on 3D microbial cultures (*Rhodococcus erythropolis*) using Flex-MEA 112

6.3.1 *R. erythropolis* cell immobilisation 115

6.3.2 EIT measurement on *R. erythropolis* 115

6.4 Summary 120

7 Conclusions and outlook **122**

7.1 Conclusions 122

7.2 Outlook 125

List of publications **127**

Bibliography **129**

Nomenclature

α	Temperature coefficient of resistance, K^{-1}
$\delta\sigma$	Conductivity change
$\delta\mathbf{V}$	Potential difference
λ	Regularisation factor
μ_r	Relative permeability
ρ	Resistivity, Ω m
σ	Conductivity, S m^{-1}
$\mathbf{I}$	Unity matrix
$\mathbf{J}$	Jacobian (sensitivity) matrix
$\mathbf{J^T}$	Transpose of Jacobian (sensitivity) matrix
$\mathbf{L}$	Second-order four connected region Laplace operator matrix
ε_r	Relative permittivity
A_w	Atomic weight
C	Capacitance, F

C_m	Cell membrane capacitance, F
d	Electrodes pitch, µm
d	Thickness of plated metal, cm
F	Faraday constant, 96485 C mol^{-1}
f	Frequency. Hz
H	Regularisation function
i	Current, A
j	Current density, mA cm^{-2}
L	Track length, µm
M	Molarity
n	Number of electrons to be transferred
Q	Total charge, C
R_B	Electrolyte bulk resistance, Ω
R_e	Extracellular resistance, Ω
R_i	Intracellular resistance, Ω
s	Interelectrode spacing, µm
T	Temperature, K
t	Time, s
V	Voltage, V

W Track width, µm

X Reactance, Ω

Abbreviations

2D Two-dimensional

3D Three-dimensional

AgCl Silver chloride

Au Gold

Cu Copper

DMEM Dulbecco's Modiffied Eagle Medium

EIT Electrical Impedance Tomography

FBS Fetal Bovine Serum

FEM Finite Element Modelling

Flex-MEA Flexible Micro-scale Electrode Array

H_2O_2 Hydrogen peroxide

H_2SO_4 Sulfuric acid

H_2SO_5 Peroxymonosulfuric acid

H_3BO_3 Boric acid

HCl Hydrochloric acid

KCl Potassium chloride

KCN Potassium cyanide

LB Lysogeny Broth

LBP Linear Back-Projection

mmpm Millimetres per minute

NaCl Sodium chloride

Ni Nickel

PBS Phosphate-Buffered Saline

PCB Printed Circuit Board

PDE Partial Differential Equation

Pt Platinum

RPM Revolutions per minute

ZIF Zero Insertion Force

List of Figures

2.1 Illustration of the structures of an animal cell [1] 8

2.2 Cancerous cells and non-cancerous cells on an underlying tissue 11

2.3 Stages of tumour development [2] 12

2.4 The biopharmaceutical research and development process from discovering a drug to getting it approved by the FDA [3] 14

2.5 Microscope image of an MCF7 spheroid 16

2.6 Cells are first cultured in a flat T25 flask [4] 22

3.1 EIT imaging of the chest using the OXBACT3 EIT system [5] 31

3.2 Reconstructed images of left: breath holding and right: breathing 31

3.3 EIT of the brain [6] 32

3.4 Illustration of EIT measurement 33

3.5 Illustration of skip-0 method with 8 electrodes [7] 36

3.6 Illustration of skip-2 method with 8 electrodes [7] 36

3.7 Equivalent circuit of the experimental set-up which include the biological system as implied by the components [8] 37

3.8 Illustration of the reactions with regards to cell polarisation where (a) signalling molecules attach to the cell membrane, (b) a membrane molecule returns to the cytoplasmic pool, (c) transmission of signals to other cells, and (d) cell migration [9] 38

3.9 Convolution kernels to approximate Gaussian-Laplace second-order derivates 41

4.1 Process of the simulation models 46

4.2 Square electrodes, length = 500 µm 46

4.3 Rectangular electrodes, length = 500 µm and width = 250 µm 47

4.4 Circular electrodes, radius = 175 µm 47

4.5 Circular electrodes, radius = 250 µm 47

4.6 Graphical representation of the boundary/domain settings in COMSOL Multiphysics® 49

4.7 Electric field in COMSOL Multiphysics® modelling 51

4.8 64 × 64 array pixels was chosen in the research for image reconstruction of micro-bioimpedance tomography 51

4.9 Electric fields for the micro-scale electrodes. Top left: circular electrodes, radius = 175 µm, top right: circular electrode, radius = 250 µm, bottom left: square electrodes, length = 500 µm, and bottom right: rectangular electrodes, length = 500 µm, width = 250 µm 53

4.10 Sensitivity distribution and simulated voltage measurements for square electrodes, length = 500 µm, rectangular electrodes, length = 500 µm and width = 250 µm, circular electrodes, radius = 175 µm, and circular electrodes, radius = 250 µm 55

4.11 Left: Configuration of two-layer 16 planar electrodes in a 30 cm height and 28 cm of diameter cylinder, right: simulation result of a two cylindrical test samples spanning the full height of the cylindrical volume [10] . . . 56

5.1 PCB design on EAGLE version 7.6.0 for EIT measurements 59

5.2 PCB fabricated using the rapid prototyping for EIT measurements . . . 59

5.3 Side view of the fluid resevoir 60

5.4 Schematic diagram of the electrochemical cell Pt/NiCl/Ag/AgCl attached to power supply and meters (or a potentiostat) for obtaining a cyclic voltammetry (CV) curve 61

5.5 Schematic diagram of the 3-electrode configuration used in the electroplating process 62

5.6 Microscopic images of Ni-plated EIT electrode designs, from left to right the dimensions are as follows: radius = 0.5 mm (circular electrodes), 1.0 mm × 0.5 mm (rectangular electrodes), 1.0 mm × 1.0 mm (square electrodes), radius = 0.25 mm (circular electrodes) 64

5.7 Chronopotentiometry of Ni electroplating for circular electrodes with radius = 0.5 mm, 1.0 mm × 0.5 mm rectangular electrodes, 1.0 mm × 1.0 mm square electrodes, and circular electrodes with radius = 0.25 mm 65

5.8 Microscopic images of Au-plated EIT electrode designs, from left to right the dimensions are as follows: radius = 0.5 mm (circular electrodes), 1.0 mm × 0.5 mm (rectangular electrodes), 1.0 mm × 1.0 mm (square electrodes), radius = 0.25 mm (circular electrodes) 66

5.9 Chronopotentiometry of Au electroplating for circular electrodes with radius = 0.5 mm, 1.0 mm × 0.5 mm rectangular electrodes, 1.0 mm × 1.0 mm square electrodes, and circular electrodes with radius = 0.25 mm 67

5.10 Experimental set-up for Au electroplating in a Faraday cage 68

5.11 Au electroplating procedure on Cu electrodes 68

5.12 Schematic cross sections illustrating the micro-scale electrode fabrication process 70

5.13 16 micro-scale electrodes with r = 250 µm circular in a ring pattern . . . 70

5.14 Microscopic images of the post-liftoff process. From left to right; 175 µm radius circular, 250 µm radius circular, 500 µm × 250 µm rectangular, and 500 µm × 500 µm square micro-scale electrodes 72

5.15 Micro-scale electrodes design on a photomask for Parylene C patterning. The red tracks are passivated with Parylene C while the areas in black are etched to create contacts when performing the EIT measurements . 73

5.16 Images of micro-scale electrodes after Parylene C etching process. From left to right; 175 µm radius circular, 250 µm radius circular, 500 µm × 250 µm rectangular, and 500 µm × 500 µm square micro-scale electrodes 74

5.17 Pt micro-scale electrodes on a glass substrate 74

5.18 The fabricated PCB for Pt micro-scale electrodes connection 75

5.19 EIT device (Pt micro-scale electrodes) directly attached on the adapter PCB 76

5.20 Optical images of cells after culturing: (left) silicon nitride (centre) silicon dioxide and (right) Parylene C 77

5.21 Trypan blue staining test results with different passivating materials to test cell viability. The error bars represent standard deviation 78

5.22 The material stack-up of a single layer flex with ZIF feature 79

5.23 The Flex-MEA design 81

5.24 Top view of the PCB 82

5.25 Bottom view of the PCB adapter PCB when placed in a fluid chamber . 83

5.26 PCB adapter PCB 84

5.27 Adapter PCB fabrication process 87

5.28 (Left): Drawing of arcrylic plate where the fluid chamber is attached at the centre of the arcrylic plate. (Right): Photo of the chamber arcrylic plate 87

5.29 Reconstructed images for the post-sterilisation test performed on ABS cube and metal disc 89

6.1 MCF7 cells at 90% confluency rate 93

6.2 MCF7 cells after the trypsinising process 94

6.3 Dead cells observed in the flask 95

6.4 Graphical representation of MCF7 spheroids culture protocol 96

6.5 Corning spheroid 96-well Corning® spheroid microplate used in the spheroids processing 96

6.6 Illustration of the spheroid formation after 48 hours 97

6.7 The MCF7 spheroid growth (in size) for three cell concentrations, 60,000 cells ml^{-1}, 120,000 cells ml^{-1} and 240,000 cells ml^{-1} over 72 hours . . . 97

6.8 Average length between different points are taken to determine the size of a non-spherical spheroid 98

6.9 Spheroid formation and growth: 60,000 cells ml^{-1} (0.43 mm), 120,000 cells ml^{-1} (0.64 mm) and 240,000 cells ml^{-1} (0.74 mm) 98

6.10 Trypan blue viability test 99

6.11 Cells proliferation with different composition of growth medium 101

6.12 (Left) Higher conductivity (Cu metal) and (right) Lower conductivity (rubber) test samples. The positions of the test samples are indicated with black rings 103

6.13 (Black) Calibration data of PBS, (red) measurement data with higher conductivity test samples, and (blue) lower conductivity test samples . . 104

6.14 Image reconstructions based on three regularisation methods, Tikhonov Regularisation, Gaussian-Laplace Regularisation and L_1 Regularisation (colour scale in Ωcm) 105

6.15 EIT imaging of MCF7 spheroids using micro-scale electrode arrays on a glass substrate 107

6.16 Triton-X effect on 0.71 mm MCF7 spheroid 108

6.17 Reconstructed images of Triton-X effect on 0.71 mm MCF7 spheroid over 85 minutes 109

6.18 Complete experimental setup representing the Flex-MEA, EIT system, display of the reconstructed images and 96-well spheroid microplate . . . 110

6.19 Measured voltage across Flex-MEA micro-scale electrodes on MCF7 cell spheroids over five different frequencies – 10 kHz, 30 kHz, 50 kHz, and 70 kHz 111

6.20 Measured voltage across PCB micro-scale electrodes on MCF7 cell spheroids with different DMSO concentrations; 10%, 50%, and 100%. The measurement was performed at 10 kHz 112

6.21 The four phases involved in bacteria growth [11] 113

6.22 *R. erythropolis* culture on day 0 where in the inset is a colony of *R. erythropolis* 114

6.23 *R. erythropolis* culture on day 3 114

6.24 The experimental set-up for EIT measurement on *R. erythropolis* 115

6.25 Location of *R. erythropolis* in the set-up and reconstructed images at 3°C 117

6.26 Location of *R. erythropolis* in the set-up and reconstructed images at 30°C 119

List of Tables

3.1 EIT measurement matrix for each pair of electrodes 34

4.1 Material properties defined in COMSOL Multiphysics® 48

5.1 Chemical composition of the Ni-plating solution 63

5.2 Electroplating set-up 66

5.3 Flex-MEA dimension 82

5.4 Resistance value of each electrode, E1 to E16 85

Chapter 1

Introduction

This research focuses on the characterisation and monitoring of cell spheroids using Electrical Impedance Tomography (EIT) to understand the behaviour and responses of cells to internal or external environmental changes. The micro-scale electrodes fabricated for this work use cell spheroids as the primary transducer to detect a change in environmental or physiological conditions. In combination with EIT, the micro-scale electrodes allow for fast, label-free, non-invasive quantitative measurements and are sensitive to any changes in the environment and cell structures. This research optimises the micro-scale electrode design to characterise and differentiate between cancerous cells and non-cancerous (healthy) cells. The outcome of this work provides a foundation for an enhanced cell spheroid analysis and characterisation, thus creating a way for earlier cancer characterisation and monitoring while minimising healthcare costs.

1.1 Thesis Motivation

Early cancer diagnosis and treatment are the primary concerns throughout the world. In 2012, 1.7 million new cases of breast cancer were diagnosed worldwide making this disease one of the most common type of cancer among women [12]. The survival rate is slightly higher in developed countries (75%) compared to patients in less developed countries (65%) [12]. The enormity of cancer-related deaths is a result of late diagnosis and the fact that cancer is a very challenging disease to be treated due to the non-uniform nature of a cancerous tumour. None of the cancer types has similar malignant or invasive potential. Thus, clinicians need to treat them uniquely [13].

It is essential to have a set of device and measurement techniques with enhanced spatial resolution and high sensitivity. The development of a cost-effective and real-time imaging system is vital in acquiring high fidelity images of cancer spheroids, which involves the study of cell spheroids in image reconstructions of EIT. This research investigates methods to improve cancerous tumour detection and provide information concerning cell spheroid characteristics through designing micro-scale electrodes and optimising the image reconstruction techniques. It has a high potential for pharmaceutical drug testing and could potentially assist the process of discovering new medications to treat cancer.

1.2 Problem Statement

Successful development of the micro-scale electrodes for EIT will provide a means of reconstructing images that differentiate non-cancerous cells and cancerous cells, other

than quantifying biocompability studies. Anti-cancer drugs, like chemotherapy drugs, require thorough characterisation and validation before they can be used clinically.

Methods like observation through inverted biological microscopes typically used for observing organisms in a transparent flask and mass spectrometry imaging require the cell spheroids to either be fixed or sliced before measurements and imaging to validate the drugs. These methods are time-consuming and not being performed on living cells.

Real-time EIT can be used to improve qualitative measurements by identifying specific time frames and drug concentrations, hence, eliminating redundant experimental trials. Continuous EIT can capture the reactions of the cells towards an anti-cancer drug at several points in time. Therefore, when a reaction is observed, quantitative measurements are being performed at the specific time to probe for more information. Apart from that, it also helps in obtaining fundamental information regarding cellular responses and behaviour.

Repeatability, accuracy and spatial resolution are essential in successfully implementing the image reconstruction of EIT of cell spheroids for cytotoxicity tests. Thus, this research aims to address these problems through micro-scale electrode design optimisation, fabrication of 16-electrode arrays, and analysis of reconstructed images from EIT experiments.

1.3 Thesis Objectives

This project is set out to explore the hypothesis that electrodes on the micrometre-scale can, by obtaining relevant electrical properties of a cancer spheroid:

(1) develop a Flexible Micro-scale Electrode Array for cancer cell detection,

(2) analyse the characteristics and modelling of cancer cell spheroids conductivity in Flex-MEA, and

(3) evaluate the effectiveness of Flex-MEA in cancer cell detection and anti-cancer drug efficacy.

1.4 Thesis Structure

Chapter 2 of the thesis provides background information on mammalian cells, the difference between a Two-dimensional (2D) and Three-dimensional (3D) cell culture, the applications of cell spheroids in the biopharmaceutical field and the cell culturing protocol.

Chapter 3 describes the applications of EIT in biomedical practice including measurement and image reconstruction techniques.

Chapter 4 defines the primary method implemented in realising this research that is Finite Element Modelling (FEM) and simulations where the micro-scale electrode designs are simulated to determine the most sensitive micro-scale electrodes. It also describes the measurement patterns of an EIT technique.

Chapters 5 and 6 explore the design of biocompatible electrodes and presents biocompatibility tests on passivating materials. The electrodes were initially fabricated on a Printed Circuit Board then scaled down to micro-scale electrodes on glass substrates and flexible material. These chapters also describe the EIT experiments for *in vitro* characterisation performed on mammalian cell spheroids and 3D microbial cultures.

In Chapter 7, conclusions, future developments and outlook of this research are discussed.

1.5 Contribution to Knowledge

The contribution to the knowledge of this research was both in electronics and biomedical applications. It further progressed the on-going investigation in the field of bioengineering and drug discovery.

The novelty of the research was the implementation of EIT for image reconstruction in microscale. The Flexible Micro-scale Electrode Array was placed in a Corning® spheroid 96 well microplates enabling real-time monitoring of the MCF7 spheroids. The Flex-MEA technology developed when integrated with improved image reconstruction technique on micro-scale gives high throughput in basic research which aids in drug discovery.

The outcomes of this research, which include the measurement of cell growth and proliferation, and influence of resistance variation towards image reconstruction, are valuable in monitoring the effectiveness of anti-cancer drug therapies. It has potential impact in pharmaceutical and biomedical engineering particularly in therapeutic drug development.

Chapter 2

Mammalian cells: An overview and applications in the biopharmaceutical industry

2.1 Introduction

The method of growing cells under controlled conditions, generally outside of their natural environment is called cell culturing. Although cell culture conditions vary for each cell type, artificial environments mimicking the natural environment consist of a suitable flask containing "culture medium", an aqueous solution, that supplies amino acids, carbohydrates, vitamins and minerals, which are the essential nutrients for cell growth and proliferation. The culture medium also provides growth factors, hormones, and dissolved gases such as carbon dioxide and oxygen [14]. The culture medium normalises the physical and chemical environment which are the pH buffer, osmotic

pressure, and temperature. Depending on the cell type, cells require a surface to attach to for adherent or monolayer type of culture, or they grow free floating in the culture medium, known as a suspension culture.

All living things are composed of at least one cell [15]. Cell biology is a study of cell structure and its function, which involves the concept that cells are the basic unit of living things [16]. Cells make up the entire human body, and in each cell, there is a set of instructions, the deoxyribonucleic acid (DNA), that instructs the cell when to reproduce and die [17].

Cell is the smallest structural and functional unit of all living things [18]. Cells are made from nucleic acids that help expressing the genetic code, proteins, carbohydrates, and lipids which are the components of cell membranes [19]. Figure 2.1 illustrates the structures of an animal cell composing of nucleus, cytoplasm, cell membrane, DNA, mitochondrion, endoplasmatic reticulum, lysosome, ribosome, and Golgi apparatus.

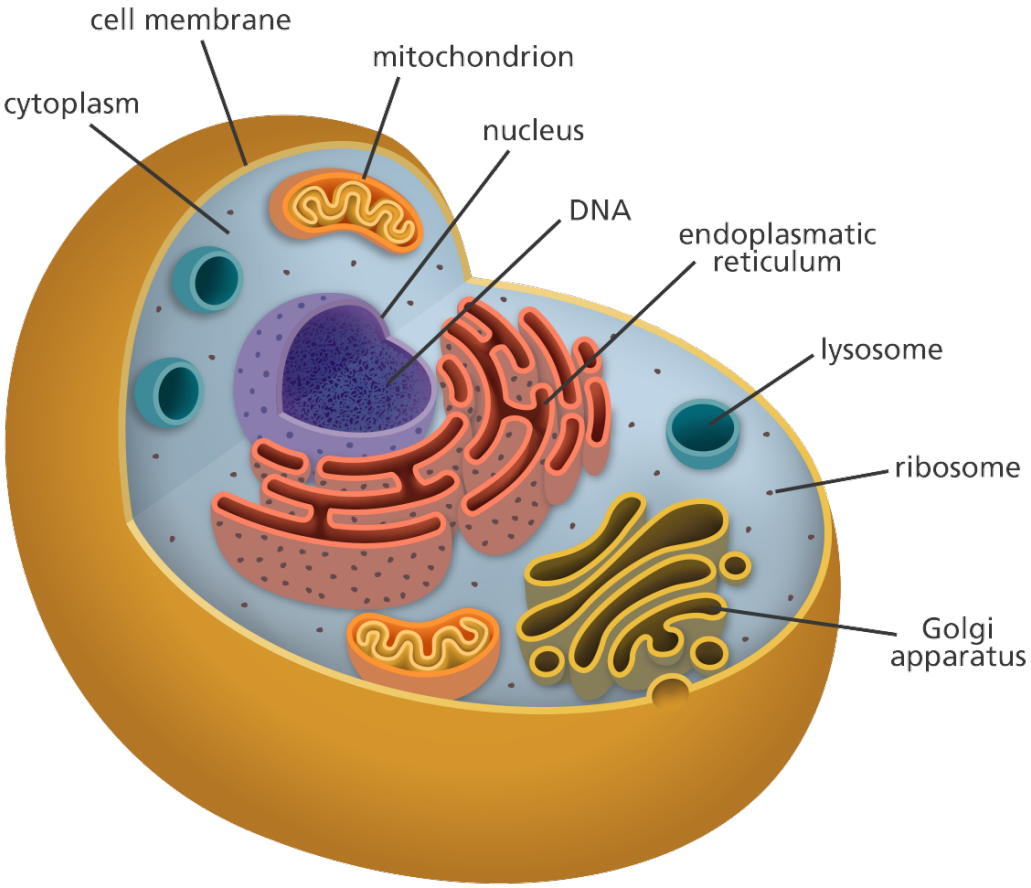

Figure 2.1: Illustration of the structures of an animal cell [1]

Since the human embryonic stem cells (hESCs) are proven for drug and toxicity screening and the human stem cell models complement conventional animal models, its implementation reduces costs and the use of animal models in drug discovery [20]. Cellular models have been used to study the therapeutics in neurodegenerative disorders [21], develop antiatherosclerotic therapy [22], and perform drug screening for toxicity assessments [23].

2.2 Importance of cell culture

Research in tissue engineering, stem cells and molecular biology primarily involves culturing cells on flat plastic or glass dishes. From today's advances of polymer technology, the standard plastic dish for 2D cell culture commonly used in the laboratory. This is known as the Petri dish, with its name being taken from Julius Richard Petri, a German bacteriologist [24]. Many researchers today also culture cells in laboratory flasks, conical flasks, and disposable bags like those used in single-use bioreactors. Other than Petri dishes, scientists have long been growing cells within biologically derived matrices such as collagen or fibrin, and more recently, on synthetic hydrogels such as polyacrylamide or polyethylene glycol (PEG) [25].

Cell culture in three dimensions has been called "Biology's New Dimension" by Alison Abbott [26]. At present, the practice of cell culture remains based on varying combinations of single or multiple cell structures in 2D [27]. Currently, there is an increase in the use of Three-dimensional (3D) cell cultures in research areas not limited to drug discovery, cancer biology, regenerative medicine and fundamental life science research. There are a variety of platforms used to facilitate the growth of 3D cellular structures including scaffold systems such as hydrogel matrices [28], solid scaffolds, scaffold-free systems such as low adhesion plates, nanoparticle facilitated magnetic levitation [29] and hanging drop plates [30].

As the natural extracellular matrix (ECM) is vital in the survival, proliferation, differentiation and migration of cells, different hydrogel culture matrices mimicking natural ECM structures are potential approaches to *in vivo* like cell culturing [25]. Hydrogels are made from polymers [31] or natural source for example, agarose [32].

They are composed of interconnected pores with high water retention, which enables efficient transport of substances such as nutrients and gases.

The 3D cell culturing using the magnetic levitation method (MLM) is a technique of growing 3D tissue by inducing cells treated with magnetic nanoparticle assemblies in spatially fluctuating magnetic fields. By applying neodymium magnetic drivers, this technique promotes cell to cell interactions by levitating the cells up to the air or liquid interface of a standard Petri dish [33]. The magnetic nanoparticle assemblies consist of a blend of magnetic iron oxide nanoparticles, Gold (Au) nanoparticles, and the polymer polylysine. 3D cell culturing is scalable, with the capability to culture 500 to millions of cells using single dish to high-throughput low volume systems.

One of the most common methods of creating 3D cell cultures is to process them into spheroids. 2D cells are cultured until they are 90% confluent before spheroid processing in round-bottom ultra low-adhesion plates. With the intention to allow cells to form aggregates in suspension, the cells need to be cultured in a condition, which prevents them from adhering to a solid surface. Commercial round-bottom well plates with low attachment surfaces for single spheroid production per well are available from Corning® and the cell concentration determines the processed spheroid size [34].

2.3 Basics of cancer

Cancer begins when a healthy cell becomes damaged and starts to multiply out of control. Cancer cells become less dependent on signals from other cells, making them resistant to the controls that maintain the growth and death of normal cells [35]. Figure

2.2 shows the difference between cancerous and non-cancerous cells on an underlying tissue.

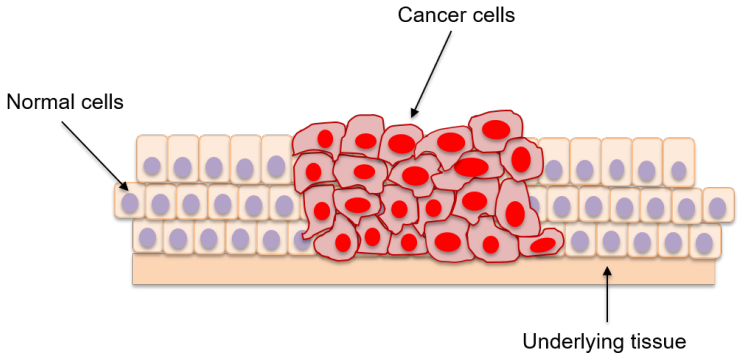

Figure 2.2: Cancerous cells and non-cancerous cells on an underlying tissue

There are various types of cancer. Cancer can begin in any parts of the body; lungs, breasts, colon, as well as blood. Cancers are similar in many ways, but they have their own particular method of growing and spreading [36]. Figure 2.3 shows the development of cancer, which happens when a single mutated cell proliferates abnormally and multiplies that result in progression of the tumour [2].

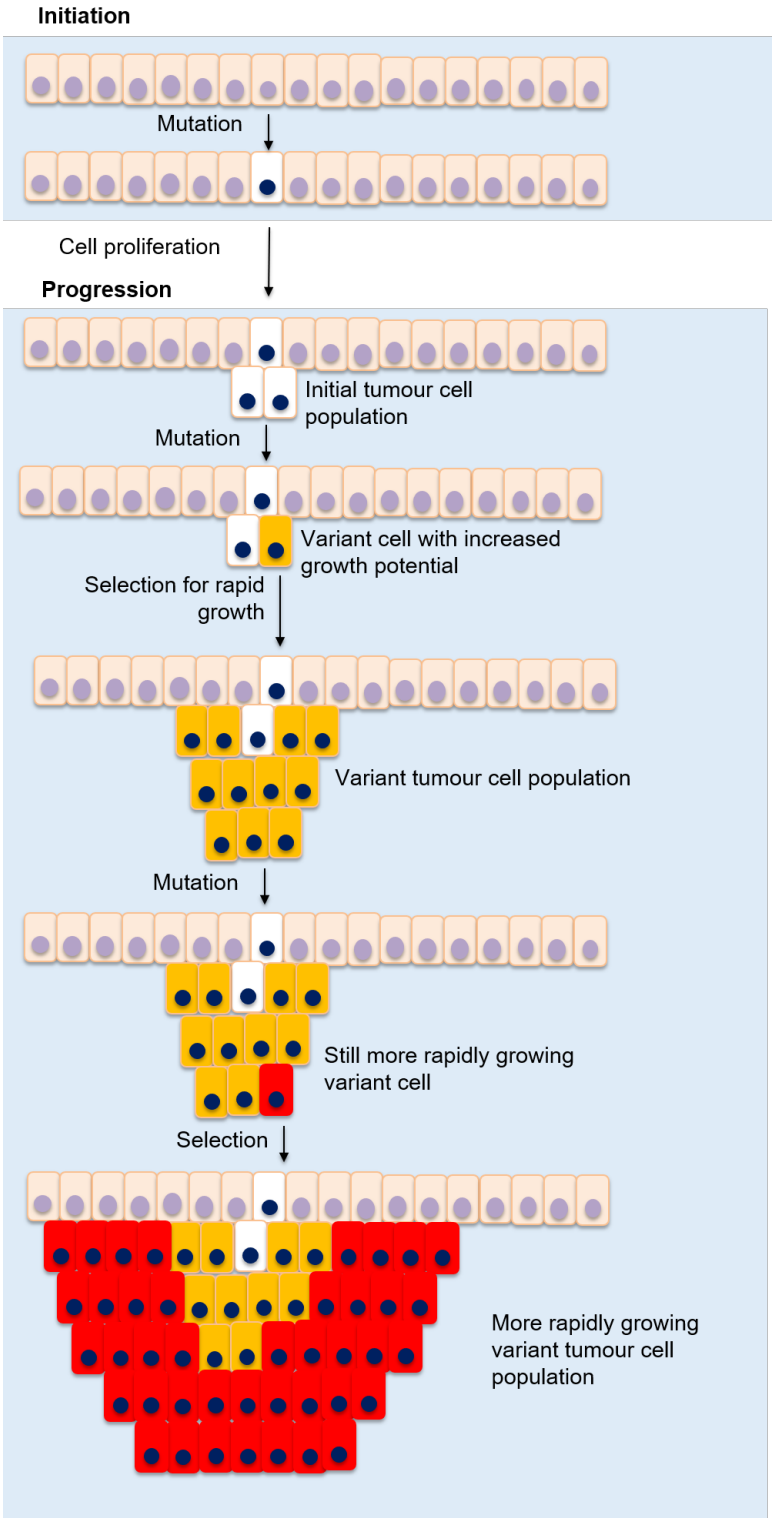

Figure 2.3: Stages of tumour development [2]

2.4 Disease models

Disease models are a collection of cells that can be used as a model of an actual human or animal disease [37] which are a vital implementation in understanding the mechanisms that encourage the progression of a disease and aiding in developing novel therapies. Transgenic animals or transformed cell lines are usually used in a disease model [38].

2.4.1 The 3Rs concept

The term "3Rs" refers to replacement, reduction, and refinement of the use of animals in scientific research [39]. This concept is a robust framework to minimise the use and suffering of animals and to deal with the harm to animals. This concept reduces animal suffering and leads to efficient scientific research [40]. According to the United Kingdom's national organisation for the 3Rs, the National Centre for the Replacement Refinement and Reduction of Animals in Research (NC3Rs), the standard definitions are described as:

- Methods which avoid or replace the use of animals in research (*Replacement*),
- methods which minimise the number of animals used per experiment (*Reduction*), and
- methods which minimise animal suffering and improve welfare (*Refinement*). [41]

2.4.2 New drug discoveries

Drug discovery is the procedure of finding new drugs and introducing them to the market for patients or clinicians [42]. The drug development and drug discovery process

involves target validation, finding the right potential drug to interact with the selected targets, performing laboratory and clinical trials on the new compound to ensure its safety and effectiveness, and finally attaining approval for new drugs to be used as new therapies [43].

Figure 2.4 illustrates the development process in biopharmaceutical research [3]. This is a time-consuming process consisting of pre-clinical research and clinical trials that involve not a small number of volunteers but thousands of volunteers and chemical entities to deliver a single Food and Drug Administration (FDA) approved medicine.

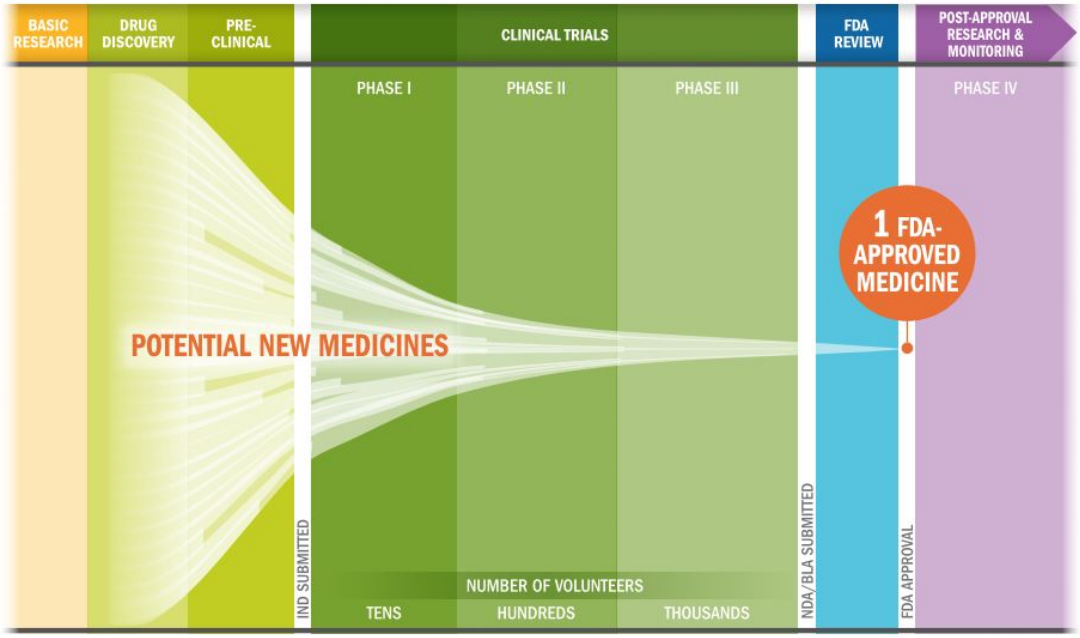

Figure 2.4: The biopharmaceutical research and development process from discovering a drug to getting it approved by the FDA [3]

2.5 3D cell culture versus 2D cell culture

It has been well known for over thirty years that cells grown using a 3D cell culture technique are the most appropriate representation of natural tissues and organs when

compared with cells grown in 2D environment. In a 2D cell culture, cells are grown on flat dishes made of synthetic polystyrene plastic that is very stiff surface. The cells adhere and spread on this plastic surface and form unnatural cell attachments to proteins that are deposited and denatured on the synthetic surface [44].

In 3D cell culture, cells attach to one another and form natural cell-to-cell attachments. They are flexible and elastic like real tissues. Cells are typically surrounded by a matrix of complex proteins in their native configuration, and this provides important biological instructions to the cells. In a 3D cell culture environment, cells can exert forces on one another, and move and migrate as they do *in vivo*. These cell-cell interactions in 3D cultures also include gap junctions, which directly couple one cell to another.

Gap junctions are much more common in 3D than 2D cell cultures. They enable cells to communicate with one another through exchanging ions, small molecules and electrical currents. The proximity of cells in a 3D environment enables surface adhesion molecules and surface receptors on one cell to bind to similar features on an adjacent cell [45]. This coupling in the 3D environment also maximises the cell-cell communication and signalling that is critical for cell function [46]. The phenotype of cells grown in 3D is more complicated and exhibits more physiological relevance to natural tissues than is the case with 2D cells. For instance, liver cells perform liver organ functions in 3D cell culture where as 2D cell culture do not. Cartilage cells form more differentiated cartilage tissue in 3D cell culture compared with 2D cell culture, and the cell type continues with almost all cells of organs and tissues. A scaffold-based 3D culture is commonly used for tissue regeneration of the bone, cartilage, skin, vascular or skeletal muscle [47].

A tumour spheroid has a necrotic core, a quiescent zone which slowly proliferates

or does not proliferate depending on the availability of nutrients and oxygen, and a proliferating zone, where the cells rapidly growing. Figure 2.5 is a microscope image of an MCF7 spheroid which shows the necrotic core, proliferating and quiescent zones.

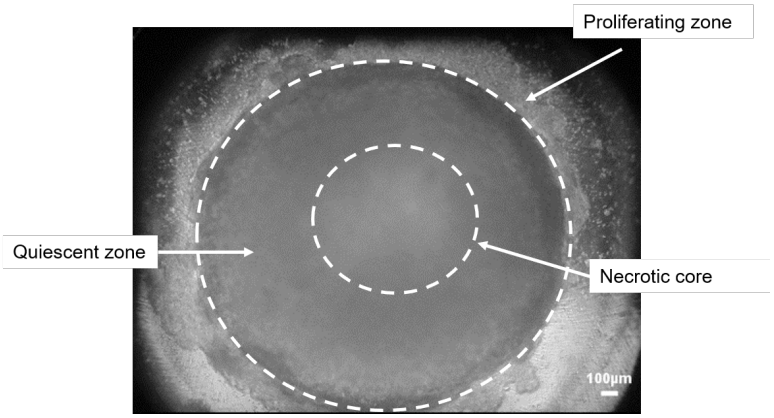

Figure 2.5: Microscope image of an MCF7 spheroid

The benefits of 3D compared with 2D cell culture also manifest when mimicking pathological conditions such as cancer. For example, breast cancer cells grown in a 2D environment can quickly be killed by low doses of chemotherapeutic drugs or low doses of radiation, making them less efficient for drug testing research. If the same cells are processed in a 3D cell culture, they are resistant to the same doses of chemotherapeutic drugs or radiation, precisely like cancerous tumours found in the body. Hence, cells grown in 3D are more valid targets for testing and discovering new drugs to treat cancer.

Another benefit of testing drugs in 3D cell culture is that 3D cells form multi-layers of cells. In contrast, 2D cells form a monolayer of cells that are thinly spread on a plastic surface. When performing drug testing on 2D cells, the drug diffuses a short distance across the cell membrane to reach its intended target while for 3D cells, the situation is more realistic and a drug needs to diffuse across multiple layers of cells to reach the cells on the inside of a microtissue [48]. The diffusion across multi-layers of cells mimics

the challenges found in the human body or in a cancerous tumour where a drug needs to diffuse through many layers of cells and extracellular matrix (ECM) before it reaches its intended target [49]. Moreover, cells grown in the 3D environment will form natural barriers to drugs such as tight junctions that bind cells tightly together and slow down the diffusion of drugs, thus making this a more realistic test.

It has been well established that cells processed into spheroids are much more representative of the *in vivo* environment than 2D cell cultures. The multicellular arrangement allows cells to interact with each other and the ECM provides a better understanding of cellular complexities. Cancer and stem cell research are mainly focused on areas where spheroids have substantial potential compared to 2D cell cultures.

In the 1980s Mina Bissell led a research group in Lawrence Berkeley National Laboratory [50] which developed 3D culture techniques for *in vivo* models. Bissell highlighted the importance of the ECM, its effects on gene expression and subsequent effects on neighbouring cells, along with the crucial role of the microenvironment [51]. This research study has led to the rise of 3D cell culture over monolayer culture techniques, and spheroids have become a standard tool for a range of applications, from studying complex malignant tissues to therapeutics research.

Advanced techniques now permit researchers to study spheroids, sub-populations, and individual cells in a colony. Spheroids first need to be generated, and this is where careful attention must be paid to achieving an optimal culture environment. In addition to the ECM, there are a number of other factors to control, including temperature, pH and carbon dioxide, which can determine the viability and reproducibility of spheroid generation [52]. Previous studies have identified ideal hypoxic conditions, and the range

of specialised culture equipment and synthetic coatings that are now available have made spheroid research increasingly accessible and versatile.

While previous research has set down the foundations of spheroid studies, the future of the research area is likely to span across multiple clinical and research applications. In particular, since spheroids can model tumours, it allows researchers to evolve more robust drug discovery initiatives, which help to improve the understanding of cancer treatments.

2.6 The applications of cell spheroids

2.6.1 The use of spheroids in cancer research

Cancer is one of the diseases most widely studied, but it continues to puzzle researchers. The complex nature and behaviour of cancer cells make them very difficult to study. Nevertheless, in present years, a multicellular tumour spheroid (MCTS) model has commonly been adopted in cancer biology. The MCTS models provide an accurate representation of the physiology of tumours, which gradually making an essential contribution to our understanding of cancer biology [53].

Spheroids have numerous structural, functional and physiological resemblances to tumours *in vivo*. Spheroids and tumours are both made up of heterogeneous cells and have similar secretory and metabolic activity [54]. The environment in a 3D cell culture exposes cells, enabling them to communicate with each other and their surroundings, providing an optimal environment for the cells to respond in a similar manner to those in a tumour [53]. Within such a representative environment, spheroids can express chemical

gradients that is the difference in ions' concentration across a membrane of the various nutrients, oxygen and catabolites (a product of catabolism that breaks down complex molecules into smaller molecules as part of the metabolism [55] found in a tumour, that can aid drug development.

One of the most defining features of a tumour is its hypoxic core, as researchers believe it is the reason for the failure of cancer drugs and treatments. This can be replicated in spheroids [53]. As a tumour grows, the cells will often run out of adequate blood supply, leaving the centre of a tumour with a low concentration of oxygen and nutrients. In addition to this, the reproducibility and reliability of the developed spheroid culture systems facilitates its adoption in cancer research.

2.6.2 Tissue culture and engineering

Cell culture is an essential component of tissue culture and tissue engineering. It forms the basics of growing and maintaining cells *in vitro*. The primary application of human cell culture is in the stem cell industry, where mesenchymal stem cells can be cultured and frozen in vials (cryopreservation) for future use. Tissue engineering potentially offers vast improvements in low-cost medical care for hundreds of thousands of patients annually [56]. It involves culturing and growing cells in scaffolds, so, a non-invasive and real-time monitoring of 3D cell culture will aid in monitoring the tissue growth in scaffold-based tissue-engineered constructs.

2.6.3 Vaccines

Vaccines for diseases like polio, measles, mumps, rubella, and chickenpox are produced in cell cultures [57]. Novel ideas in the field of vaccines include recombinant DNA-based vaccines, such as one made using human adenovirus that is a common cold virus as a novel adjuvant [58] [59]. The discovery of new vaccines require careful assessments from testing, licensing and monitoring [60]. A real-time non-destructive monitoring technique of 3D cultures would be able to decrease the time taken for a vaccine to pass through the stages prior to being licensed for use.

2.7 Tissue culture techniques protocol

There are three types of cell cultures; primary cells cultures, secondary cell cultures and cell lines [61]. Primary cell cultures happen when the cells are isolated from the tissue and proliferated until they reach confluence. When a primary cell culture is subcultured, it is then known as a secondary cell culture. Subcultures or passages are formed by transferring the cells from one culture vessel or flask, to the other [62]. A cell line can be either finite or continuous depending on its lifespan in culture: whether it is limited or immortal [61].

Adherent cells and suspension cells are the two types of the primary cell cultures. Cells grow in a monolayer attached to the surface of a tissue culture dish or flask is known as adherent cells. The cell growth is limited by the surface area of the culture dish or flask on which the cells are proliferating. Since the adherent cells are attached to the surface, the cells are dissociated through trypsinisation. Suspension cells do not

attach to the surface but instead, the cells grow floating in the culture medium and the cell growth is limited by the concentration of cells. The suspension cells do not need any enzymatic dissociation as they are free floating in the culture medium. Cell lines derived from solid tissue classified as epithelial, endothelial, fibroblast and neuronal are adherent cell lines while cell lines derived from blood are suspension cell lines [63].

2.7.1 Culturing adherent cells

The technique of detaching confluent adherent cells from the vessel surface is known as passaging the cells or trypsinising. Trypsinisation cut the bond between the cell and the surface so that the cells no-longer adhere to the surface [64]. Mechanical scraping may also be required to fully detach cells.

Plating density is the number of cells per volume of culture medium when adding them to a cell culture vessel. It plays a critical role in the function of some cell types. For example, a lower plating density makes granulosa cells exhibit estrogen production [65], while a higher plating density makes them appear as progesterone-producing theca lutein cells [66]. Cells can grow either in suspension or adherent cultures [67]. Some cells naturally live in suspension such as cells in the bloodstream, which are clearly not attached to a surface. Likewise, there are cell lines that have been adapted to be able to survive in suspension cultures so they can multiply to a higher density than adherent conditions would allow [68].

Adherent cells need a surface, such as a tissue culture flask coated with an extracellular matrix component. The extracellular matrix components such as collagen or laminin increase the adhesion properties and provide other signals required for growth

and differentiation [69]. Most cells derived from solid tissues are adherent. An alternative type of adherent culture is organotypic culture [70], which involves growing cells in a 3D environment as opposed to 2D culture dishes. This 3D culture system is biochemically and physiologically more similar to *in vivo* tissue [68] but is technically challenging to maintain because of many factors, one of the examples, diffusion [71].

2.7.2 Maintaining cells in culture media

Most of the isolated primary cells undergo the process of senescence, and they stop dividing after a certain number of population doublings while retaining their viability [72]. This process is described as the Hayflick limit [73]. Cells are typically grown and maintained in a flask such as that shown in figure 2.6. This is maintained at an appropriate temperature and gas condition; 37°C, 5% CO_2 for mammalian cells in an incubator. Culture conditions vary for every individual cell type, and variation of conditions for a particular cell type can result in different phenotypes [74].

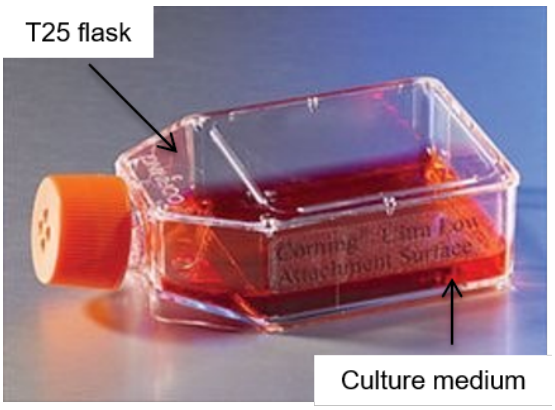

Figure 2.6: Cells are first cultured in a flat T25 flask [4]

2.7.2.1 Growth conditions

Aside from pH, temperature and dissolved gas concentrations, the most common varied factor in culture systems is the cell growth medium. Every cell growth medium recipe has different values in pH, glucose concentration, growth factors and the presence of other essential nutrients. The growth factors are often derived from the serum of animal blood, such as fetal bovine serum (FBS) [75], fetal calf serum (FCS), equine serum, and porcine serum [76] to supplement the media.

2.7.3 Manipulation of cultured cells

The common manipulations carried out on cultured cells are media changes, passaging cells, and transfecting cells. These actions are performed using tissue culture methods that rely on the aseptic technique. The aseptic technique aims to avoid contamination by bacteria, yeast, or other cell lines [68]. Manipulations are typically carried out in a sterile laminar flow cabinet to eliminate contaminating micro-organisms. Antibiotics such penicillin and streptomycin as well as antifungals are added to the growth media depending on the cell type [77]. As cells undergo metabolic processes, acid is produced and the pH decreases. Hence, a pH indicator is added to the medium for nutrient depletion measurement [68]. It is usually colourimetric and the culture medium in figure 2.6 will change its colour when nutrients in the media are depleted.

2.7.3.1 Cell passaging

Cell passaging, also known as subculturing, involves transferring a small number of cells into a new vessel [78]. If cells are regularly split, they can be cultured for a

longer time as it avoids the senescence-associated with prolonged high cell density [79]. Suspension cultures are easily subcultured with a small amount of culture containing few cells diluted in a larger volume of fresh media. For adherent cultures, cells need to be detached, and it is commonly performed with 0.25% w/v trypsin-EDTA [64] to dissociate the cells. A small number of detached cells can be used to seed new cell cultures [67].

2.7.3.2 Transfection and transduction

Another conventional method for manipulating cells involves the introduction of foreign DNA by transfection [80]. It is regularly performed to cause cells to express a gene of interest. More recently, the transfection of ribonucleic acid interference (RNAi) constructs has been realised as a convenient mechanism for suppressing the expression of a particular gene or protein. DNA can also be inserted into cells using viruses, in methods referred to as transduction [81], infection or transformation. Viruses such as parasitic agents are well suited to introduce DNA into cells, as this is a part of their regular course of reproduction.

2.7.3.3 Cell storage

Cell lines in continuous culture are susceptible to genetic drift while finite cell lines are fated for senescence [74] and cell cultures are susceptible to microbial contamination [82]. Since the replacement of an established cell line is time-consuming and it is a valuable resource, it is critical to freeze them down and preserve for long-term storage [74].

Once a small excess of cells becomes available from subculturing, they should be

frozen. The frozen cells will be the seed stock, protected, and not be made available for general laboratory use [83]. Working stocks can be prepared and replenished from frozen seed stocks [74]. If the seed stocks become depleted, cryopreserved working stocks can then serve as a source for preparing a fresh seed stock with a minimum increase in generation number from the initial freezing [84].

The ideal way for cryopreserving cultured cells is keeping them in liquid nitrogen in a complete medium with a cryoprotective agent such as dimethylsulfoxide (DMSO) [74]. Cryoprotective agents lessen the freezing point of the medium and also allow a slower cooling rate, substantially reducing the risk of ice crystal formation which can damage the cells and cause cell death [85]. The typical temperature for cryopreservation of mammalian cells is -80°C.

2.8 Summary

Mammalian cell culture plays a vital role in research and development of new drugs and is a heavy element in improving the quality of health and life of patients suffering from life-threatening diseases such as cancer and genetic disorders. In fighting diseases, new therapies or drug treatments are developed. When a new drug treatment is discovered, it needs to be tested before bringing it to the market. A 3D cell spheroid represents more physiologically relevant systems compared to 2D cell culture. Hence, cell spheroids exhibit high potential for pharmaceutical drug testing.

This research is proposing a technique to avoid the implementation of animal testing in an experiment. The technique also introduces a more time and cost-effective procedure in the research and and development new drugs discoveries.

Chapter 3

Electrical Impedance Tomography (EIT) in biomedical and clinical applications

3.1 Introduction

Electrical properties such as the conductivity and permittivity determine the behaviour of materials under the influence of external electric fields. Conductive materials have a high electrical conductivity relative to the electrical current flow through a material, which enables both direct and alternating currents to flow smoothly through them. In contrast to that, dielectric (insulator) materials have a low conductivity.

Electrochemical impedance spectroscopy (EIS) has been known as a non-invasive characterisation technique of tissue change [86] which can be used to analyse electrical

processes occurring in a system. The technique is sensitive to changes in both surface and bulk effects, which makes it a valuable technique for electrochemical research and sensor applications. A reversible reaction at the working electrode is formed where both the oxidised and reduced species are soluble in the aqueous solution at the electrode. A complex impedance plot can be obtained by applying an alternating current to the electrochemical cell.

In 1999, H.P. Schwan [87] published a historical overview on the application of impedance measurement in biology. This technique began in 1911 when it was first shown that erythrocytes (red blood cells) have an impedance that varies with frequency due to the presence of cell membranes. The growth and activity of a cell, changes in its structure, shape and location have all been monitored or measured in biosensors using microelectrodes [88] where impedance characteristics of cultured cells are being examined over a period of time.

An electrochemical sensing electrode is a transducer that converts between an electric current in a wire to an ionic current in an electrolyte, i.e. tissue, and vice versa. When designing and fabricating electrodes, it is crucial to consider the size and the material used [89]. Stainless steel is a typical electrode material in dye-sensitised solar cells (DSSCs) since it is resistant to corrosion [90]. Since Au is a biocompatible material [91], Au-plated electrodes were implemented in a non-invasive bioimpedance monitoring process of 3D cell culturing [92] and in a whole-cell biosensor for ECIS, the cells were grown on Au-film electrodes [93]. Due to the biocompatibility demonstrated in Platinum (Pt) [94], a glucose sensor based on Pt-electroplated carbon electrode was developed to determine glucose in serum [95].

In an Electrical Impedance Tomography (EIT), measurements of the resistance be-

tween different combinations of electrodes are used to determine the resistivity of an object. Different regions the object that is under investigation have different conductivity. Therefore, current flow changes its direction, hence, making it possible to detect the changes in boundary potential. The different tissue has different impedance. Therefore, it is possible to differentiate their reconstructed images and detect physiological changes.

3.2 Historical background of EIT

Tomography is an imaging technique that provides a cross sectional image through an object using measurements performed on the outside of the object. It requires the use of a penetrating wave, such as electromagnetic and ultrasonic which is affected by the materials and structures that make up the oject. It normally involves performing measurements of the absorption, reflection or emission of the measured waves at different angles around the periphery of the object which can be used to reconstruct the distribution of material properties in the cross section.

This technique has applications in the fields of biological [96] and physical sciences [97]. In most cases, the production of these images is based on mathematical tomographic reconstruction, often requiring significant computation. In a typical X-ray tomography at a hospital, a sectional image is made through a body by moving the X-ray source and the film in opposite directions during the exposure. Consequently, structures in the focal plane appear to be sharper, while structures in other planes are hazy. Different focal planes that contain the structures of interest can be selected by adjusting the direction and extent of the movement. Prior to the introduction of

more modern computer-assisted techniques, this technique which was developed in the 1930s by Alessandro Vallebona, a radiologist, proved useful in reducing the problem of superimposition of structures in projection (shadow) radiography [98].

In 1953, B. Pollak described the use of planography, as another term for tomography [99]. A chapter in the American Roentgen Ray Society's 1996 book, "A History of the Radiological Sciences" [100] provides a detailed history of the development of conventional tomography from its inception until being replaced by computer-assisted tomographic techniques starting in the mid to late-1970s. A computed tomographic (CT) scanner was invented by Sir Godfrey Hounsfield who won the Nobel Prize in Physiology of Medicine in 1979 [101]. It was a major advance in diagnostic medicine.

3.3 Biomedical and clinical applications of EIT

In recent years, Electrical Impedance Tomography (EIT) has been used to enable early detection of cancer cells [102]. In particular, EIT has been used for detection of breast cancer cells [103]. EIT is a fast, non-invasive, low-cost tomographic imaging modality that generates cross-sectional or 3D images of conductivity and permittivity distributions within the region of interest which does not involve radiation process. The four main attributes in electrical properties of tissues are resistance (R), conductance (σ), permittivity (ϵ) and capacitance (C).

In a biological tissue, R is an element that opposes the ions flow among its cells while σ is the inverse of R. During the charging process of a capacitor when a supply voltage is present, a charging current, i flows into the capacitor. The charging current is opposed by any changes to the voltage across its conductive plates. The relationship between

the charging current and the rate at which the capacitors supply voltage changes is as shown in equation 3.1, where C is the capacitor capacitance value measured in farads and $\frac{dV}{dt}$ is the rate of change of the supply voltage with respect to time.

$$i = C\frac{dV}{dt} \tag{3.1}$$

Frequency of the applied current affects the ease of current passage which means, higher applied frequency leads to charges flowing through the object back and forth rapidly. In a bioimpedance measurement, the opposition to current flow through a capacitor, C, is known as reactance, X which measurement unit is similar to R that is in Ohms (Ω). If a reactance value is high, the value of its effective resistance to alternating current is also high. The relationship between them is shown in equation 3.2.

$$X = \frac{1}{2\pi fC} \tag{3.2}$$

In an EIT measurement, the tissue conductivity is determined by injecting current through an electrode while measuring the electrode voltage(s). In the case of a breast cancer, the malignant breast tumours demonstrate lower electrical impedance compared to the healthy tissue [103]. A 3D EIT system for breast cancer detection in [104] also mentioned that breast cancer tissue has lower impedance than the normal tissue.

This technique implemented by EIT can produce images by identifying the electrical conductivity distribution of the test sample. High temporal resolution in 2D or 3D images can be produced by the EIT technique [105]. EIT has been implemented in cell cultures and other medical diagnoses [106]. Examples of EIT application in biomedical

and chemical use are to detect breast cancer in a study conducted by Cherepenin [107] and monitor brain function [108].

The EIT group at Oxford-Brookes University developed an EIT system wrapped around the chest; wired then unwired for a 3D EIT imaging of the chest as shown in figure 3.1 and results in figure 3.2 showing low conductivity when there was no breathing activity and simultaneous conductivity change during breathing, were published in [109].

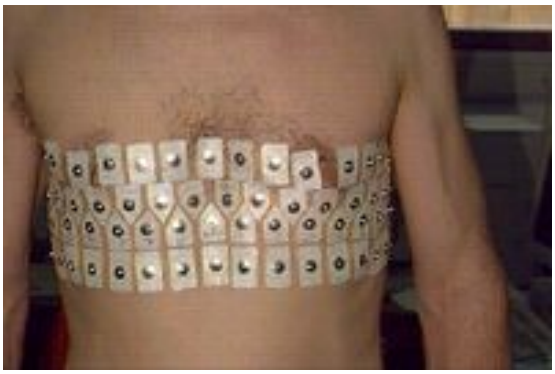

Figure 3.1: EIT imaging of the chest using the OXBACT3 EIT system [5]

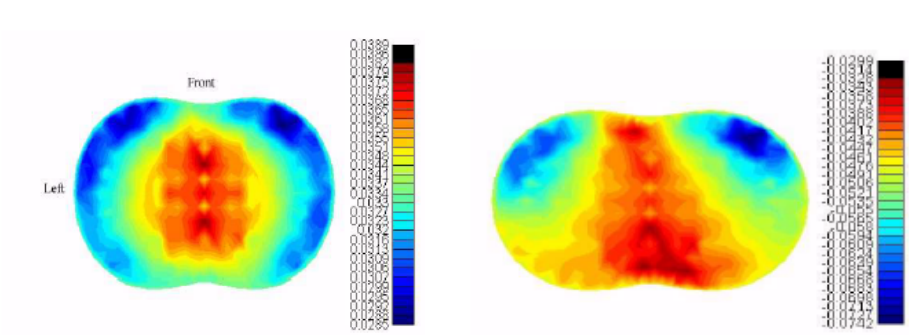

Figure 3.2: Reconstructed images of left: breath holding and right: breathing [109]

In figure 3.3, electrodes were attached to a grapefruit which represents a child's head. Then liquid is injected into the grapefruit to mimic brain haemorrhage. This set-up was exhibited at the London Science Museum to demonstrate the application of EIT in detecting brain haemorrhage.

Figure 3.3: EIT of the brain [6]

3.4 Theory

3.4.1 Electrical Impedance Tomography (EIT)

EIT is a technique that reconstructs the conductivity distribution of an inhomogeneous (non-uniform) medium. An alternating current is forced between a pair of electrodes, and the voltages between adjacent electrode pairs are measured. Conductivity distribution is then estimated based on the calculated boundary voltages [105].

3.4.2 Measurement techniques

In EIT, measurements are made using a ring of electrodes surrounding the sample being tested. In the most typical EIT method, a stimulating alternating current signal

is forced between a pair of adjacent electrodes and the resulting potentials are sensed between each of the other adjacent electrode pairs [106]. A 1.5 mA peak-to-peak current is applied [106] between the first electrode-pair (E1-E2) to ensure a reasonable value of the signal-to-noise ratio (SNR). If the applied current is too small, the response voltage on the electrodes will be very weak. However, if the SNR can be improved, applied current of smaller amplitude can be used in the EIT measurement.

An example of the structure is presented in figure 3.4. An alternating current (I) was first applied between the first electrode pair (E1-E2) and voltage (V) measurements are acquired between neighbouring electrode pairs (E3-E4, E4-E5, ..., E15-E16). The measurement matrix is shown in Table 3.1. The stimulation or excitation electrodes are then changed, and the method is replicated with the current applied between subsequent electrode-pairs (E2-E3, E3-E4, ..., E16-E1) for a total of 208 measurements made for each frame [110].

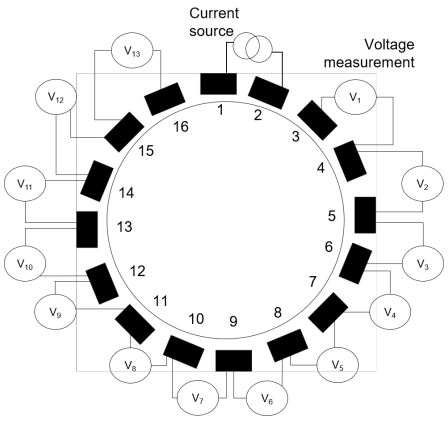

Figure 3.4: Illustration of EIT measurement

Table 3.1: EIT measurement matrix for each pair of electrodes

Current	V1	V2	V3	V4	V5	V6	V7	V8	V9	V10	V11	V12	V13
I1,2	V3,4	V4,5	V5,6	V6,7	V7,8	V8,9	V9,10	V10,11	V11,12	V12,13	V13,14	V14,15	V15,16
I2,3	V4,5	V5,6	V6,7	V7,8	V8,9	V9,10	V10,11	V11,12	V12,13	V13,14	V14,15	V15,16	V16,1
I3,4	V5,6	V6,7	V7,8	V8,9	V9,10	V10,11	V11,12	V12,13	V13,14	V14,15	V15,16	V16,1	V1,2
I4,5	V6,7	V7,8	V8,9	V9,10	V10,11	V11,12	V12,13	V13,14	V14,15	V15,16	V16,1	V1,2	V2,3
I5,6	V7,8	V8,9	V9,10	V10,11	V11,12	V12,13	V13,14	V14,15	V15,16	V16,1	V1,2	V2,3	V3,4
I6,7	V8,9	V9,10	V10,11	V11,12	V12,13	V13,14	V14,15	V15,16	V16,1	V1,2	V2,3	V3,4	V4,5
I7,8	V9,10	V10,11	V11,12	V12,13	V13,14	V14,15	V15,16	V16,1	V1,2	V2,3	V3,4	V4,5	V5,6
I8,9	V10,11	V11,12	V12,13	V13,14	V14,15	V15,16	V16,1	V1,2	V2,3	V3,4	V4,5	V5,6	V6,7
I9,10	V11,12	V12,13	V13,14	V14,15	V15,16	V16,1	V1,2	V2,3	V3,4	V4,5	V5,6	V6,7	V7,8
I10,11	V12,13	V13,14	V14,15	V15,16	V16,1	V1,2	V2,3	V3,4	V4,5	V5,6	V6,7	V7,8	V8,9
I11,12	V13,14	V14,15	V15,16	V16,1	V1,2	V2,3	V3,4	V4,5	V5,6	V6,7	V7,8	V8,9	V9,10
I12,13	V14,15	V15,16	V16,1	V1,2	V2,3	V3,4	V4,5	V5,6	V6,7	V7,8	V8,9	V9,10	V10,11
I13,14	V15,16	V16,1	V1,2	V2,3	V3,4	V4,5	V5,6	V6,7	V7,8	V8,9	V9,10	V10,11	V11,12
I14,15	V16,1	V1,2	V2,3	V3,4	V4,5	V5,6	V6,7	V7,8	V8,9	V9,10	V10,11	V11,12	V12,13
I15,16	V1,2	V2,3	V3,4	V4,5	V5,6	V6,7	V7,8	V8,9	V9,10	V10,11	V11,12,	V12,13	V13,14
I16,1	V2,3	V3,4	V4,5	V5,6	V6,7	V7,8	V8,9	V9,10	V10,11	V11,12	V12,13	V13,14	V14,15

In a single frequency time-difference (TD) imaging, a pair of complementary currents with a fixed frequency were forced between two adjacent electrodes on an EIT device consisting 16 electrodes. Complementary currents means, two sinusoidal currents on two adjacent electrodes were applied with 180° phase difference in every measurement. Firstly, a measurement at time t_0 is recorded as reference data, then the voltage variation at time t_1 with respect to the reference data is used for image reconstruction [105]. The voltage variation is calculated as

$$\Delta V = V_{t_1} - V_{t_0} \tag{3.3}$$

After ΔV is attained, the conductivity distribution is estimated by solving the following optimization problem:

$$\Delta\hat{\sigma} = argmin_{\Delta\sigma}\frac{1}{2}\|\Delta V - \mathbf{J}\Delta\sigma\|_2^2 + \lambda H(\Delta\sigma) \tag{3.4}$$

where $H(\cdot)$ is the regularisation function and λ is the regularisation factor [105].

Brown and Seagar (1987) suggested a method for EIT equipment with 16 electrodes with the *skip-m* method where m is the number of the electrodes that determines the gap between the current carrying electrode and measuring electrode [111]. A current of 5 mA peak-to-peak at 5 kHz is sequentially applied to the human body using a pair of adjacent electrodes, and the method is repeated by applying a current between each pair of adjacent electrodes to obtain a set of electric potential data [111]. Figure 3.5 shows the *skip-0* method in EIT measurements where the blue lines are the current applied and red lines are the voltage measured.

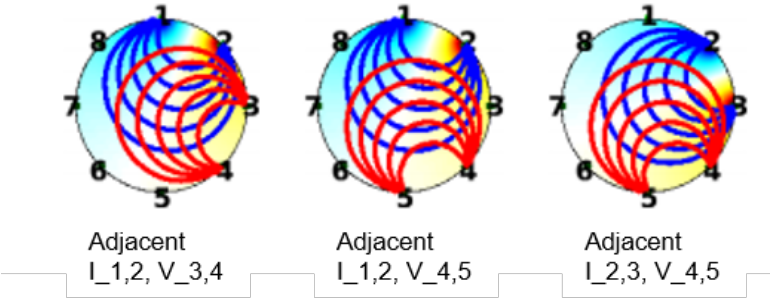

Figure 3.5: Illustration of skip-0 method with 8 electrodes [7]

In contrast to Brown and Sugar, Hua, Webster and Tompkins [112] proposed a different technique called the cross method. Current is applied between a pair of more distant electrodes compared to *skip-0* through two opposed electrodes as illustrated in figure 3.6. Distinguishability is the crucial concept in comparing injection strategies. It is the smallest conductivity change that can produce variations in the measured electric potentials more substantial than the uncertainty level of the measurements in the electrodes.

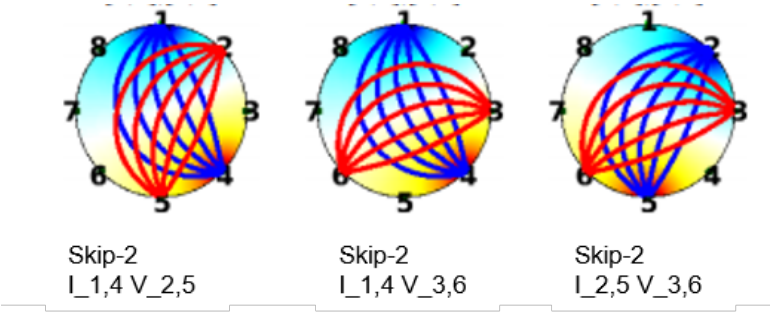

Figure 3.6: Illustration of skip-2 method with 8 electrodes [7]

An electrode is a transducer that converts an electric signal (electronic current) in a wire to an ionic current in an electrolyte, containing cells [89]. Figure 3.7 shows an equivalent circuit of the electrode-electrolyte impedance. It is considered that each cell is expressed in an equivalent circuit, and the biological tissue is constituted. In the case of a uniform living tissue, an equivalent circuit on tissue level is express by

intracellular and extracellular resistances R_i, R_e, cell membrane capacitance C_m, and the bulk resistance of the electrolyte R_B.

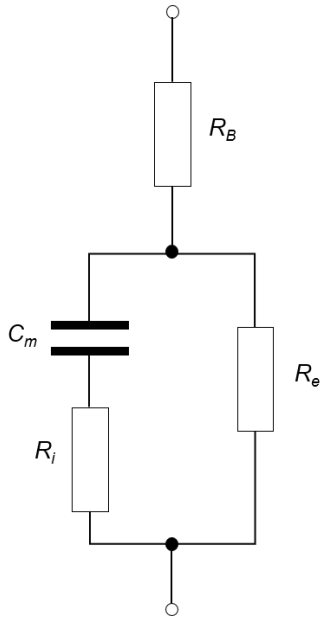

Figure 3.7: Equivalent circuit of the experimental set-up which include the biological system as implied by the components [8]

In relation to the cell electrical properties, The features found in the cell are electrically excitable. When a single cell is inactive, the inner part of the cell will be generally negative. The outer part of a neurone cell will be positive and has electrical properties. When there is a transmission of signal to other cells, the features in the cell will start to excite through cell polarisation. During cell polarisation, the inner cell membrane will be polarised with respect to the outer part of the cell. At this moment, the negatively charged features in the cell will be attracted towards the positively charge features which concentrate along the outer part of the cell. When this happens, the cell is said to be polarised and there appears to be a potential difference between the middle part and the outer part of the cell membrane. It is possible to measure the potential difference between the inner part and outside part of the cell by recording the potential difference. Figure 3.8 illustrates the reactions involved with regards to the cell

polarisation which consists of four reactions; molecules attached to the cell membrane, the return of a membrane cell to the cytoplasmic pool, cells transmitting signals to other cells, and the cell migration. Contact impedance between the electrode and the tissue has to be small and known, in order to design instruments and reconstruct impedance images. An equivalent circuit is used as a model on the cellular level shown in figure 3.7.

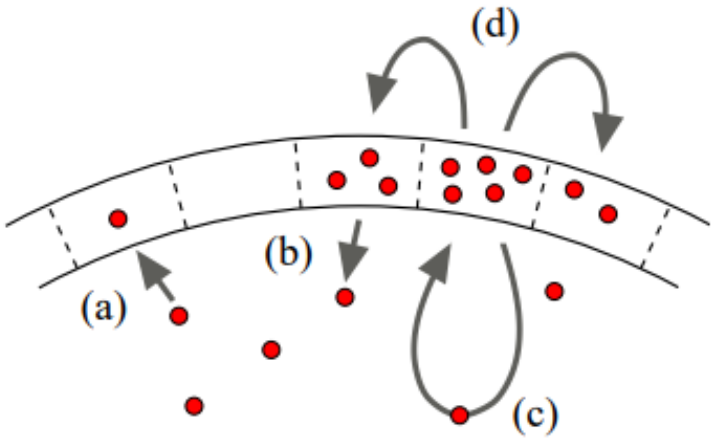

Figure 3.8: Illustration of the reactions with regards to cell polarisation where (a) signalling molecules attach to the cell membrane, (b) a membrane molecule returns to the cytoplasmic pool, (c) transmission of signals to other cells, and (d) cell migration [9]

Materials and electrode size are the two essential factors to be considered in electrode design. Electrodes made of the right materials and size are crucial to interface between the instrument metal and the ionic conductors in the tissue. Silver (Ag) electrodes coated with AgCl are the most commonly used for measuring the electrocardiogram (ECG). Stainless steel is a conventional electrode material since it does not corrode. Au and Pt are used in specialised applications due to their biocompatibility [113]. Graphite is often added to plastic materials to make them conductive due to its low cost [114]. Carbon electrodes will not introduce toxic products when embedded in the body, which is not the case for some other metals [115].

In addition to metals, electrodes can also be made from conducting polymers [116]. A natural polymer such as karaya gum needs NaCl and other chemicals to be added to produce a conductive adhesive polymer. Their impedance value is suitable for ECG electrodes, but the impedance is high when used in imaging. Polyvinylpyrrolidone is an example of a synthetic polymer that is hydrophilic, elastomeric, water-insoluble pressure-sensitive adhesive. It has been used as an ECG electrode despite its high impedance value [89].

3.4.3 Image reconstruction techniques

In most cases, the production of reconstructed images is based on mathematical tomographic reconstruction. In a 3D image reconstruction, algorithms with multi-plane electrode arrangements have been applied to create more accurate reconstructed impedance distributions [117] [118] [119]. It is recommended to implement planar electrode placement such that 16 electrodes are placed in two rings of vertically aligned electrodes with electrodes placed sequentially in each ring [120].

Fundamentally, EIT involves the solving of two problems: the forward problem and the inverse problem. The forward problem determines the electrical voltage distribution on the outermost surface of the object arising from the applied current pattern injection and conductivity distribution [121]. On the other hand, the inverse problem is the image reconstructing step for EIT. The purpose of the reconstruction algorithm is to define conductivity distribution obtained from the electrical voltage measurement and sensitivity matrix [122].

Among five of the popular image reconstruction algorithms are Linear Back-

Projection, linear Landweber, linear conjugate gradients, linear regularised Gauss-Newton and non-linear regularised Gauss-Newton. Linear Back-Projection (LBP) is a simple and fast algorithm of image reconstruction besides being one of the most common techniques used in electrical tomography [123]. It is regularly implemented for its fast speed. However, it results in a low quality of the reconstructed image. Therefore to attain a high-quality image reconstruction, an iterative image reconstruction algorithm is applied, and the Landweber algorithm is one example [124]. It is based on the linearisation of a normalised form of the problem. More specifically, the normalised forward problem is approximated using a series of hyper-planes. The reconstruction matrix used in LBP is found to be a 'weighted' transpose of the linear operator (matrix) that defines the linearised-normalised forward problem. The rows of this latter matrix contain the information of the sensitivity maps used in LBP.

Theoretically, EIT defines the relationship between conductivity change, $\delta\sigma$, and the potential difference, $\delta\mathbf{V}$, within a detecting domain. This relationship can be written as:

$$\delta\mathbf{V} = \mathbf{J}\delta\sigma \tag{3.5}$$

where $\mathbf{J}$ is the Jacobian (sensitivity) matrix of EIT.

The image reconstruction for EIT encompasses the calculation of conductivity distribution when the current introduced is known and voltage readings are recorded. Due to the intrinsic ill-posedness and ill-conditioned characteristic of the EIT image reconstruction problem, the solution can be formulated as the following optimization problem based on regularisation techniques:

$$\delta\sigma_\lambda = argmin_\sigma \|\mathbf{J}\delta\sigma - \delta\mathbf{V}\|^2 + \lambda f(\delta\sigma) \tag{3.6}$$

where λ represents the positive scalar regularisation parameter and f is the regularisation function encoding prior constraint information.

3.4.3.1 Tikhonov Regularisation

Tikhonov regularisation is one of the most popular regularisation methods for solving ill-posed inverse problems and has been applied to EIT image reconstruction. The Tikhonov regularisation can be formulated as:

$$\delta\sigma_\lambda = argmin_\sigma \|\mathbf{J}\delta\sigma - \delta\mathbf{V}\|^2 + \lambda\|\delta\sigma\|^2 \tag{3.7}$$

Further, the solution above can be written as:

$$\delta\sigma_\lambda = (\mathbf{J}^T\mathbf{J} + \lambda\mathbf{I}^T\mathbf{I})^{-1}\mathbf{J}^T\delta\mathbf{V} \tag{3.8}$$

where $\mathbf{I}$ denotes the unity matrix.

3.4.3.2 Gaussian-Laplace Regularisation

Another commonly applied regularisation tool is the Gaussian-Laplacian method. Figure 3.9 shows the three popular Laplacian operators applied to a single pixel.

0	1	0
1	-4	1
0	1	0

1	1	1
1	-8	1
1	1	1

-1	2	-1
2	-4	2
-1	2	-1

Figure 3.9: Convolution kernels to approximate Gaussian-Laplace second-order derivates

In this work, the first operator, i.e., the second-order four connected region Laplace operator, is adopted. Accordingly, equation 3.6 can be rewritten as:

$$\delta\sigma_\lambda = argmin_\sigma \|\mathbf{J}\delta\sigma - \delta\mathbf{V}\|^2 + \lambda\|\mathbf{L}\delta\sigma\|^2 \tag{3.9}$$

Further, the solution above can be written as:

$$\delta\sigma_\lambda = (\mathbf{J}^{\boldsymbol{T}}\mathbf{J} + \lambda\mathbf{L}^{\boldsymbol{T}}\mathbf{L})^{-1}\mathbf{J}^{\boldsymbol{T}}\delta\mathbf{V} \tag{3.10}$$

where $\mathbf{L}$ is the second-order four connected region Laplace operator matrix.

3.4.3.3 L_1 Regularisation

Over-fitting is a problem that occurs when a model contains a large set of data. Regularisation is one of the techniques to avoid over-fitting, where it 'pushes' the coefficients in. For example, vector, $\boldsymbol{x}$, to set to be zero for many components and then, reduces the vector size. L_1 regularisation is applied to the model to reduce its size. Hence, by implementing L_1 regularisation, vector $\boldsymbol{x}$ becomes smaller (more sparse), as most of the components are zeros.

Letting λ as the regularisation parameter, then equation 3.6 in section 3.4.2 can be rewritten as:

$$\delta\sigma_\lambda = argmin_\sigma \|\mathbf{J}\delta\sigma - \delta\mathbf{V}\|^2 + \lambda\|\delta\sigma\|_1 \tag{3.11}$$

Equation 3.11 is solved iteratively based on the spectral projected gradient for L_1 minimisation method [125].

3.5 Summary

Live-cell imaging is an essential analytical tool in biomedical research and pharmaceutical laboratories. Live-cell microscopy involves a compromise between obtaining an excellent image quality and ensuring the cells are in good condition. Hence, the spatial and temporal resolutions in an experiment are often limited to avoid exposing the cells to a high illumination intensity over an extended period. Electrical Impedance Tomography is a promising technique for non-invasive, radiation-free monitoring technology. It is widely relevant and safe for the patient, enabling continuous real-time monitoring of electrical properties of the organ or tissue over extended periods of time. Even though the principle of EIT has been known for over thirty years, there are ongoing research projects and publications signifying its possible applications in clinical practice in recent literature.

Since micro-bioimpedance tomography research has not been widely studied, in order to close the gap in research, micro-scale electrodes were designed in this research and prior to the fabrication, an FEM was performed and further described in Chapter 4. From the results obtained in Chapter 4, the following steps were designing and fabricating the micro-scale electrodes for micro-bioimpedance tomography. Detailed explanation with regards to the methods are discussed in Chapter 5. Micro-bioimpedance tomography were then being performed on MCF7 spheroids and microbial cultures using the fabricated micro-scale electrodes. Results and analysis of the micro-bioimpedance measurements are explained in Chapter 6.

Chapter 4

Finite Element Modelling (FEM) of micro-scale electrodes

4.1 Introduction

The description of the laws of physics for space and time-dependent problems are typically expressed in terms of Partial Differential Equations (PDEs) and, in most cases, these PDEs cannot be solved using analytical methods. Therefore, an approximation of the equations will usually be constructed based on numerous types of discretisations [126]. The FEM is the dominant discretisation technique in structural mechanics [127] and is a method for numerical solution of field problems that divides a structure into multiple elements [128].

FEM is one of the vital computation tools in various engineering fields. In neural engineering, the technique is beneficial to interpret recorded electrical bio-signals

generated by neural or muscle tissue activities [129]. In the electronics industry, FEM has become known in the analysis of products subjected to impact loading due to producing robust products by manufacturers [130].

4.2 Motivation of Modelling and Simulation

Modelling is a way to represent an actual system, and that includes both software and hardware. If mathematical relationships drive the software components of a model, the virtual representation can be computed under an extensive range of conditions to see its behaviour [131].

The motivation for using FEM is to determine the influence of model parameter on the solution by performing a sensitivity analysis [132]. The sensitivity analysis is crucial in increasing model robustness, design optimisation, identifying parameters that require further research, eliminating variables to simplify a model and providing a better understanding of a model as well as variable interactions [133].

The FEM evaluates the optimum electrode layout and determines what is the most effective micro-scale electrode morphology that can be made without affecting its performance and the measurement efficacy. The types of FEM involved in this research were 2D and 3D modelling. The 2D modelling identified which electrode tip morphology gave the optimum performance and compared the simulation results with experimental results. The 3D modelling was performed to study the sensor's performance on cell cultures since the 'domain' in a 2D simulation is the surface and not the volume. Hence, simulations using cell spheroids had to be performed with the 3D model.

4.3 Simulation models

The simulation models were created and analysed using COMSOL Multiphysics® and the purpose of FEM is defined in figure 4.1 to obtain sensitivity distribution.

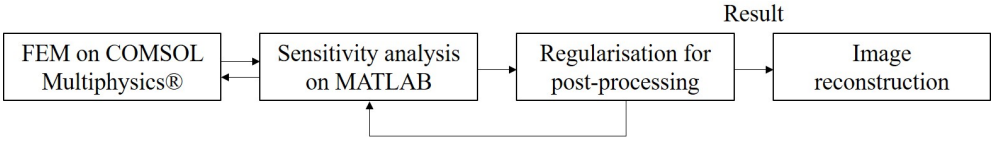

Figure 4.1: Process of the simulation models

4.3.1 Micro-scale electrode morphologies

Measuring voltage on an electrode separate from the current electrode minimises the effect of contact impedance [89]. Four different micro-scale electrode morphologies were proposed and presented in figures 4.2, 4.3, 4.4 and 4.5 to investigate which electrode shape gives the finest imaging resulting in high-resolution images.

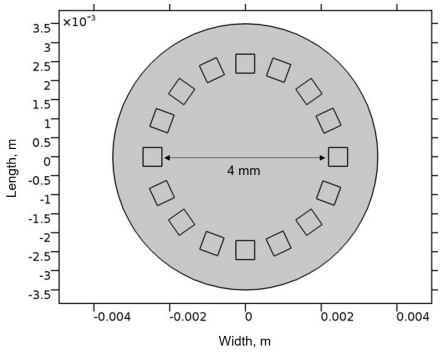

Figure 4.2: Square electrodes, length = 500 µm

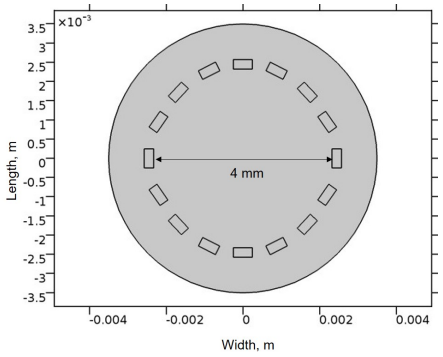

Figure 4.3: Rectangular electrodes, length = 500 µm and width = 250 µm

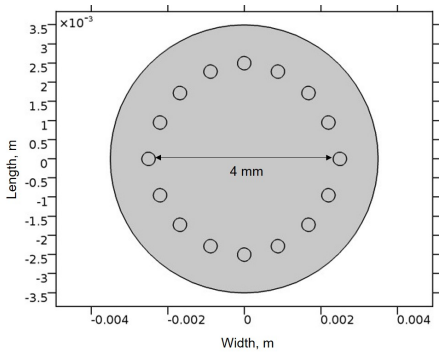

Figure 4.4: Circular electrodes, radius = 175 µm

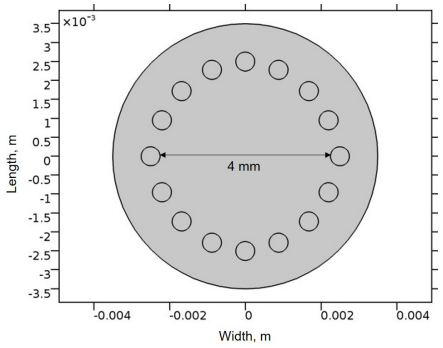

Figure 4.5: Circular electrodes, radius = 250 µm

4.3.2 Simulation setup

The impedance of an artefact is dependent on the electromagnetic properties of the material composing it. Material properties related to impedance are:

(a) Conductivity

(b) Resistivity

(c) Permittivity

(d) Permeability

The COMSOL Multiphysics® modelling involved used the AC/DC application module with Electric Currents (ec) physics. Table 4.1 shows the material properties of Phosphate-Buffered Saline (PBS) and Pt electrodes defined in the model.

Table 4.1: Material properties defined in COMSOL Multiphysics®

Materials	**Conductivity** σ (S m^{-1})	**Resistivity** ρ (Ω m)	**Relative permittivity** ε_r	**Relative permeability** μ_r
Phosphate-Buffered Saline (PBS)	1.78	0.5618	80	N/A
Pt	8.9×10^6	1.12×10^{-7}	1	1.000265

The boundary/domain settings were set as follows in COMSOL Multiphysics® as shown in figure 4.6.

(1) Electric insulation (Fluid reservoir)

(2) Terminal (Electrodes)

(3) Ground (Point at 0,0)

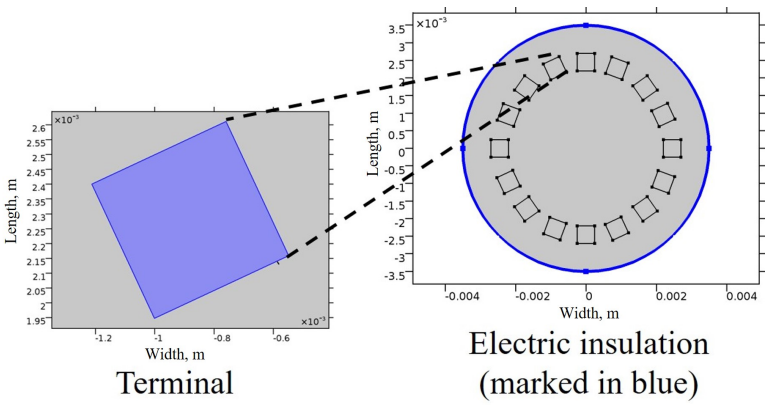

Figure 4.6: Graphical representation of the boundary/domain settings in COMSOL Multiphysics®

An alternating current of 1.5 mA was forced between a pair of adjacent electrodes (skip-0) at 10 kHz as described in 3.4.2. The electric potentials were measured between adjacent non-current carrying electrodes. The method was repeated by applying a current between each pair of adjacent electrodes. The MATLAB® scripting was integrated with COMSOL Multiphysics® to swap between electrodes and sequentially apply 1.5 mA AC.

In order to utilise LiveLink™ for MATLAB®, MATLAB® script (.m file) is generated from COMSOL Multiphysics® *Save As* option. However, the simulation file from COMSOL Multiphysics® needs to be solved for a pair of the electrodes prior to saving it as a model file for MATLAB®. In the source code example shown below, eNum denotes the number of electrodes that is 16, indexMap is the array of electrodes according to the domain set in COMSOL Multiphysics®.

```
#Creating the electrode index
eNum=16;
indexMap=[10 12 14 16 17 15 13 11 9 7 5 3 2 4 6 8 10]
#10 is E1 and electrode position is going upwards
```

```
[newnode,nodenum]=nodeeit(64);

for i=1:eNum
#Selecting the excited electrodes
#current excitation 1
model.physics('ec').feature('term1').selection.set([]);
#current excitation 2
model.physics('ec').feature('term2').selection.set([]);

#current excitation 1
model.physics('ec').feature('term1').selection.set([indexMap(i)]);
#current excitation 2
model.physics('ec').feature('term2').selection.set([indexMap(i+1)]);
```

In the *for* loop, each pair of adjacent electrodes (those carrying current) is sequentially swapped.

Since current forcing electrodes are different from the electrodes measuring voltage, sensitivity is the dot product of the electric fields of voltage electrodes and the current electrodes. In COMSOL Multiphysics® modelling, each measurement point contains data of $[E_x(x,y), E_y(x,y)]$ where (x,y) is the Cartesian coordinate of a measurement point, E_x is the electric field in x-direction and E_y is the electric field in y-direction as shown in figure 4.7.

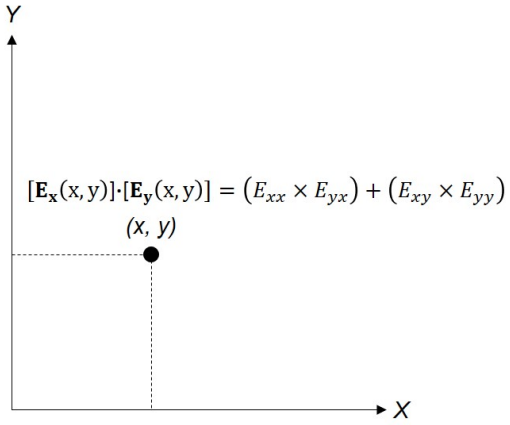

Figure 4.7: Electric field in COMSOL Multiphysics® modelling

A 64 × 64 array pixels image was chosen in the research to display the reconstructed images. Figure 4.8 illustrates a 64 × 64 array pixels made up 4096 pixels. From 4096 pixels, 3320 pixels represented the cross-section of the fluid reservoir, that is the experimental boundary, while another 776 pixels are outside the boundary.

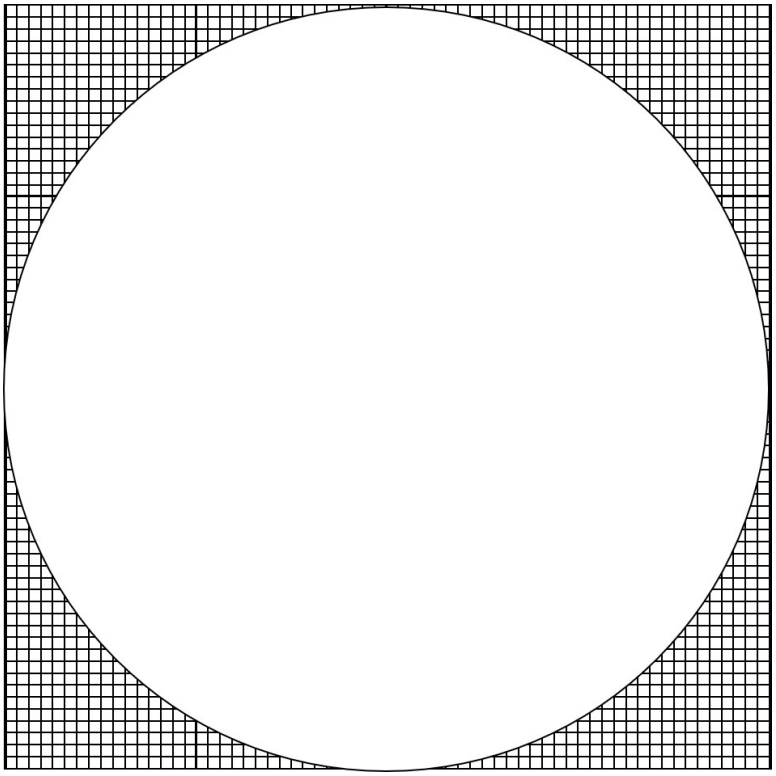

Figure 4.8: 64 × 64 array pixels was chosen in the research for image reconstruction of micro-bioimpedance tomography

In the following source code, each function has different roles in a simulation model.

```
#Ex is electric field, x component
efieldx=mpheval(model, 'ec.Ex');
#Ey is electric field, y component
efieldy=mpheval(model, 'ec.Ey');

#Returns the coordinates of the evaluation points
data1=efieldx.p;
data2=efieldy.p;

#Returns the indices of the mesh elements at each evaluation point
nodenum=efieldx.ve;

#Gets electric field in x-direction
elex(i,1:length:(nodenum))=mphinterp(model, 'ec.Ex', 'coord', data1);

#Gets electric field in y-direction
eley(i,1:length:(nodenum))=mphinterp(model, 'ec.Ey', 'coord', data2);

CirS(k,:)=(-(dot(elex(i,:)',eley(i,:)')+dot(elex(j,:)',eley(j,:)')));
```

They are as described below:

```
mpheval #To evaluate the expression at all node points

mphinterp #To evaluate expressions at extracted data in co-ordinates
in data1 and data2

ec.Ex and ec.Ey #The electric fields in x- and y-components respectively

CirS$()$ #A function that evaluates the sensitivity
```

The function Cirs() that evaluates the sensitivity solves the **dot** product of the two fields, elex and eley which expresses the sensitivity to conductivity changes.

The electric fields simulated for all four types of micro-scale electrode are exemplified in figure 4.9. The electrodes size in the FEM has the same size as the micro-scale electrodes on glass substrate. The intensity of electric field between electrode 1 (E1) and electrode 2 (E2) gives information with regards to the strength of the electric field at the particular location. The electric field is greatest as the distance between electrodes gets closer.

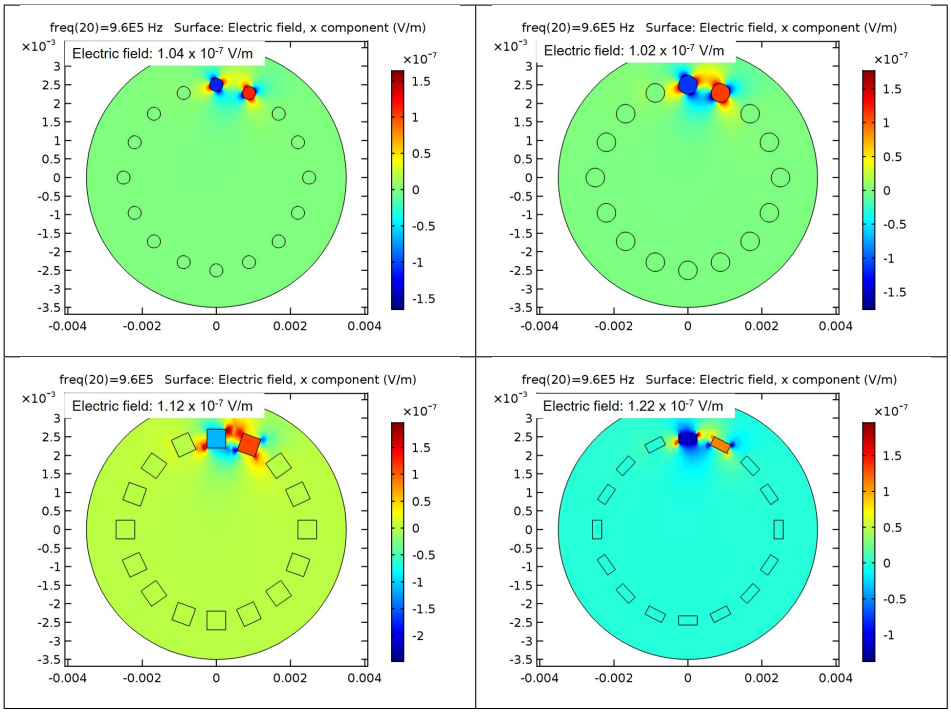

Figure 4.9: Electric fields for the micro-scale electrodes. Top left: circular electrodes, radius = 175 µm, top right: circular electrode, radius = 250 µm, bottom left: square electrodes, length = 500 µm, and bottom right: rectangular electrodes, length = 500 µm, width = 250 µm

With the circular electrodes, each charge has no net force on then, because they are in equilibrium since there is the same amount of charge on either side of the electrodes. However, for square and rectangular electrodes, the charge is piling up at the edge of the electrodes because in such way, it balances the forces on each charge. The electric field is strongest on the edge of the electrodes because it is higher when the distance between the edges is shorter.

The shape of the electric field is defined by the shape of the electrodes and the distribution of the electric field is affected by the geometry of the electrodes. Equally-spaced micro-scale electrodes produce a uniform distribution of charges. The 175 µm radius circular electrodes do not illustrate a strong electric field between E1-E2, unlike the 250 µm radius circular electrode, 500 µm square electrodes and rectangular electrodes. The charge accumulates at the edge of both square and rectangular electrodes, resulting the strongest field at these areas. The best ones are the 500 µm square electrodes and rectangular electrodes because they have the highest electric field.

Figure 4.10 illustrates the sensitivity evaluated by the source code previously described in 4.3.2. The sensitivity distribution is normalised which means it is dimensionless (without units). It reflects the relative change. Based on the sensitivity distribution, the square and rectangular electrodes were giving the highest sensitivity, therefore, the optimum electrode shape was either square with length = 500 µm or rectangle with the dimension length = 500 µm and width = 250 µm.

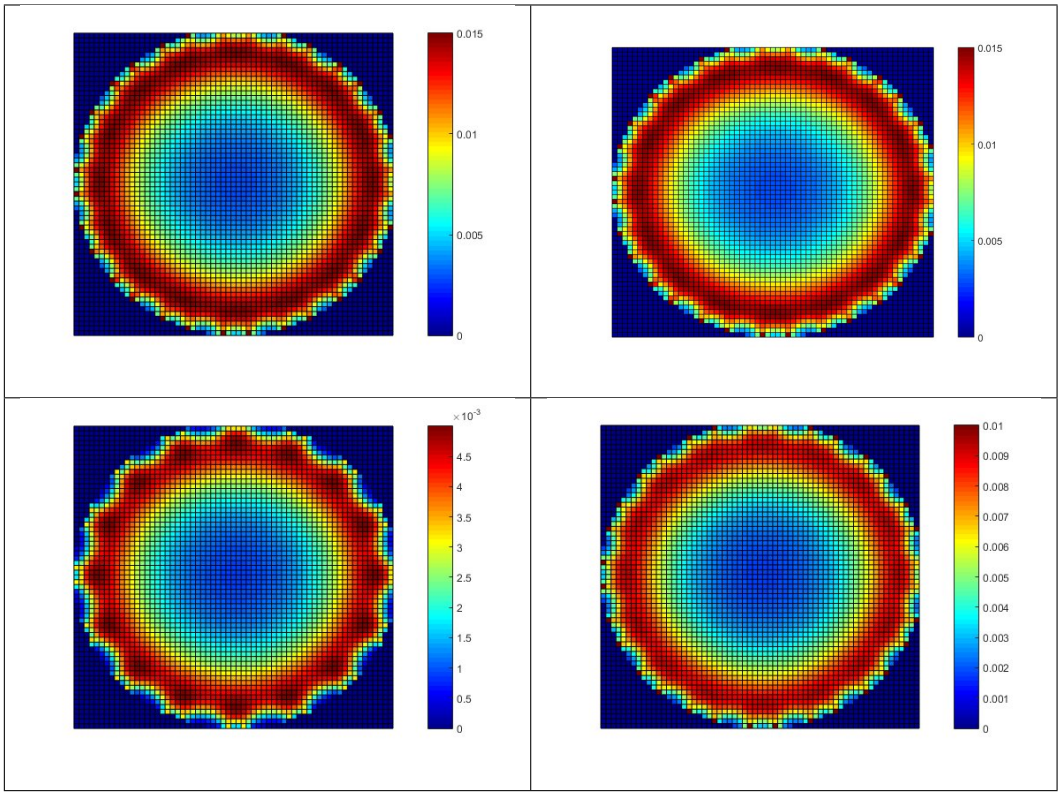

Figure 4.10: Sensitivity distribution and simulated voltage measurements for square electrodes, length = 500 µm, rectangular electrodes, length = 500 µm and width = 250 µm, circular electrodes, radius = 175 µm, and circular electrodes, radius = 250 µm

With regards to 3D EIT, a simulation study was performed to improve the electrodes that are placed around a body surface and current patterns for 3D EIT [10]. This study was done on macro-scale electrodes in a 30 cm × 28 cm diameter. The purpose of the study was to investigate different electrode morphology with various measurement patterns. The configuration of two-layer planar electrodes produced promising results which could lead to an improved image reconstruction in EIT.

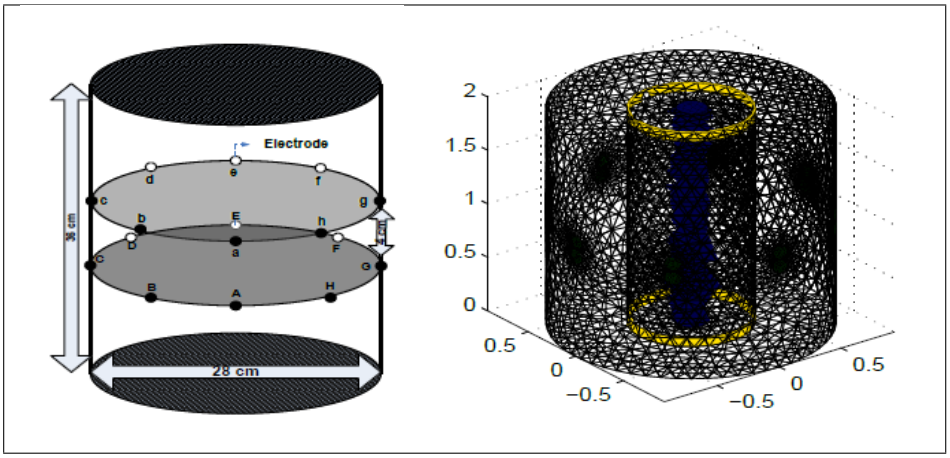

Figure 4.11: Left: Configuration of two-layer 16 planar electrodes in a 30 cm height and 28 cm of diameter cylinder, right: simulation result of a two cylindrical test samples spanning the full height of the cylindrical volume [10]

4.4 Summary

It can be observed that square electrodes (500 µm × 500 µm) and rectangular electrodes (500 µm × 250 µm) show the highest normalised sensitivity on the electrodes. The sensitivity is affected by the electric field that is a measure of electric force per unit charge, (Vm^{-1}). These electrodes experimentally exhibit similar result. In addition to that, EIT measurement is affected by the placement of the fluidic chamber and possible differences between electrodes. Depending on the fluidic chamber position, small changes in media volume and interfacial electrode impedance will cause variation in voltage measurements.

Chapter 5

Electrode design and fabrication for micro-bioimpedance tomography

5.1 Introduction

This chapter presents the development of the micro-bioimpedance sensor design and fabrication. Factors that are investigated include biocompatibility, electrode material, electrode morphology, and resistance. This resulted in the development of nickel-gold (NiAu) electrodes on Printed Circuit Board (PCB), platinum (Pt) electrodes on a glass substrate and a gold (Au) micro-scale electrode array on a flexible PCB (Flex-MEA).

5.2 Electrodes design on a PCB

An initial electrodes design was implemented on a PCB with 16 electrodes in a ring. The full PCB consists of four sets of electrodes with different designs for the electrode

geometries. The electrodes were fabricated on a PCB with Copper (Cu) tracks with the following designs:

- Circular electrodes, radius = 0.5 mm
- Circular electrodes, radius = 0.25 mm
- Rectangular electrodes, 1.0 mm × 0.5 mm
- Square electrodes, 1.0 mm × 1.0 mm

5.2.1 Electrode design on EAGLE version 7.6.0 and rapid prototyping to produce Cu electrodes

The low-cost, rapid prototyping facilities available at the Scottish Microelectronics Centre (SMC) were utilised to fabricate the electrodes on a PCB. Figure 5.1 shows the PCB design for EIT measurement using EAGLE, an electronic computer-aided design (ECAD) software with the fabricated PCB presented in figure 5.2. A fluid reservoir shown in figure 5.3 was attached to the PCB using UV cured epoxy at which point the system was ready for measurements.

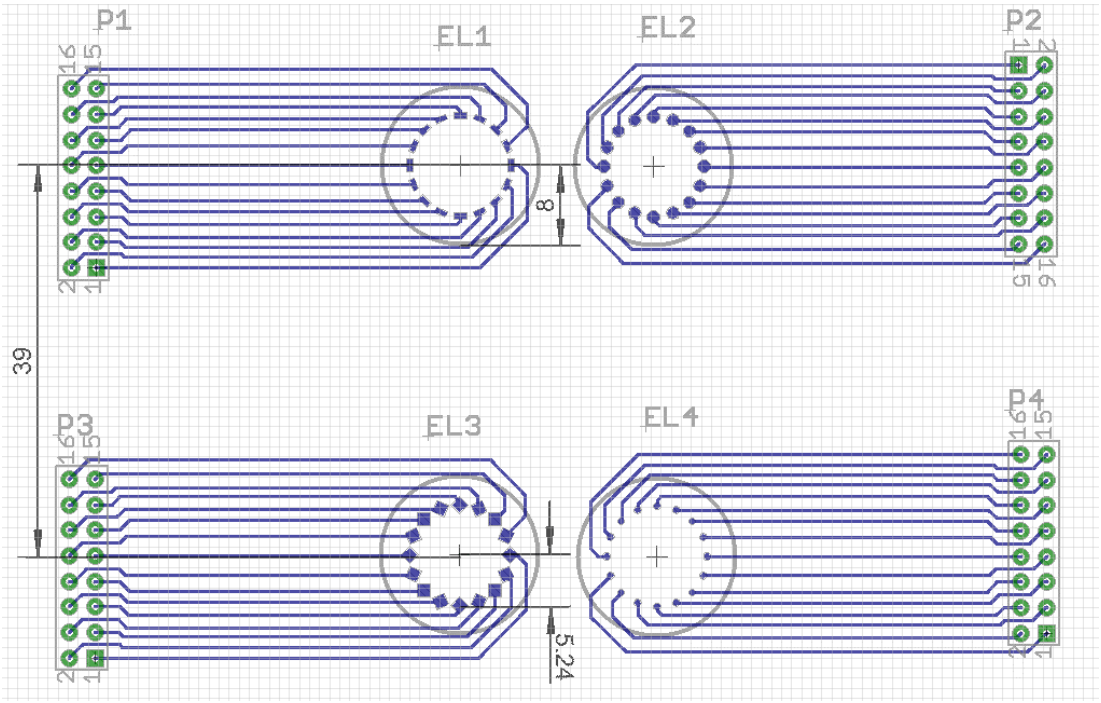

Figure 5.1: PCB design on EAGLE version 7.6.0 for EIT measurements

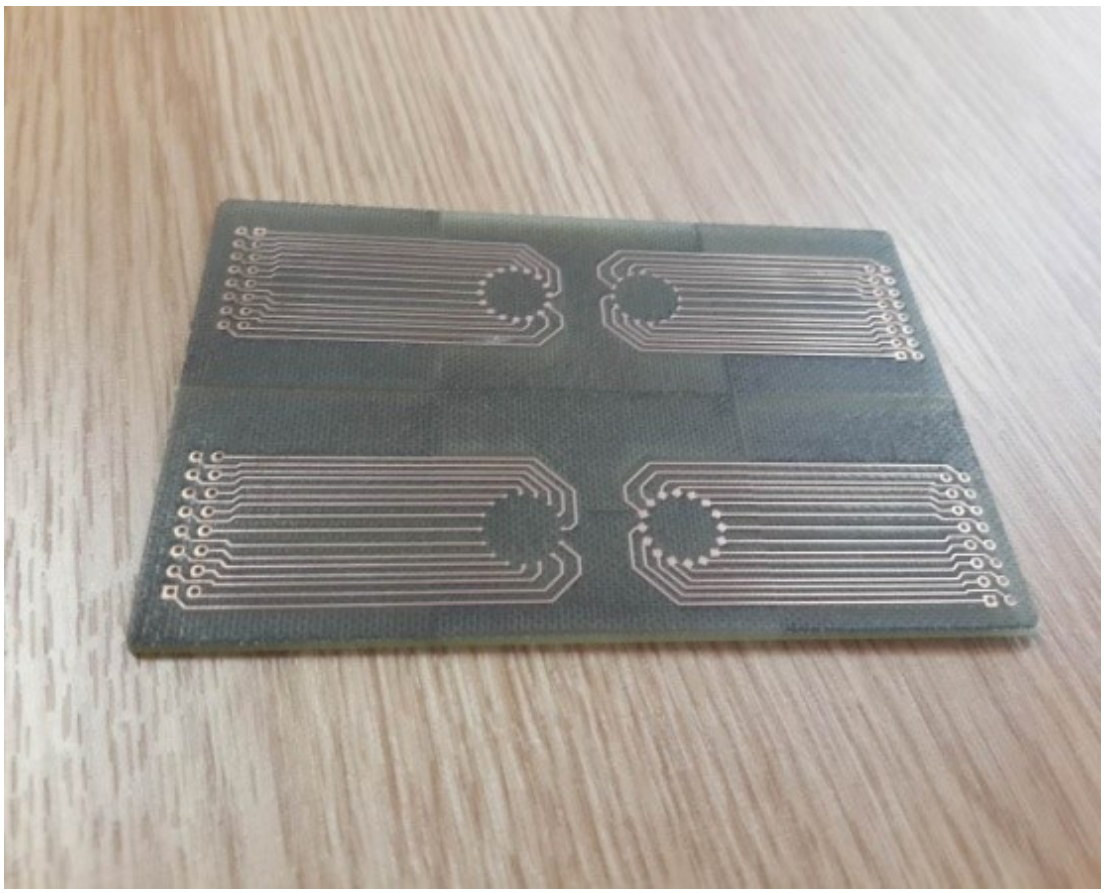

Figure 5.2: PCB fabricated using the rapid prototyping for EIT measurements

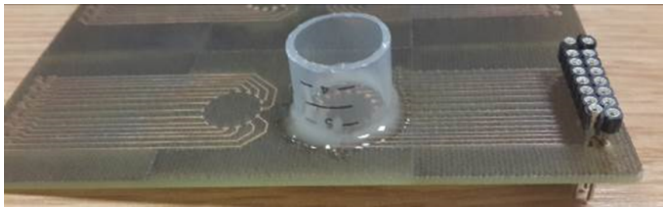

Figure 5.3: Side view of the fluid resevoir

5.2.2 Nickel (Ni) and Au electroplating for biocompatible electrodes

5.2.2.1 Introduction to general electrochemistry

Electrochemistry is the branch of chemistry that studies the relationship of electrical and chemical effects [134]. Electrochemistry is the study of chemical reactions that involve electron or charge transfer, reduction and oxidation. In an electrochemical experiment where a working electrode and a reference electrode are immersed in a solution, the potential difference between the reference and working electrodes is varied using an external power supply as shown in figure 5.4. The electrochemical reaction occurs at the working electrode while the reference electrode has a consistent and known electrode potential.

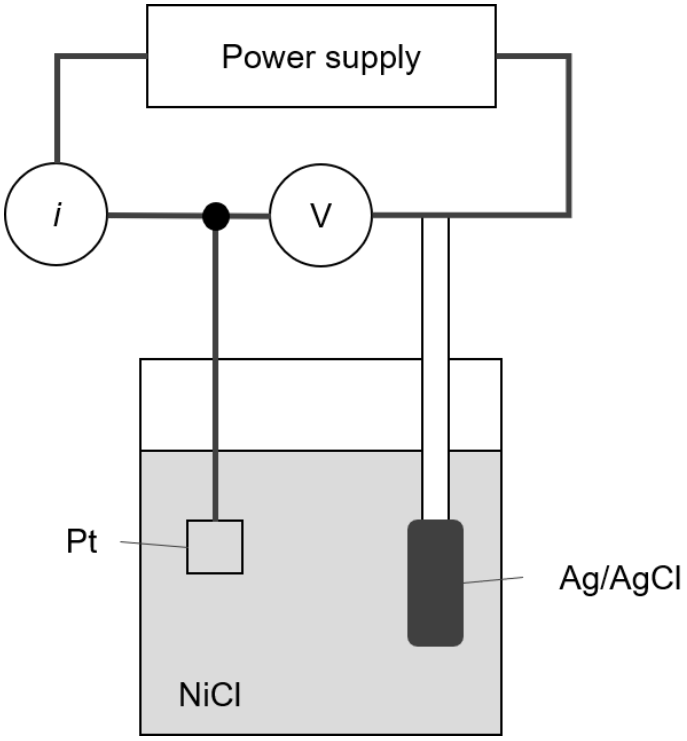

Figure 5.4: Schematic diagram of the electrochemical cell Pt/NiCl/Ag/AgCl attached to power supply and meters (or a potentiostat) for obtaining a cyclic voltammetry (CV) curve

All potentials are measured with respect to a separate reference electrode in the solution. The potential difference, V, can produce a current flow in the external circuit because electrons cross the electrode/solution interfaces as electrochemical reactions occur. The number of electrons is measured with regard to the total charge, Q, passed in the circuit. Charge is expressed in the units of coulombs (C), where 1 C $= 6.24 \times 10^{18}$ electrons. The relationship between charge and amount of product formed is given by the *Faraday's law*; that is, the passage of 96,485.4 C causes a reaction (e.g., consumption of 1 mole of reactant or production of 1 mole of product in a one-electron reaction). The current, i, is the rate of flow of charge (or electrons), where a current of 1 Ampere (A) is defined as 1 C s^{-1}. When the current is plotted as a function of the potential, a current-potential *(i vs V)* curves results. Such curves are informative about the nature of the solution and the electrodes and about the reactions that occur at the interfaces.

5.2.3 Aims of plating the electrode tips

Since Cu is easily corroded and is toxic to cells, Au of thickness 0.5 µm was electrochemically plated on the Cu electrodes to make them biocompatible. As Au does not tarnish and is found to be nontoxic to cells [135]. The 3-electrode configuration shown in figure 5.5 was used for the electroplating process, using a Pt mesh counter electrode and an Ag||AgCl||KCl (3 M) reference electrode. Prior to Au plating, the electrodes were coated with a thin layer of 0.2 µm of Ni as a barrier layer to avoid Au migration to Cu. The amount of time required for the electroplating of Ni and Au varies according to the shapes and dimensions depending on the area of electroplating to occur.

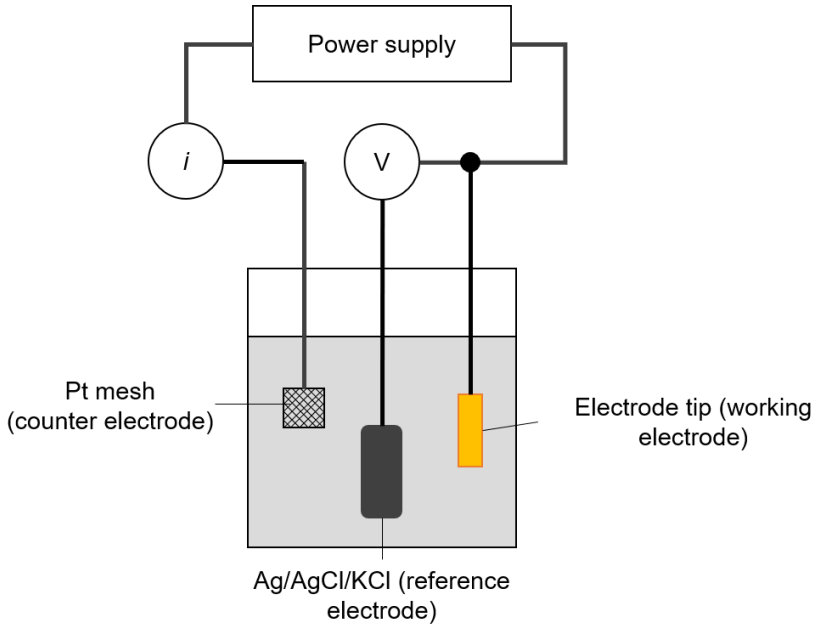

Figure 5.5: Schematic diagram of the 3-electrode configuration used in the electroplating process

Electroplating times and current density were studied to obtain a uniform electroplating process. The time required for an electroplating process can be determined by:

$$t = \frac{d\rho nFA}{jA_w} \tag{5.1}$$

where:

d = thickness of the plated metal (Ni or Au) (cm)

ρ = metal density of Ni or Au (gm cm^{-3})

n = number of electrons to be transferred (from Ni^{2+} to Ni, n=2, and from Au^{+} to Au, n=1)

F = Faraday constant; 96485 C mol^{-1}

A = area of Ni or Au electroplating to occur (cm^2)

j = current density of 20 mA cm^{-2} for Ni plating [136] 10 mA cm^{-2} for Au plating [137]

A_w = atomic weight of Ni, 58.6934(4) [138] or Au, 196.9665(5) [138]

5.2.4 Electroplating

5.2.4.1 Ni plating

The Ni-plating acts as a barrier layer to ensure no Au migration to Cu. The electroplating process was performed with the chemical composition of Ni-plating solution defined in table 5.1.

Chemical	**Molarity (M)**
110 gl^{-1} Ni(II) chloride hexahydrate ($NiCl_2.6H_20$)	$0.\bar{4}6$
30 gl^{-1} Boric acid (H_3BO_3)	0.1
2 gl^{-1} Sodium saccharin	–
0.1 gl^{-1} Sodium dodecyl sulfate (SDS)	–
250 µl of 5% HCl to stabilise the pH of the electrolyte between 2.9 and 3.0	–

Table 5.1: Chemical composition of the Ni-plating solution

The target pH of the Ni-plating solution was pH 3.0 and the electrolyte maintained at a value between 2.9 and 3.0. The pH was kept constant by adding 250 µl of 5%

hydrochloric acid (HCl) solution to the Ni plating solution with the concentration of 110 gl^{-1}, 0.46 M. The Cu electrodes were being cleaned with 10% sulfuric acid (H_2SO_4) prior to the electroplating process and Ni was deposited at a current density of 20 mA cm^{-2}. The required electroplating time was calculated using equation 5.1 with the atomic weight of Ni, 58.6934(4) [138] and a current density of Ni, 20 mA cm^{-2} [136] to have a uniform layer of Ni on the electrodes. The process was then repeated for the rest of the electrodes.

At the working electrode, reduction occurred and resulted in deposition of atomic Ni, Ni^0.

$$Ni^{2+} + 2\,e^- \longrightarrow Ni^0 \tag{5.2}$$

Figure 5.6 shows photos of the Ni-plated electrodes and figure 5.7 shows the chronopotentiometry plots (an electrochemical technique where the current of the working electrode is kept constant, and the resulting potential from Faradaic processes occurring at the electrode is monitored as a function of time). After completing the Ni electroplating process, the Ni-plated surface was cleaned with 10% H_2SO_4 as it is a standard protocol of cleaning metal excess for 15 minutes before proceeding to the Au electroplating process.

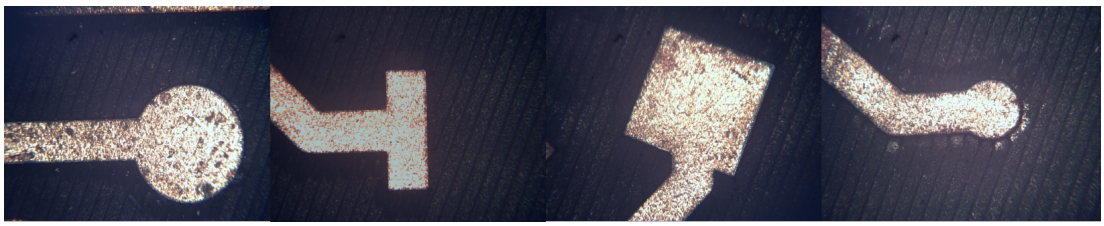

Figure 5.6: Microscopic images of Ni-plated EIT electrode designs, from left to right the dimensions are as follows: radius = 0.5 mm (circular electrodes), 1.0 mm × 0.5 mm (rectangular electrodes), 1.0 mm × 1.0 mm (square electrodes), radius = 0.25 mm (circular electrodes)

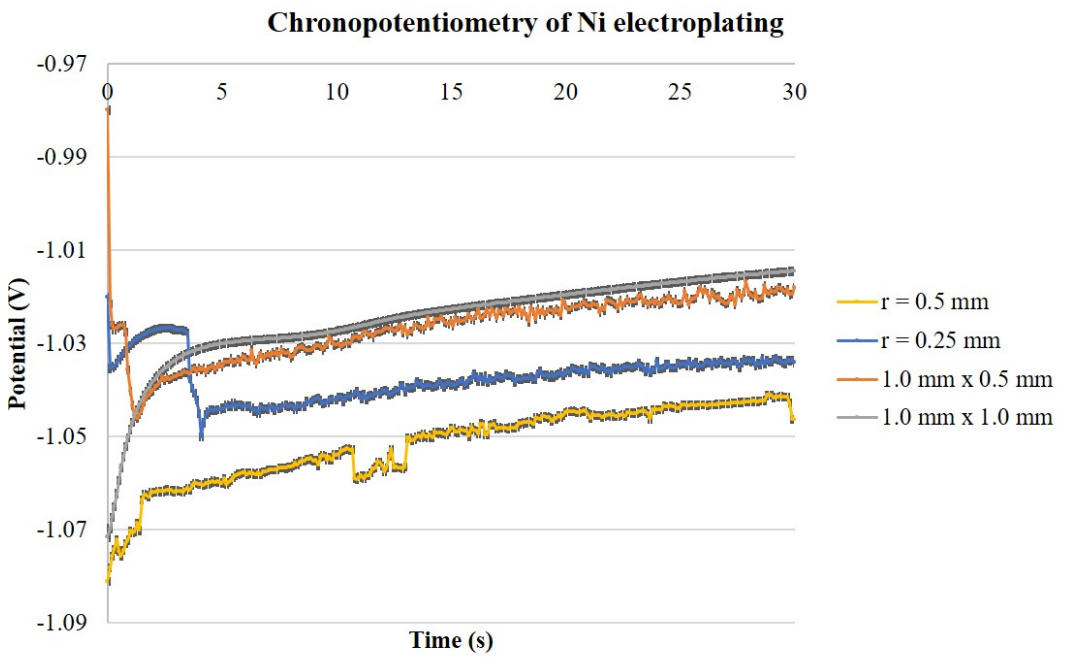

Figure 5.7: Chronopotentiometry of Ni electroplating for circular electrodes with radius = 0.5 mm, 1.0 mm × 0.5 mm rectangular electrodes, 1.0 mm × 1.0 mm square electrodes, and circular electrodes with radius = 0.25 mm

The chronopotentiometry process in figure 5.7 shows different potential changes for four different electrodes when Ni plating was performed to coat a thin layer of 0.2 µm of Ni. The electrode with largest surface area, 1.0 mm × 1.0 mm square electrodes, gave the lowest potential change while the circular electrodes have higher potential change.

5.2.5 Au plating

The Au plating solution was purchased from SPA Plating Ltd. The required electroplating time to obtain 0.5 µm Au plating was calculated using equation 5.1 with the atomic weight of Au, 196.966 569(5) [138] and a current density of 10 mA cm^{-2} for Au plating [137] to have a uniform layer of Au on the electrode tips. The process was repeated for the rest of the electrodes. The calculated current which varied according to

Working electrode	Electrode to be plated
Counter electrode	Pt wire (mesh)
Reference electrode	Ag/AgCl electrode
Software	GPES
Software method	Method > Potentiometry (Galvanostatic)

Table 5.2: Electroplating set-up

the geometry of the electrodes was applied to the electrodes during the electroplating process.

The Au plating tank solution contains potassium cyanide (KCN) which produces poisonous hydrogen cyanide gas when reacting with an oxidising agent [139]. Hence, it should not be mixed with any active oxidising agent and care was taken not to mix it with any other types of acid solution. The Au plating solution consists of 4 g Au in a one-litre solution. The electroplating set-up is summarised in table 5.2.

At cathode, reduction occurred and resulted in deposition of Au^0.

$$Au^+ + e^- \longrightarrow Au^0 \tag{5.3}$$

The Au-plated electrodes and chronopotentiometry of the Au electroplating are shown in figures 5.8 and 5.9 respectively.

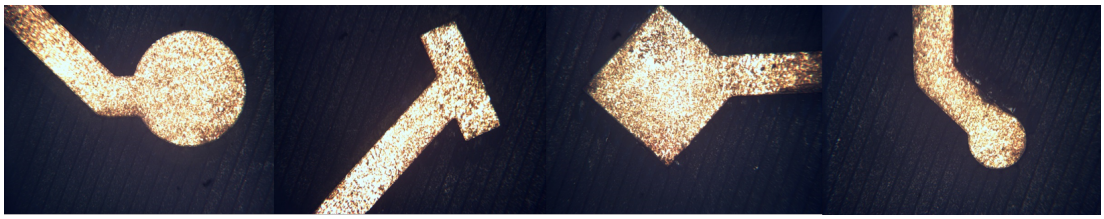

Figure 5.8: Microscopic images of Au-plated EIT electrode designs, from left to right the dimensions are as follows: radius = 0.5 mm (circular electrodes), 1.0 mm × 0.5 mm (rectangular electrodes), 1.0 mm × 1.0 mm (square electrodes), radius = 0.25 mm (circular electrodes)

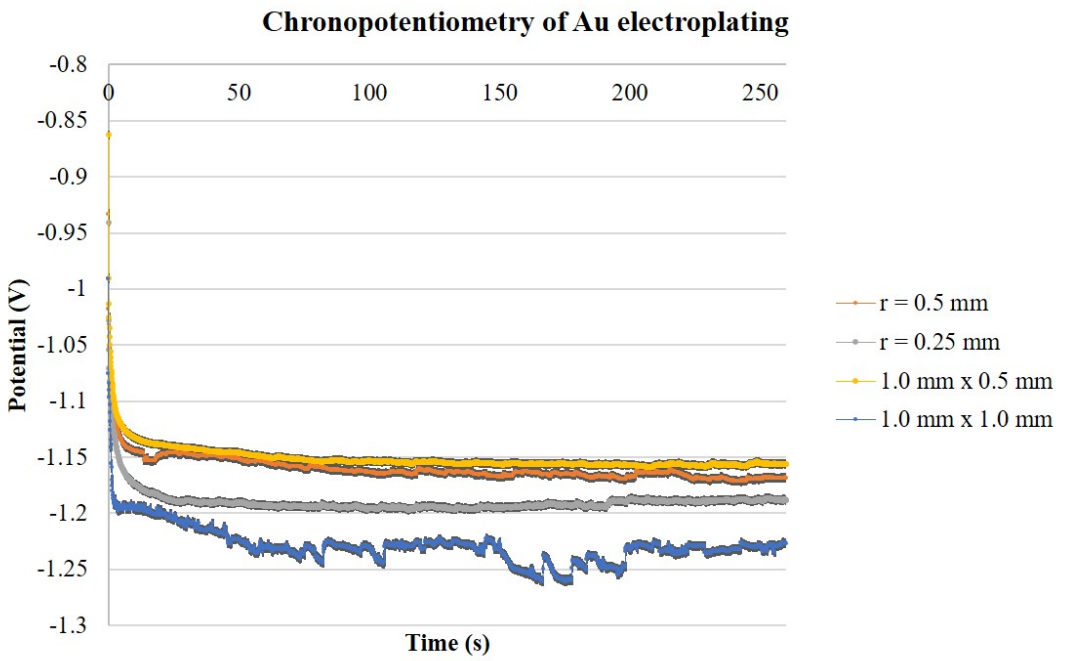

Figure 5.9: Chronopotentiometry of Au electroplating for circular electrodes with radius = 0.5 mm, 1.0 mm × 0.5 mm rectangular electrodes, 1.0 mm × 1.0 mm square electrodes, and circular electrodes with radius = 0.25 mm

The chronopotentiometry graph in figure 5.9 shows different potential changes for four different electrodes when Au plating was performed to coat a thin layer of 0.5 µm of Au. Different electrode has different relationship between the electrode potential (voltage) and time in the chronopotentiometry graph. Unlike Ni plating, the 1.0 mm × 1.0 mm square electrodes has the highest potential change in voltage during Au plating.

A clamp was employed to hold the Ag/AgCl/KCl reference electrode firmly in place as illustrated in figure 5.10. The electroplating process was performed in a Faraday cage that shields the set-up enclosed from external electric fields. Although accurate calculations were performed to obtain the desired electroplating times, there were some minor defects in the Au coating on some of the electrodes.

Figure 5.10: Experimental set-up for Au electroplating in a Faraday cage

Figure 5.11 shows the Au electroplating protocol on Cu.

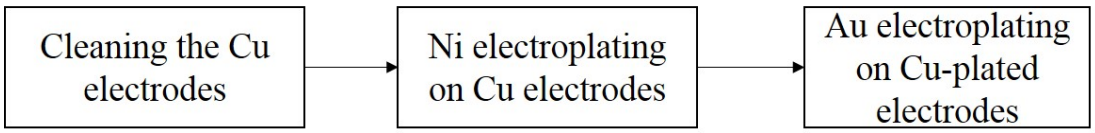

Figure 5.11: Au electroplating procedure on Cu electrodes

5.2.6 Limitations of electrodes on PCB

Due to the millimetre scale sensing area of electrodes on a PCB, it is a challenge using it for micro-scale phantoms, cell spheroids and tissue scaffolds which are a few hundred micrometres in size. Cellular resolution with EIT requires the dimensions of the electrode system to be scaled down. Therefore, the EIT device was scaled down by microfabricating the electrodes on a glass substrate.

5.3 Micro-scale electrode design on glass substrate

In this research, the proposed layout has 16 micro-scale electrodes arranged in a ring surrounding a circular volume which will be imaged using these electrodes specifically designed and fabricated for EIT measurements. The micro-scale electrodes morphology used were 500 µm × 250 µm rectangular, 500 µm diameter circular, 350 µm diameter circular and 500 µm × 500 µm square micro-scale electrodes. The diameter of the fluid chamber attached to each set of sensor electrodes was 6 mm which is the size of a single well in a standard 96-well-plate for cell culture.

5.3.1 Micro-scale electrode fabrication techniques

These micro-scale electrodes for cell culture studies were fabricated on a substrate (glass or silicon) where a conducting layer (typically an unreactive metal such as Au or Pt) was deposited and patterned followed by a passivation layer (Parylene C, silicon dioxide or silicon nitride) deposited over the conducting layer. The fabrication process is illustrated in figure 5.12, while figure 5.13 shows the layout of fabricated electrodes. The passivation layer over the electrodes was patterned to expose the metal and to define the microelectrode area [88].

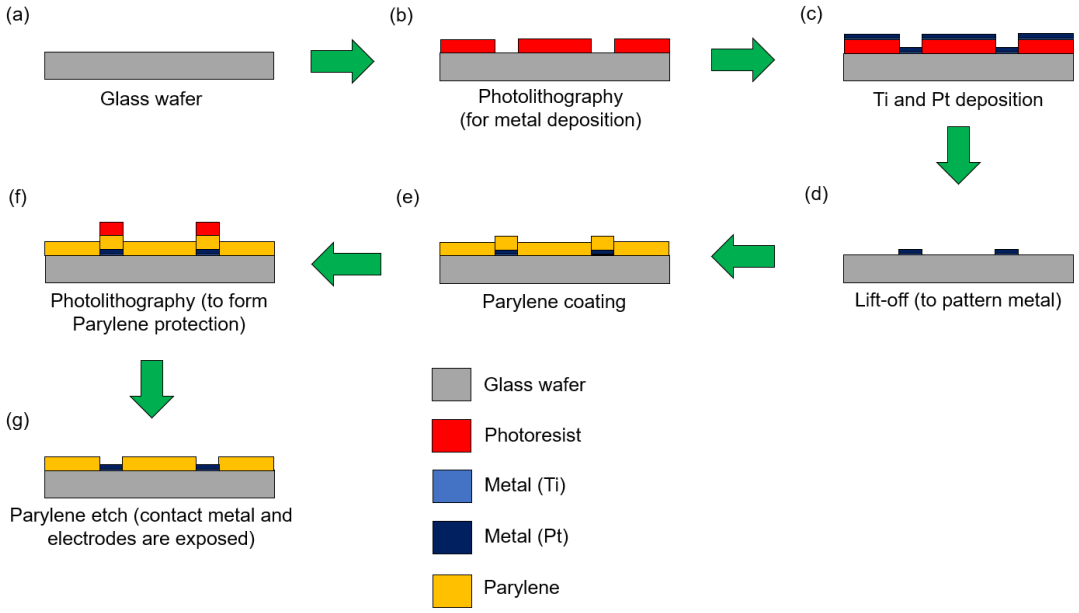

Figure 5.12: Schematic cross sections illustrating the micro-scale electrode fabrication process

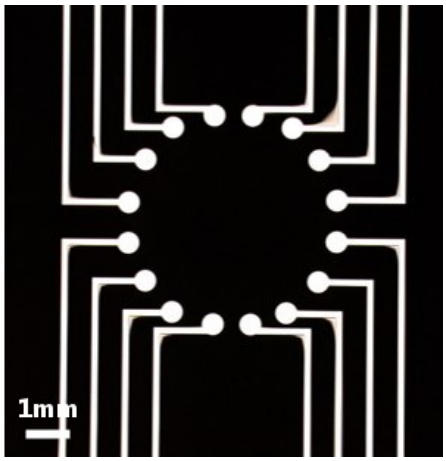

Figure 5.13: 16 micro-scale electrodes with r = 250 µm circular in a ring pattern

5.3.1.1 Wafer cleaning

The substrate used for this research was glass due to its transparency enabling better optical inspection of the cells. The glass wafer was cleaned in Piranha solution to ensure the wafers are clean before commencing the microfabrication process in the cleanroom.

Piranha solution is a mixture of H_2SO_4 and hydrogen peroxide (H_2O_2) that is used

to remove organic materials from the substrate. Since the mixture is a strong oxidising agent, it will remove most organic materials, and will also hydroxylate most surfaces. The mixture used in this research was three parts (210 ml) of concentrated H_2SO_4 and one part (70 ml) of 30% H_2O_2. Peroxymonosulfuric acid (H_2SO_5), a highly oxidising acid, is produced when H_2O_2 has a reaction on H_2SO_4 [140].

Extra care had to be taken while preparing Piranha solution since it is highly corrosive. The mixture of H_2SO_5, H_2O_2 and H_2SO_4 that is corrosive and highly oxidising can react vigorously with organic materials during the cleaning process which could then lead to an explosion. Even when made with care, the resultant heat could increase the temperature to over 100°C. The substrate cleaning took 15 minutes after which the substrate was rinsed with plenty of de-ionised (DI) water followed by nitrogen (N_2) drying.

5.3.1.2 Metal patterning

The photoresist used in this process was AZ nLOF® 2035 (negative resist for metal patterning) from AZ Electronic Materials USA Corporation. The desired thickness was 1.2 µm and the spin speed was set to 4000 RPM. The substrate was then soft baked for 5 minutes at 90°C, before being exposed to UV light for 25 seconds using a photomask on a Karl Süss MA8 mask aligner. After this the glass substrate was placed on the hotplate for one minute at 110°C for a post-exposure bake.

The next step was to develop the photoresist using AZ 726 MIF developer, also from AZ Electronic Materials USA Corp. The dish was agitated to develop the photoresist for around a minute until all unexposed resist was removed. The metal deposition

was performed by using electron-beam evaporation on an ANS cluster tool. 10 nm of titanium (Ti) was deposited as an adhesion layer, followed by 100 nm of Pt.

MICROPOSIT Remover 1165 was used to strip the resist following the metal deposition. The glass wafer was soaked for 10 minutes in MICROPOSIT solution. After 10 minutes, the MICROPOSIT solution was changed, and the wafer was left in the new solution for at least one hour. It was left over an hour to ensure the remaining metal was removed. After one hour, the wafer was rinsed with isopropanol (IPA) and DI water. This step was repeated to ensure any tiny bits of metal on the glass wafer was thoroughly removed. The wafer was then rinsed with IPA and DI water after one hour. The glass wafer was cleaned in O_2 plasma for 5 minutes before Parylene C coating the passivation layer.

The microscopic images of the post-liftoff process are shown in figure 5.14.

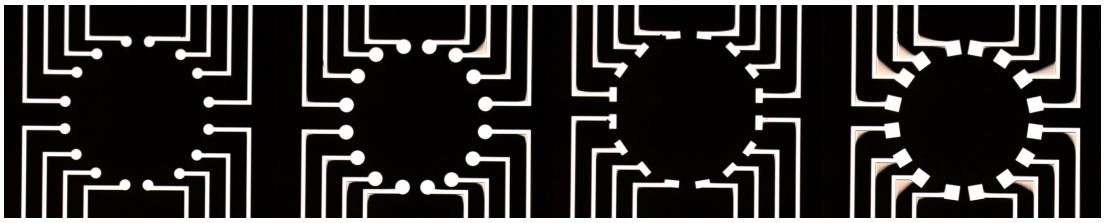

Figure 5.14: Microscopic images of the post-liftoff process. From left to right; 175 µm radius circular, 250 µm radius circular, 500 µm × 250 µm rectangular, and 500 µm × 500 µm square micro-scale electrodes

5.3.1.3 Deposition of passivation layer

Parylene C was used as passivation, and 1.2 µm thick layer was deposited by physical vapour deposition in a SCS Labcoter tool. For thickness measurement, a silicon (Si) chip acting as a reference was placed together with the glass substrate during the deposition process. The Parylene C coating thickness on the Si chip was then measured using a

NanoSpec reflectometer metrology tool that measures the thickness of thin, transparent films on Si.

The deposition of passivation layer has similar process as the metal patterning that was discussed in 5.3.1.2. However, the photoresist used in this process was MEGAPOSIT™ SPR™ 350. The substrate was soft baked for 5 minutes at 90°C, before being exposed to UV light for 5 seconds using a photomask which design is shown in figure 5.15, on a Karl Süss MA8 mask aligner. After this the glass substrate was placed on the hotplate for one minute at 110°C for a post-exposure bake. Parylene C was patterned and etched to expose the electrodes and to create contacts.

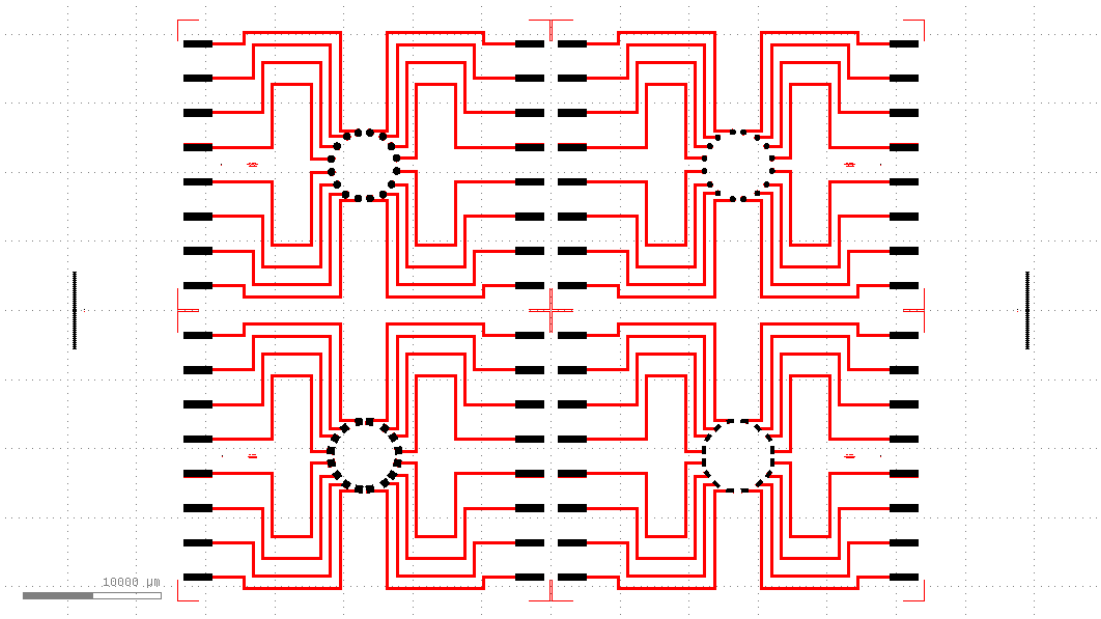

Figure 5.15: Micro-scale electrodes design on a photomask for Parylene C patterning. The red tracks are passivated with Parylene C while the areas in black are etched to create contacts when performing the EIT measurements

The microscopic images of the micro-scale electrodes following post-Parylene C etching process are shown in figure 5.16.

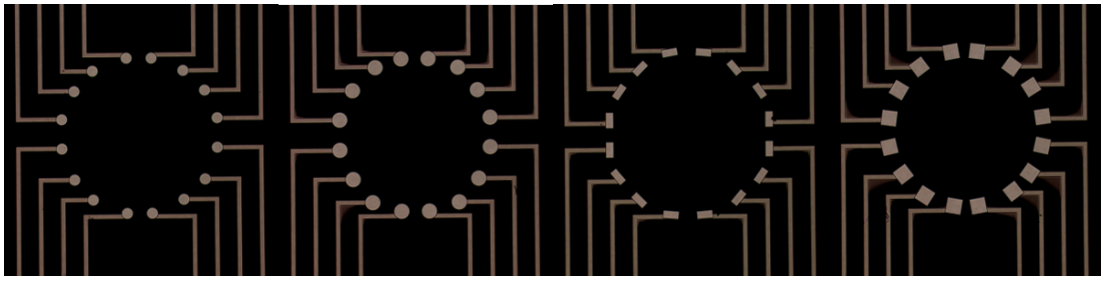

Figure 5.16: Images of micro-scale electrodes after Parylene C etching process. From left to right; 175 µm radius circular, 250 µm radius circular, 500 µm × 250 µm rectangular, and 500 µm × 500 µm square micro-scale electrodes

5.3.1.4 Wafer dicing

Prior to dicing the glass substrate, it was coated with MEGAPOSIT™ SPR™ 350 to protect the Pt electrodes during the dicing process. The sensors were diced and then cleaned in acetone, followed by IPA and as DI water to remove the photoresist (SPR350) coated prior to the dicing process. The sensors were then cleaned in O_2 plasma for 15 minutes. Figure 5.17 shows the Pt electrodes on a glass substrate. The tracks were designed in such way so they all have equal resistance. However, the issues with lift-off process seen in figure 5.14 mean there are small variations. The issue can be improved by cleaving the substrate and using the scanning electron microscope (SEM) to produce the cross-section images of the substrate.

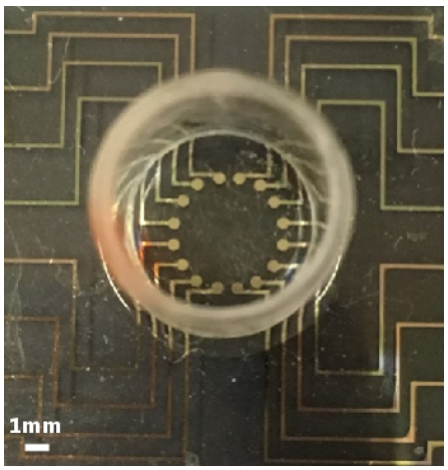

Figure 5.17: Pt micro-scale electrodes on a glass substrate

5.3.2 PCB for Pt micro-scale electrodes connection

A PCB was designed to connect the Pt micro-scale electrodes to the EIT system. The PCB design for the Pt micro-scale electrodes connection was performed using TARGET 3001!, standalone software for PCB layout [141]. Contact problem often arose during the EIT measurements which were known to be caused by the Pogo pin on the socket. Since there are four pieces of PCBs stacking up on top of each other, there were possibilities that either one of the Pogo pin was not in contact with the electrodes hence, disrupting the EIT measurements. The fabricated PCB is shown in figure 5.18

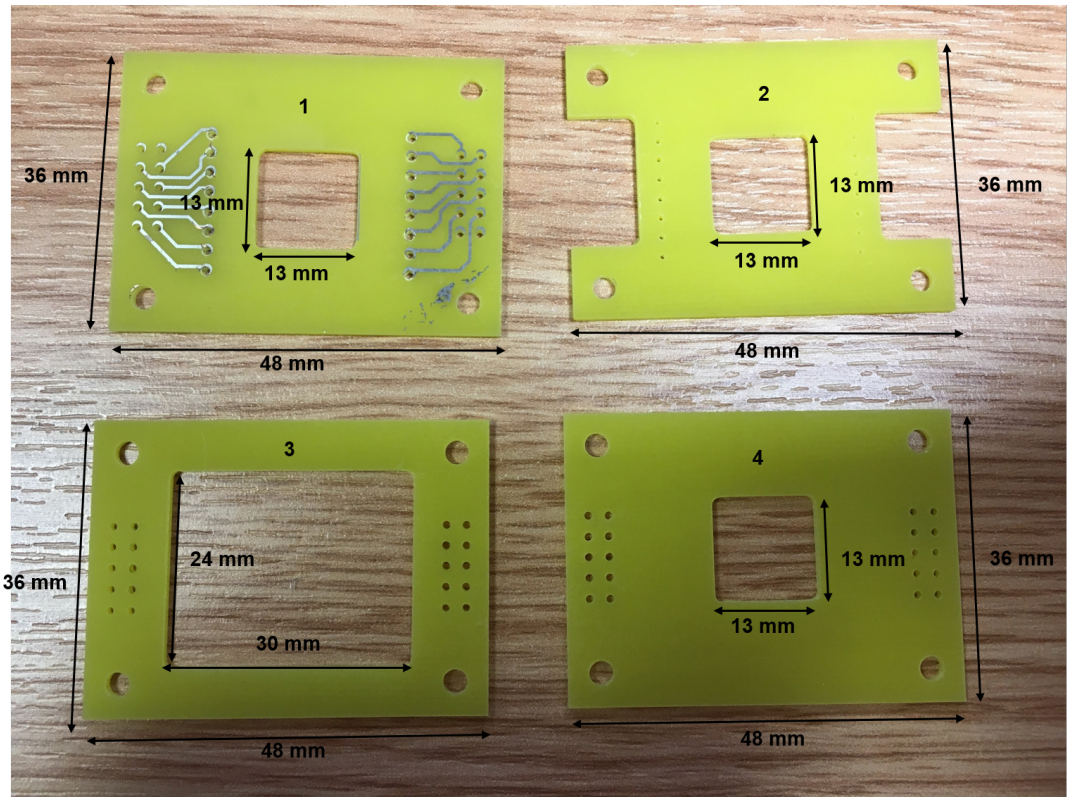

Figure 5.18: The fabricated PCB for Pt micro-scale electrodes connection

Therefore, a new adapter for the Pt micro-scale electrodes was designed, as shown in figure 5.19 where the EIT device microfabricated on the glass substrate was soldered directly on the PCB using thin wires.

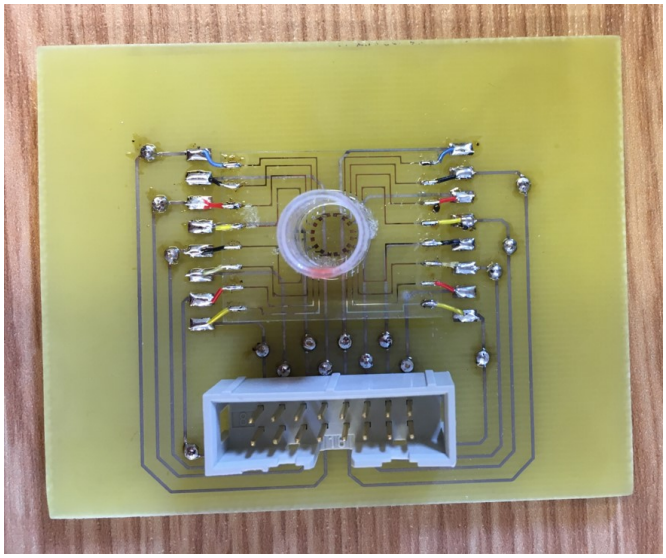

Figure 5.19: EIT device (Pt micro-scale electrodes) directly attached on the adapter PCB

5.3.3 Biocompatibility tests on passivation materials

Materials selection plays an essential role in the design of micro-scale electrodes for micro-bioimpedance tomography. It has to be biocompatible as so not to have any potentially harmful physiological effects [142] during *in vitro* characterisation in the lab. The term 'biocompatibility' was first mentioned in 1970 by R.J. Hegyeli (Amer Chem Soc Annual Meeting abstract) and C.A. Homsy et al. (J Macromol Sci Chem A4:3,615, 1970).

A passivation layer is a coating layer to insulate and act as a barrier to corrosion, thereby preventing damage to the biological system in a biomedical application. It is typically the covering layer of a microelectrode structure and therefore is usually exposed to the biological system, so its biocompatibility is also important. Silicon nitride [143], silicon dioxide [144], photoresist [145] and polyimide [146] [147], are materials commonly used materials as passivation layers. Apart from selecting a passivation material based on dielectric constant and dielectric strength [148], biocompatibility is crucial in cell-

based biosensors. Biocompatibility studies were performed on insulation materials used in this work: silicon nitride, silicon dioxide, and Parylene C. Three 2.0 cm × 2.8 cm chips were diced from silicon wafers for cell adhesion experiments. These chips were coated with either 1 µm of Parylene C (deposited using an SCS Labcoter), 1 µm of plasma enhanced chemical vapour deposited (PECVD) silicon nitride or 1 µm of PECVD silicon dioxide using STS Multiplex PECVD.

The coated chips were treated in an oxygen plasma (Barrel Asher) for five minutes to clean surfaces. They were placed in 60 mm plastic Petri dishes before seeding with a concentration of 2,250,000 cells ml^{-1} of MCF7 breast cancer cells. As a control, MCF7 cells were also cultured directly in a 60 mm Petri dish. All Petri dishes were incubated for five days before comparing the cell viability of the different materials.

Table 5.20 shows that the Parylene C coating has the highest cell density compared to silicon dioxide and silicon nitride, making it the most suitable passivating material for MCF7 cells.

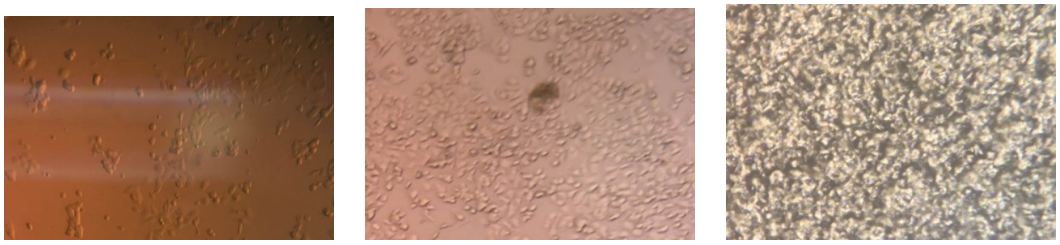

Figure 5.20: Optical images of cells after culturing: (left) silicon nitride (centre) silicon dioxide and (right) Parylene C

The trypan blue cell viability protocol was followed to discriminate between viable and non-viable cells. Trypan blue solution is a dye used to determine between live and dead cells. The trypan blue solution was added directly to the trypsinised cell suspension in a 1:1 0.4% trypan blue solution to the cell suspension. After 5 minutes, dead cells

were stained. Cells cultured on silicon nitride have the lowest percentage of live cells while Parylene C exhibits the highest rate of live cells as shown in figure 5.21.

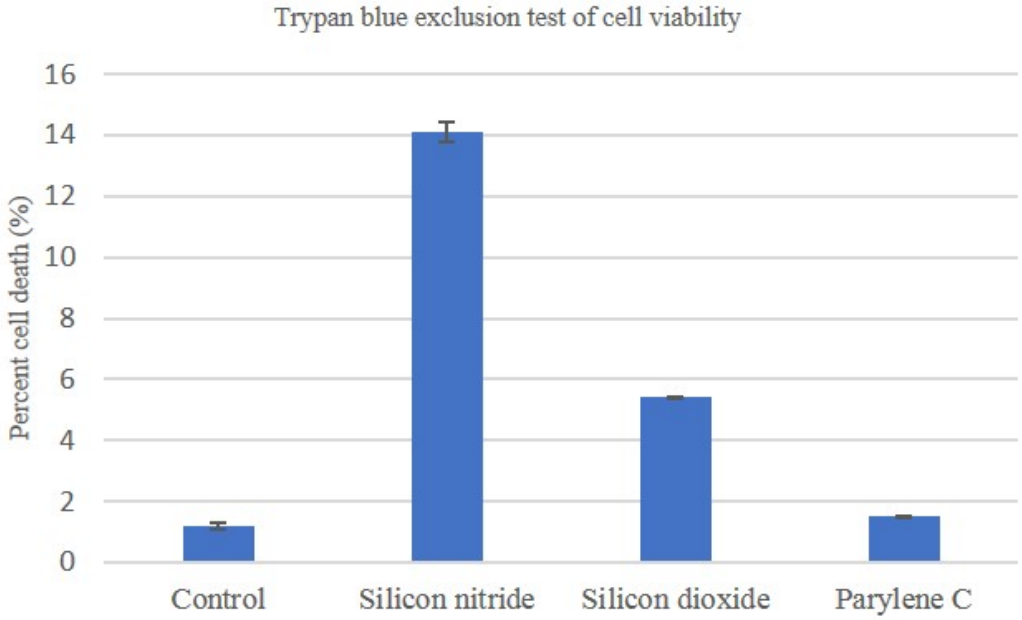

Figure 5.21: Trypan blue staining test results with different passivating materials to test cell viability. The error bars represent standard deviation

5.4 Flexible Micro-scale Electrode Arrays (Flex-MEAs) design

The idea of the Flex-MEA is to create a 3D ring of electrodes to incorporate the EIT with 3D cell structures. When electrodes are on the chamber wall, an electric field is evenly distributed within the 3D cell structure in the chamber, hence, resulting in precise sensitivity.

The dimension of the Flex-MEA used is 36 mm in length and 27 mm in width. The Flex-MEA was fabricated by Merlin Flex Ltd on a polyimide with Au micro-scale electrode array. The material stack-up of our Flex-MEA is shown in figure 5.22. The

Flex-MEA is comprising 25 µm adhesive and polyimide with 18µm Cu. It is protected with 12.5 µm polyimide coverlay and thickened in the Zero Insertion Force (ZIF) contact area with additional polyimide to give a finished thickness of 0.3 mm. The general thickness on the rest of the Flex-MEA is 0.0805 mm.

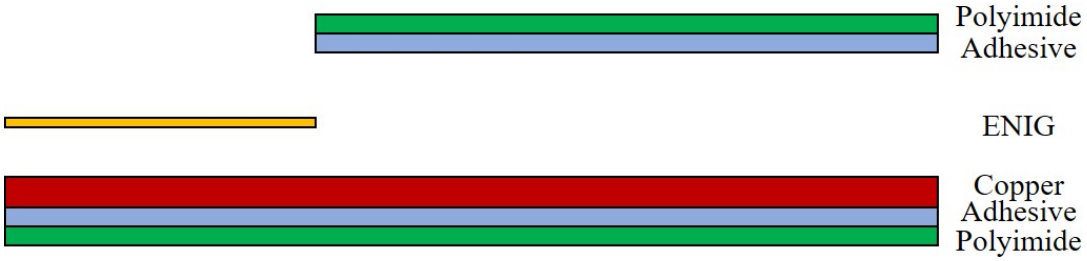

Figure 5.22: The material stack-up of a single layer flex with ZIF feature

The Flex-MEA used in this work was designed to ensure all pairs of electrodes gave the same cell constant, K, which unit is cm^{-1} [149]. Cell constant is the ratio of the distance between the electrodes, d, to the affective area of the electrodes, a.

$$K = \frac{d}{a} \tag{5.4}$$

It relates the conductivity of the sample, κ:

$$\kappa = GK \tag{5.5}$$

where G is conductance, unit measurement is siemens, (S) and is the reciprocal of resistance, R.

$$G = \frac{1}{R} \tag{5.6}$$

Therefore, when a homogeneous sample is probed, all pairs of subsequent electrodes produce identical results. When measuring an inhomogeneous sample, the impedance then gives a measure of the mean resistivity of the sample down to a depth equal to the electrode spacing.

By maintaining the ratio between the interelectrode spacing, s, and the micro-scale electrodes pitch, d, constant, all the micro-scale electrode pairs have the same cell constant. The evolution of Flex-MEA started with millimetre-scale planar electrodes fabricated on a PCB to micrometre-scale planar electrodes fabricated on a glass substrate and now improved further by having an electrode arrangement on a flexible material. With the improved Flex-MEA design, every electrode will have different resistance due to variation in track lengths as shown in figure 5.23

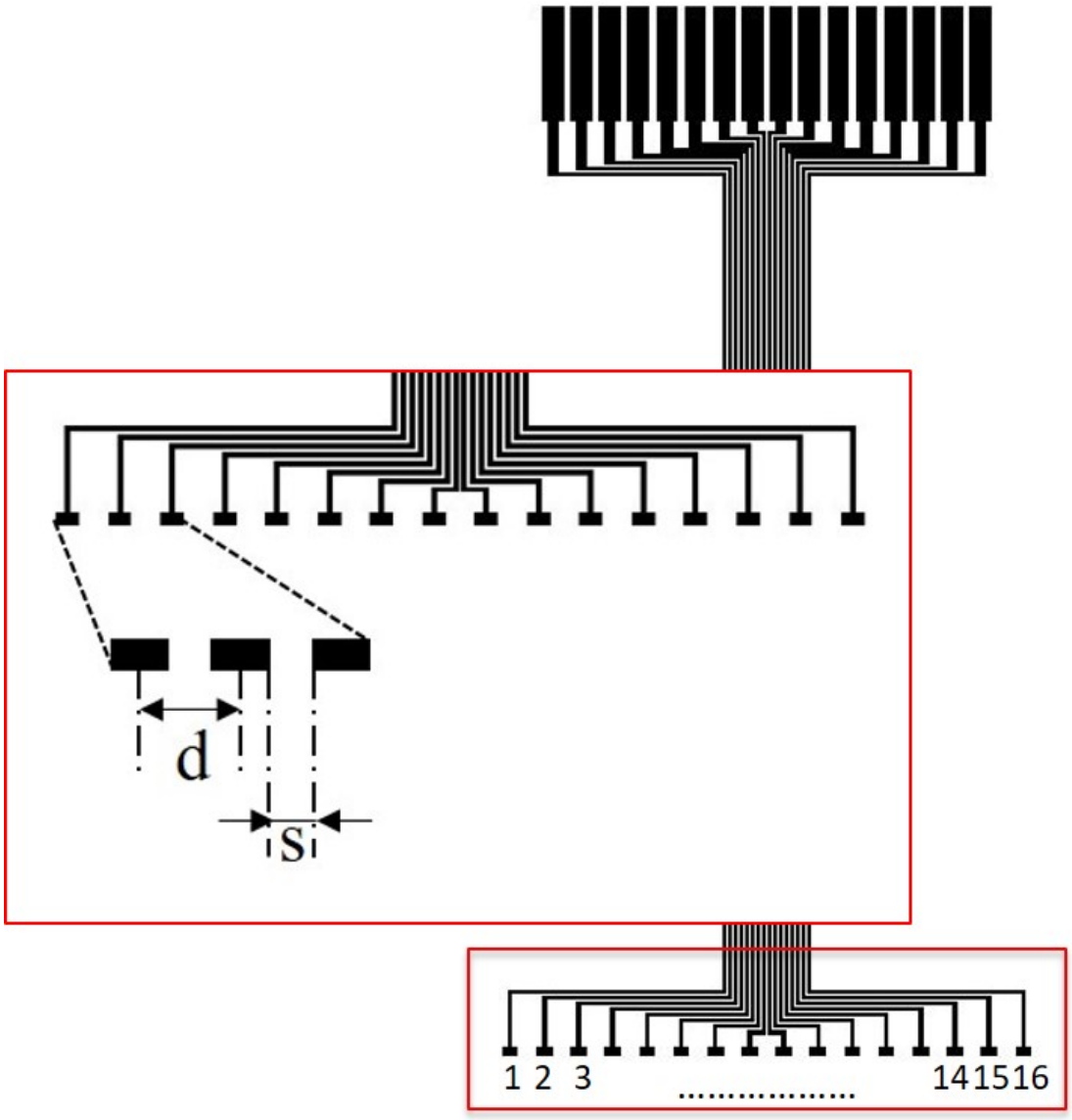

Figure 5.23: The Flex-MEA design

The dimension of each micro-scale electrode is 500 µm in length and 250 µm in width. The lines and pads will be accurate in size to ±25 µm, resulting in 475 µm to 525 µm for the Au micro-scale electrodes and ranging between 675 µm to 725 µm for the interelectrode spacing with 3 - 5% tolerance.

The electrode and track dimensions on the Flex-MEA are summarised in table 5.3.

Micro-scale electrodes pitch, d	1200 µm
Interelectrode spacing, s	700 µm
Micro-scale electrodes length	500 µm
Spacing between long tracks	100 µm
Tracks pitch	200 µm

Table 5.3: Flex-MEA dimension

The fabricated Flex-MEA is shown in figures 5.24 and 5.25 from top and bottom respectively. The flexibility enables it to be fitted in either the fluid chamber or conventional multiwell culture plates.

Figure 5.24: Top view of the PCB

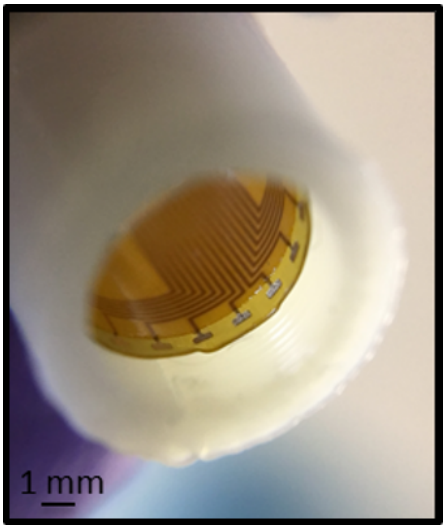

Figure 5.25: Bottom view of the PCB adapter PCB when placed in a fluid chamber

Since we are dealing with small resistance measurement, an adapter printed circuit board (PCB) has been fabricated to attain equal and precise resistance measurement for all 16 electrodes. This is further discussed in 5.4.1.

5.4.1 PCBs to EIT system adapter PCB

The adapter PCB design for the PCBs was also performed using TARGET 3001!, a standalone PCB layout CAD software [141]. Since EIT is a relationship between conductivity variation, $\delta\sigma$ and the potential difference, δV, in a sensing field, it is essential to keep the resistance value across the PCB to the EIT system identical for all the micro-scale electrodes.

The PCB trace resistance for each micro-scale electrode is defined in the equation below

$$R = \rho\frac{L}{tW}[1 + \alpha(T - 25)] \tag{5.7}$$

where:

ρ = resistivity ($\rho_{Cu} = 1.7 \times 10^{-8}$ Ωm)

L = track length, m

W = track width, m

t = track thickness, m

T = temperature in Celsius, C

α = temperature coefficient in C^{-1}

Since it is challenging in equalising the resistance on Flex-MEA due to the restricted space, the width and length of tracks on the adapter PCB as shown in figure 5.26 have been adjusted as to attain equivalent resistance for each micro-scale electrode.

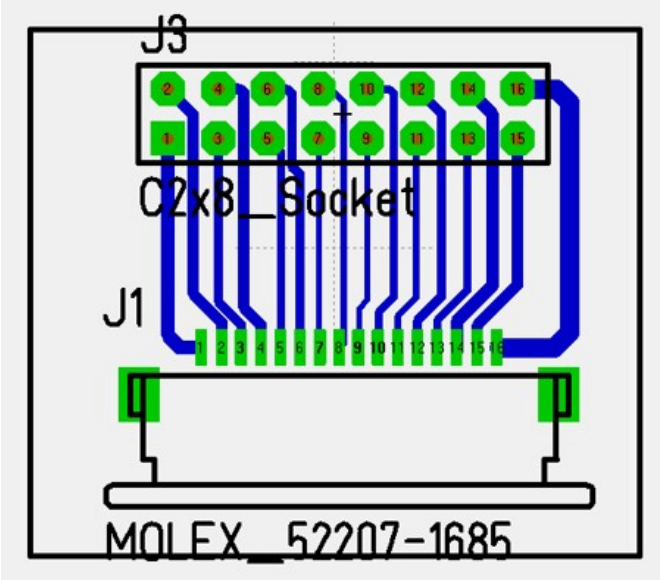

Figure 5.26: PCB adapter PCB

It is important to keep the series resistance identical for all the electrodes on a PCB. Table 5.4 shows the electrode calculated and measured resistance on flexible PCB, adapter PCB and its total resistance with 10% – 22% percentage error.

Table 5.4: Resistance value of each electrode, E1 to E16

	Calculated resistance			Measured resistance			
	Flex-MEA (mΩ)	**Adapter PCB (mΩ)**	**Total (mΩ)**	**Flex-MEA (mΩ)**	**Adapter PCB (mΩ)**	**Total (mΩ)**	Error (%)
E1	492	15	507	381	26	407	19
E2	475	32	507	368	28	396	21
E3	472	35	507	354	59	413	18
E4	442	65	507	340	93	433	14
E5	435	72	507	326	116	442	12
E6	395	112	507	312	148	460	17
E7	378	129	507	298	144	442	12
E8	378	129	507	283	169	452	10
E9	378	129	507	283	170	453	10
E10	378	129	507	298	128	421	16
E11	395	112	507	312	101	413	18
E12	435	72	507	326	85	411	18
E13	442	65	507	340	69	409	19
E14	472	35	507	354	42	396	21
E15	475	32	507	368	28	396	21
E16	492	15	507	381	12	393	22

Since it was a low resistance measurement, a four-wire resistance approach was implemented to reduce the effect of test lead resistance. With this approach, voltage was forced through one of the test probes and current is measured through the sense probe for each electrode. The various percentage error was presumably due to the fabrication process to accommodate different values of length and width.

The adapter PCB was fabricated using standard PCB fabrication process shown in figure 5.27. Firstly, the required circuit was designed and printed as 1:1 artwork onto an acetate sheet using a laser printer. The Gerber file was imported to the computer numerical control (CNC) machine for drilling of the PCB. At this stage, the machine drilled all the holes on the photoresist coated PCB. The printed artwork was next attached on the PCB for UV exposure. It is very vital to ensure that the board is fully exposed during UV exposure. The exposure time taken was 100 seconds, and we had to be careful of the timings. If the resist is not exposed for long enough, it will be difficult to develop it all away.

The developer solution was prepared by mixing 50 ml of Mega Electronics 600-010 Seno 4006 to 950 ml parts of DI water to make a 1-litre solution resulting in a 19:1 mix. The temperature applied was ranging between 40°C – 50°C and the time taken to develop the photoresist was 60 s.

The PCB was cleaned and washed under running water in between the processes. It was then placed in the etching tank containing ferric chloride at 40°C – 50°C for 7 minutes. The process left the Cu tracks with photoresist on them that was stripped off using PC155 resist strip solution for 5 minutes. The solution was prepared by mixing 1 litre of PC155 to 4 litres of DI water.

The PCB was immersed in the tin plating solution for 5 minutes before it starts to oxidise. The PCB was then immersed immediately in cold water and thoroughly rinsed and wiped dry before they were ready for the experimental works.

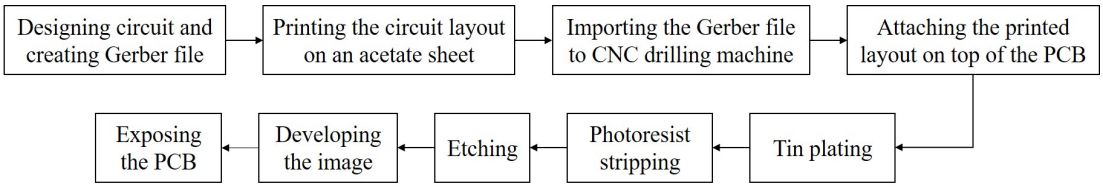

Figure 5.27: Adapter PCB fabrication process

5.4.2 Fluid chamber and plate

A 6.4 mm diameter fluid chamber was designed and printed on a 3D printer mimicking the dimension of a 96-well cell culture plate individual well. The fluid chamber was fitted in a 40 mm x 25 mm x 3 mm acrylic plate, as illustrated in figure 5.28 to hold it in place.

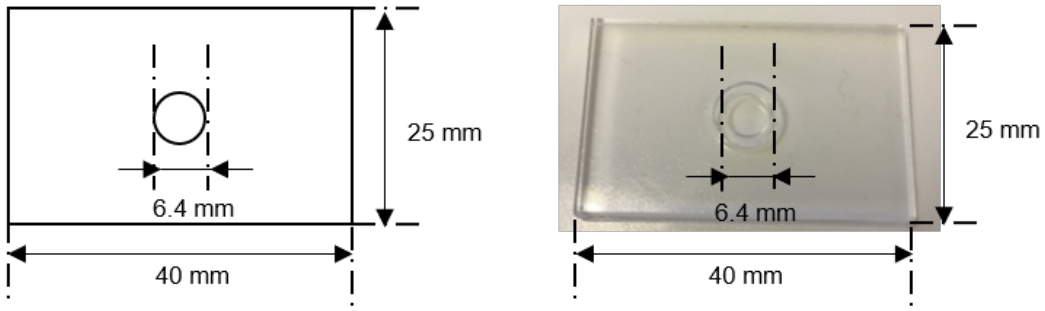

Figure 5.28: (Left): Drawing of arcrylic plate where the fluid chamber is attached at the centre of the arcrylic plate. (Right): Photo of the chamber arcrylic plate

The equipment used to machine the parts was a 3-axis milling machine (XYZ SMX 3500). The finish was achieved using a 1.5 mm diameter end milling cutter ran at 4000 RPM (revolutions per minute). As acrylic is a soft material, a high RPM was required, and the feed rate was 400 mmpm (millimetres per minute). The feed rate determines

how quickly it will move on the X and Y axis to make the circle profile needed to fit the fluid chamber.

5.5 Sterilisation technique

Sterilisation, especially for medical devices, is important to avoid any exposure to infections [150] when the devices are in use. Therefore, before moving to perform any experimental work, the PCB was placed in an autoclave and heated through pressurised steam to decontaminate and kill all microorganisms including bacterial spores. The part being exposed to steam at 121°C for 15 minutes. EIT measurements were performed for post-sterilisation test on a 27mm^3 cube made from ABS, non-conductive material and 5 mm x 1 mm metal disc. PBS was used as a reference, and it seems that the sterilisation method did not affect the PCB's functionality as the reconstructed images shown in figure 5.29 give the precise representation of the experimental set-up.

Colour bar in the figure represents resistivity. Since sensitivity is higher at the electrodes, resistivity was observed to be lower at the centre of the fluid chamber where an ABS cube was placed in, hence was unable to reconstruct the third edge of the cube perfectly. The reconstructed image for metal disc after sterilisation however matches the experimental set-up and represents a high conductivity value at the area in the fluid chamber where the metal disc was placed in.

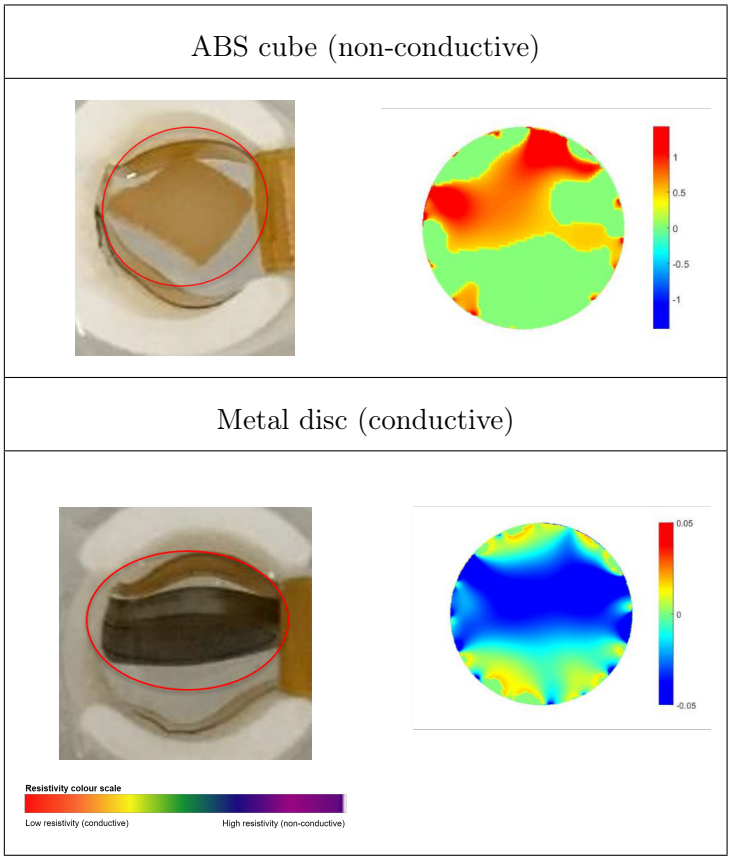

Figure 5.29: Reconstructed images for the post-sterilisation test performed on ABS cube and metal disc

5.6 Summary

First micro-scale electrode design was fabricated on a PCB (millimetre-scale) for micro-bioimpedance tomography of cell spheroids and 3D tissue cultures. The second electrode design was scaled down to micro-scale electrodes on a glass substrate. These two designs represent the planar electrodes. The final micro-scale electrodes design was fabricated on a flexible PCB, proposing a different electrode orientation compared to the planar electrodes.

The compatibility of PCB in a 96-well cell culture plate makes EIT measurements

of a cell spheroid possible in an individual well without having to transfer the spheroid to a separate chamber. Apart from providing a time-efficient method, it prevents from mishandling during the spheroid transfer. The post-sterilisation test shows the PCB does not lose its functionality after being exposed to pressurised steam at 121°C for 15 minutes.

Chapter 6

Micro-bioimpedance tomography measurements and analysis

6.1 Introduction

A medical standard compliant, compact, high speed, 3D multi-frequency Electrical Impedance Tomography (MFEIT) system for real-time 3D biomedical imaging has been developed by the Agile Tomography Group at the University of Edinburgh [151] and is used in this research for the measurements of micro-bioimpedance tomography of cell spheroids and microbial cultures. Several advanced features are implemented in this system to enable high-performance impedance spectroscopic imaging. It contains 32 electrode interfaces, and the supported frequency range operates from 10 kHz to 1 MHz. There is also a fully adjustable current source with current real-time monitoring and emergency switch-off functions. A flexible switching scheme has been developed to enable individual sensing strategies. Real-time 3D imaging software, Visual

Tomography, has been developed for rapid 3D image reconstruction, data analysis, visualisation and parametric configuration. The highest attainable signal to noise ratio is 82.82 dB on a 16-electrode sensor, and the system can achieve up to 1014 frames per second at semi-parallel data acquisition for a real-time imaging [151]. In semi-parallel mode, the differential voltages between adjacent electrodes are simultaneously recorded for each current carrying electrode pair [152].

6.2 Micro-bioimpedance tomography of *in vitro* characterisation on cell spheroids on Pt electrodes

6.2.1 Experimental work

6.2.1.1 MCF7 cells culturing

MCF7 cells were cultured for micro-bioimpedance measurements and grown into cell spheroids. These human breast cancer cells, which are adherent and typically cultured while attached to a surface [153], are readily available in the Tissue Culture Lab, at The University of Edinburgh. The complete culture medium for MCF7 contains 85% Dulbecco's Modiffied Eagle Medium (DMEM) high glucose, 15% Fetal Bovine Serum (FBS), 1% 20 mM L-glutamine and 1% penicillin-streptomycin [154]. A high glucose medium was used to stimulate the proliferation of MCF7 cells while FBS is the source of natural growth factors and hormones needed for cell growth and proliferation. L-glutamine, an essential amino acid, is included in the DMEM composition for the cells to be cultured longer while penicillin-streptomycin is a mix of antibiotics added to prevent any bacterial contamination.

2D cells are cultured until they are 90% confluent prior to spheroid processing. The medium starts changing its colour to orange usually after 48 hours, due to the changes in solution pH the cultured cells consuming nutrients from the medium. Hence, the flask medium was replaced with fresh medium to replenish the nutrients. The cell culture medium had to be replaced twice a week due to the change in its pH value and was changed when the cells were not yet confluent.

A T-25 flask requires 4 ml of medium. The old medium was removed from the flask using a pipette and disposed into a beaker filled with Virkon®, a disinfectant based on peroxygen compounds that has a wide spectrum of activity against bacterial spores [155]. The flask was then filled with 4 ml of fresh medium. The flask was orientated in a horizontal position in the incubator. When the cells had reached 90% confluency rate as shown in figure 6.1, the splitting process then took place.

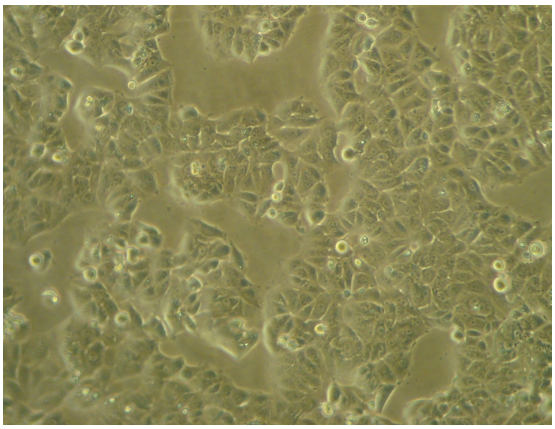

Figure 6.1: MCF7 cells at 90% confluency rate

Splitting involves lifting the cells from the surface and one way to do that is to use trypsin. For a T-25 flask, 0.5 ml 0.25% w/v trypsin solution is added to 1.5 ml of fresh growth media which makes up a 2 ml solution to detach the cells. For the splitting ratio of 1:5, 0.4 ml of the growth media with cells were transferred to a new T-25 flask which

was filled with 3.6 ml of medium before the suspension transfer that made up the 4 ml of solution in the T-25 flask.

The ratio 1:5 is empirical for the lab and culture conditions. Basic rule of thumb is splitting the cells in such a way that they will reach an ideal confluency or sub-confluency by the time of the next split which typically every other day. However, splitting can be performed in higher ratio which brings to less cells trypsinisation for example, twice a week. In order to ensure the cells have regular proliferation, the cells need to have normal population doubling with regular split as cells do not like to be too diluted and over confluent.

For every individual cell culture flask after the trypsining process, the passage number for the flask was increased by one, i.e. 'P41' if the cells were taken from the flask labelled 'P40'. Observation on the MCF7 cells after trypsining can be seen in figure 6.2 where the cells are rounded and suspended in 0.25% w/v trypsin solution.

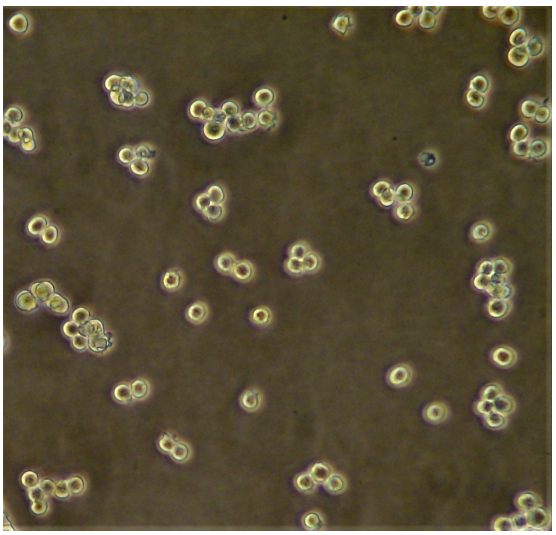

Figure 6.2: MCF7 cells after the trypsinising process

However, there were times when the cell culturing did not work right as exemplified in figure 6.3. A clump observed in the flask were presumed to be dead cells which were

not proliferating after three days. The flask containing MCF7 cells had to be agitated after they were trypsinised to avoid the same incident from happening again. This is to ensure single cells in culture medium did not attach to one another and they were non-adherent. When single cells were still attached to one another after trypsinisation, this resulted the cells to form clumps.

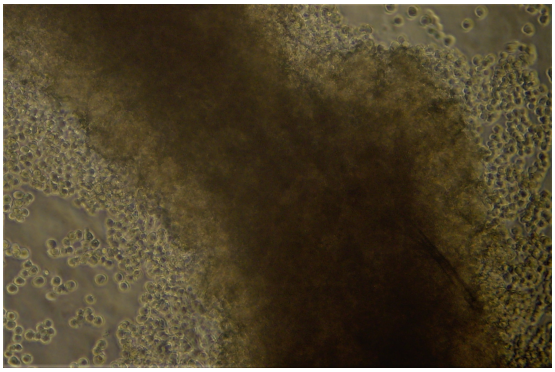

Figure 6.3: Dead cells observed in the flask

6.2.1.2 Spheroids processing

Figure 6.4 shows the culture protocol of MCF7 spheroids. When the cell density has reached 90%, the flask surface was washed with 1 ml PBS to remove as many extracellular proteins as possible. The PBS was then removed, and the flask was filled with 0.25% w/v trypsin solution to dissociate the cells. A single cell suspension had been obtained when the cells were observed to be detached from the flask surface. The cell suspension was transferred to a sterile 15 ml centrifuge tube and centrifugation took place at 1,200 RPM for 5 minutes. The supernatant was discarded carefully, so the cell pellet was not removed. The cells were re-suspended in 1 ml of fresh growth medium, and 10 µl was taken out for cell counting using a Haemocytometer.

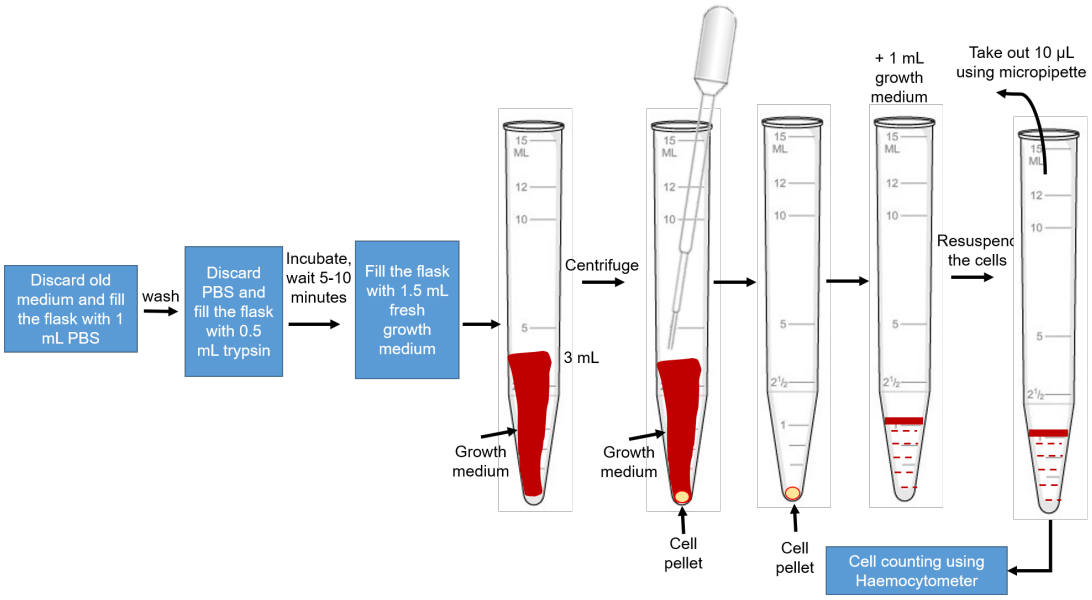

Figure 6.4: Graphical representation of MCF7 spheroids culture protocol

To process MCF7 spheroids, 100 µL cell suspension was pipetted into a Corning® spheroid 96 well microplates shown in figure 6.5. Because the spheroid microplate has a round bottom and not a flat bottom, the cells are formed as spheroids as illustrated in figure 6.6.

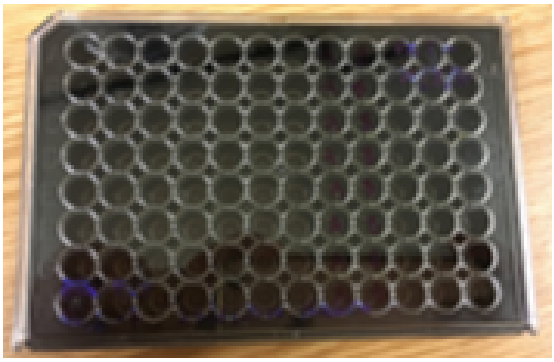

Figure 6.5: Corning spheroid 96-well Corning® spheroid microplate used in the spheroids processing

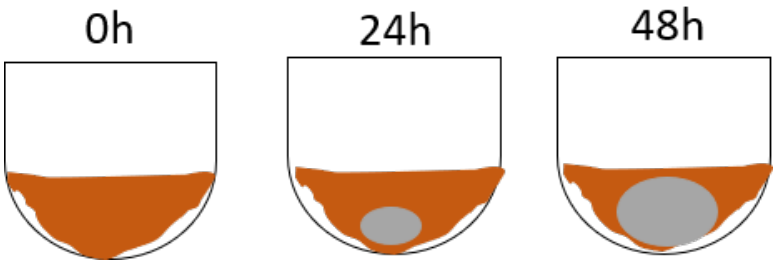

Figure 6.6: Illustration of the spheroid formation after 48 hours

Three cell concentrations were prepared; 60,000 cells ml^{-1}, 120,000 cells ml^{-1} and 240,000 cells ml^{-1}. 100 µl of cell suspension was dispensed to three wells of 96-well Corning® spheroid microplate for each concentration. The spheroid growth for each concentration is shown in the graph in figure 6.7.

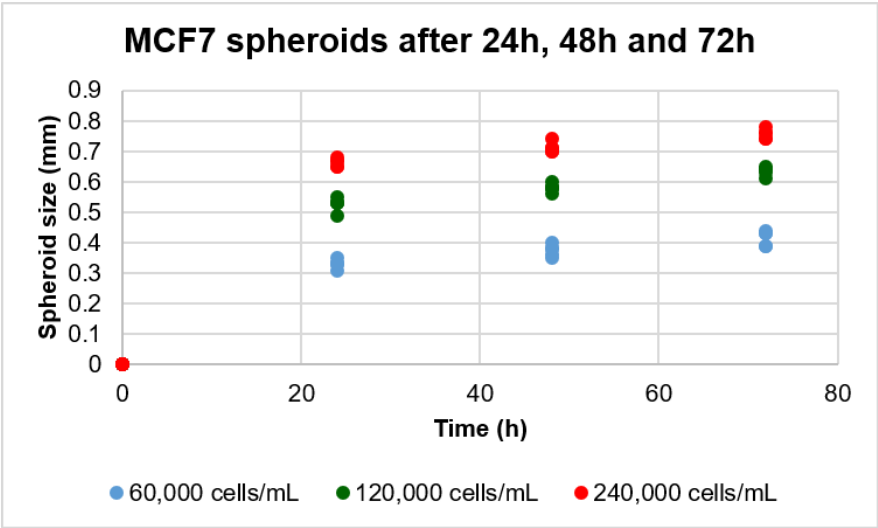

Figure 6.7: The MCF7 spheroid growth (in size) for three cell concentrations, 60,000 cells ml^{-1}, 120,000 cells ml^{-1} and 240,000 cells ml^{-1} over 72 hours

The spheroid microplate was placed in an incubator set at 37°C with 5% CO_2 and spheroid formation as well as growth was visually observed after 24, 48 and 72 hours. The MCF7 spheroids are at their stable growth condition after three days of seeding. The spheroid size is determined using ImageJ where the microscope images of MCF7 spheroids were analysed to define the spheroid diameter. For spheroids with non-

spherical shape, the size is determined by taking the average length between different points around the perimeter as described in figure 6.8.

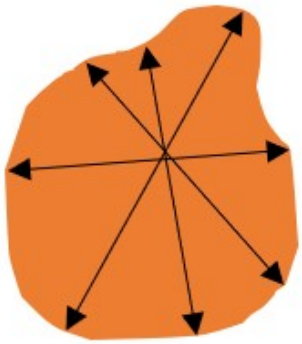

Figure 6.8: Average length between different points are taken to determine the size of a non-spherical spheroid

Figure 6.9 shows microscope images of spheroid formation from each of these concentrations.

60,000 cellsml^{-1} (0.43 mm)	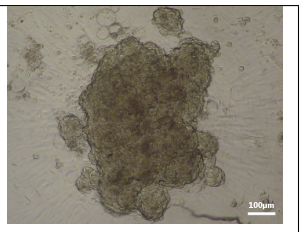
120,000 cellsml^{-1} (0.64 mm)	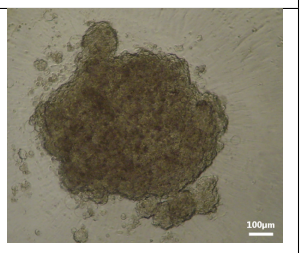
240,000 cellsml^{-1} (0.74 mm)	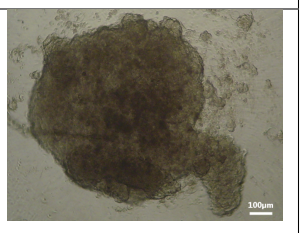

Figure 6.9: Spheroid formation and growth: 60,000 cells ml^{-1} (0.43 mm), 120,000 cells ml^{-1} (0.64 mm) and 240,000 cells ml^{-1} (0.74 mm)

6.2.1.3 Viability tests

A viability test was followed using trypan blue. In this process, the medium in the flask was discarded and washed with 1 ml PBS. The cells were then trypsinised with 0.5 ml 0.25% w/v trypsin solution and incubated at 37°C with 5% CO_2 for 5 minutes. With a 1:1 ratio of cell suspension to trypan blue, 0.5 ml 0.4% trypan blue solution was added to the flask. Observation under a microscope was performed after 4 minutes. In a trypan blue exclusion test, the dead cells took up trypan blue as shown in figure 6.10.

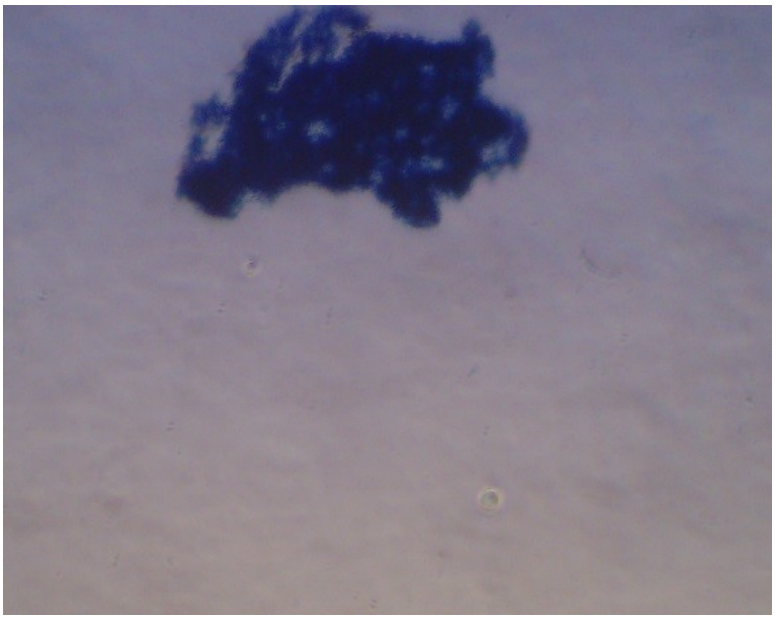

Figure 6.10: Trypan blue viability test

The trypan blue cell viability protocol was essential for biocompatibility tests for passivating materials. Biocompatibility studies were performed on silicon nitride, silicon dioxide, and Parylene C as previously discussed in section 5.3.3.

6.2.1.4 Effects of sodium bicarbonate on cells proliferation

The cells available in the lab are usually cryopreserved by storing the cells at -80°C. In order to culture frozen cells, the standard protocol starts by thawing them then, pelleting them by centrifugation at 1,200 RPM for 10 minutes before transferring the pellet into a flask filled with growth medium from the centrifuge tube. Two different growth medium were prepared to study the effects of sodium bicarbonate on cells proliferation. Both flasks were kept in the 37°C 5% incubator, and daily observation was recorded. The standard complete MCF7 growth media consists of 85% DMEM from Sigma-Aldrich, high glucose), 15% FBS, 1% penicillin/streptomycin, and 1% 20mM L-glutamine.

Flasks #1 and #2 have the same number of cells. On day 2, few cells were seen attached to the surface of flask #1 before replenishing the growth medium. The cells were proliferating but in minimal quantity. When the cells had reached 50% confluency rate on day 5, the growth medium was renewed. The cell's proliferation was observed to be rather slow which could be caused by the cells having been frozen. The confluency rate was 55% on day 6 and 60% on day 7.

The growth rate of MCF7 is low meaning which, the average doubling time is 48 hours. In addition to that, it is normal for frozen cells to double up their average time as the cells are still in shock when transforming from a frozen to a typical environment. The cells were 70%, confluent on day 8 and the flask was restocked with fresh growth medium. As soon as the cells had achieved 80% confluency rate on day 9, the cells were sub-cultured into three T25 flasks for further experimental work.

Observation on flask #2 shows the cells did not look healthy. However, the growth medium was renewed and on day four after the cells were cultured, they seemed to look

more like unhealthy cells. Very few cells were attached to the flask surface resulting in an inadequate confluency rate even after five days.

Even though the growth medium in flask #2 contained sodium bicarbonate, this should not significantly affect the cell proliferation as sodium bicarbonate is used as a buffer to regulate pH. The observation made on day seven exhibits low cell proliferation. Nevertheless, the flask was renewed with fresh growth media.

Different growth medium composition clearly affects cell proliferation. After 4-5 days, the cells in flask #1 reached 50% confluency. However, cells in flask #2 did not seem to thrive. The cell's proliferation for both conditions is shown in figure 6.11.

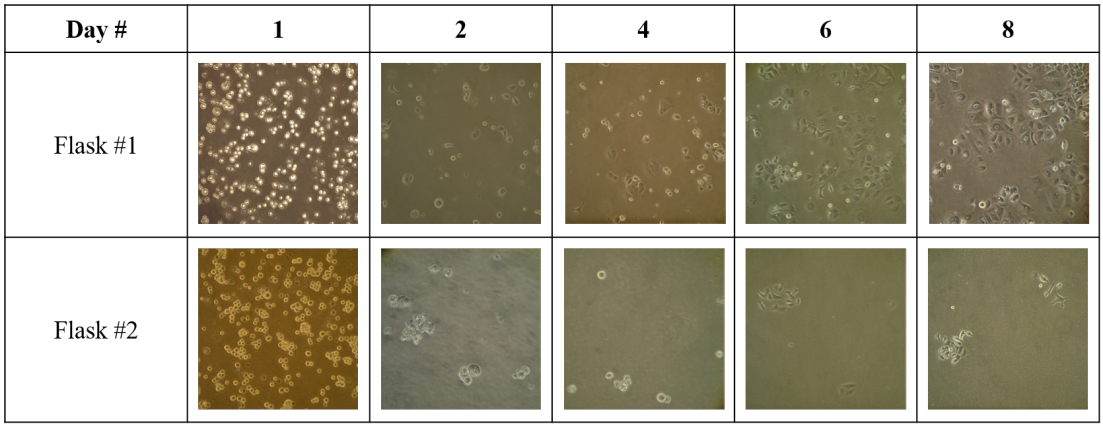

Figure 6.11: Cells proliferation with different composition of growth medium

6.2.1.5 Biological waste disposal

Without proper biological waste disposal, the hazardous material has the potential to harm as it can spread disease, impact the water supply, and environment. Disinfecting is one of the steps in biological waste disposal, and it is a process to decrease the number of organisms where it will not be harmful to health. Tissue culture waste from the experimental works was mixed with 3% Virkon solution to disinfect. The waste was

left overnight before flushing the contents to drain with plenty of water. Disposable containers were disposed of in the 'Biological waste bin' while reusable containers were washed up for reuse. Bacterial culture, on the other hand, was collected in a 500 mL Duran bottle. When the bottle is 75% full, it was autoclaved in an on-site facility. Contaminated tissue culture plates and flasks were disinfected with 3% Virkon solution for at least two hours before flushing the excess liquid to drain and disposing them in the 'Biological waste bin'. All used pipette tips were placed in either 'Used pipette tips' jar for sterilisation or 'Sharps bin' with orange-coloured lid for incineration. Used gloves were placed in 'Biological waste Bin'.

6.2.2 Regularisation methods in image reconstruction for micro-bioimpedance tomography

Three regularisation methods - Tikhonov, Gaussian-Laplace and L_1 - for the image reconstruction of 700 µm diameter test samples are verified using 500 µm × 250 µm rectangular Pt electrodes. The performance of these regularisation methods are compared based on the reconstructed images.

Calibration data was obtained from a homogeneous background (250 µL of PBS of concentration 1X), and followed by a test sample with higher or lower conductivity. Figure 6.12 shows the positions of the two test samples in relation to the microelectrodes.

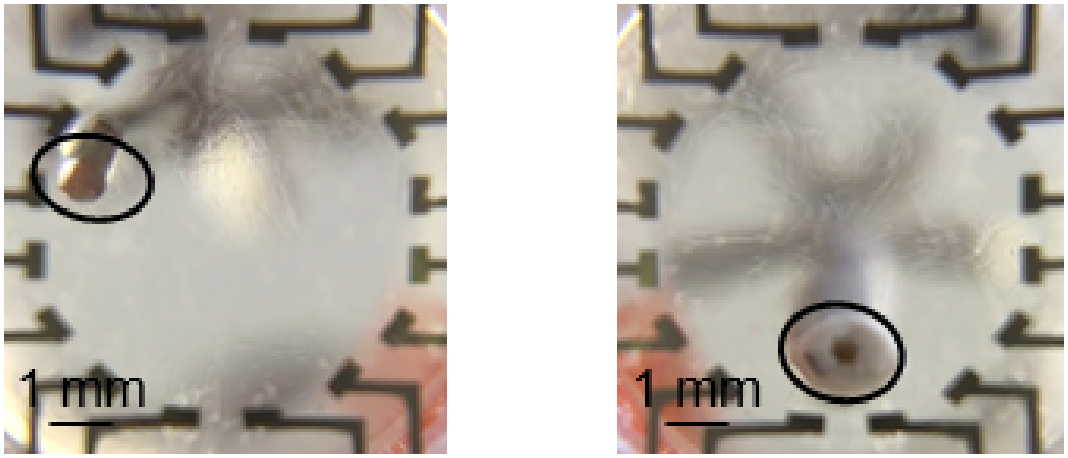

Figure 6.12: (Left) Higher conductivity (Cu metal) and (right) Lower conductivity (rubber) test samples. The positions of the test samples are indicated with black rings

Figure 6.13 presents three recorded data sets for Phosphate-Buffered Saline (PBS) and two test samples with different conductivity values. The voltage difference range between 1 mV and 6 mV, and these graphs do not show large differences between each experiment. The patterns are regular in relation to the electrodes. If the setup is homogeneous, we should observe a regular pattern over 104 measurements. Therefore, the dissimilarities and irregular peaks observed in figure 6.13 are believed to be caused by the placement of the fluidic chamber and possible differences between the electrodes.

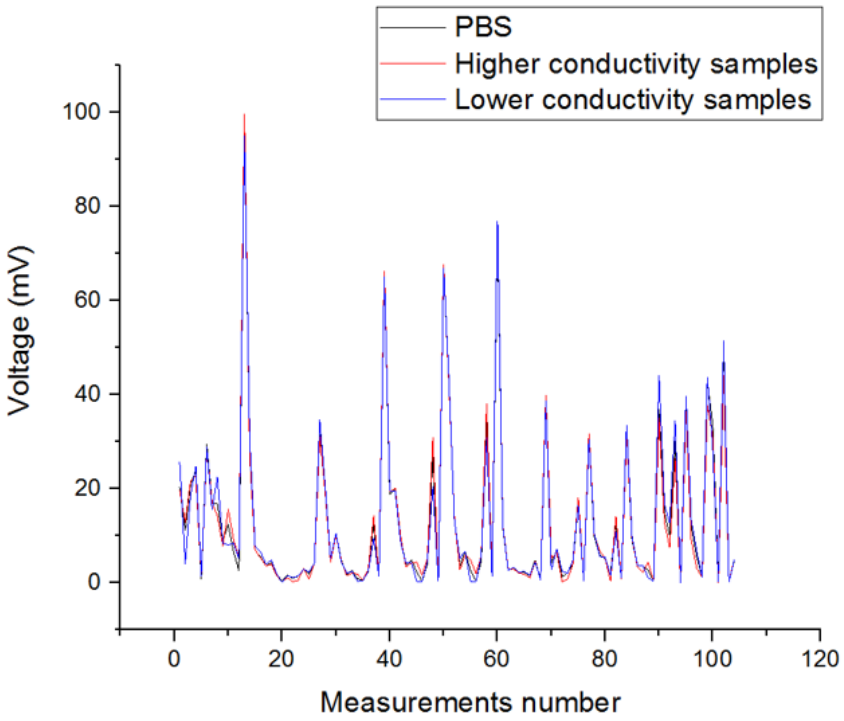

Figure 6.13: (Black) Calibration data of PBS, (red) measurement data with higher conductivity test samples, and (blue) lower conductivity test samples

Conductivity distribution is then estimated according to the potential variation obtained, and from the information gathered, image processing of the test sample can be implemented. Calculations are performed based on the voltage difference values acquired and images are then reconstructed according to the three regularisation methods as shown in figure 6.14.

Test sample	Tikhonov Regularisation	Gaussian-Laplace Regularisation	L_1 Regularisation
Lower resistivity (Higher conductivity)	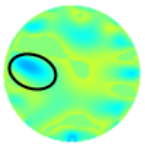	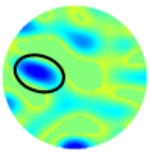	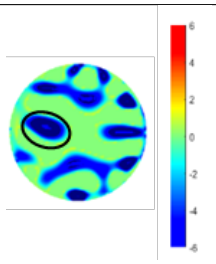
Higher resistivity (Lower conductivity)		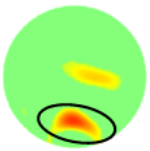	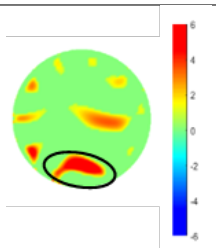

Figure 6.14: Image reconstructions based on three regularisation methods, Tikhonov Regularisation, Gaussian-Laplace Regularisation and L_1 Regularisation (colour scale in Ωcm)

For a test sample with lower resistivity (higher conductivity), Tikhonov regularisation is unable to produce a high intensity image. Gaussian-Laplace regularisation gives the closest representation of the experiment setup although the intensity is not as high as L_1 regularisation. Although the reconstructed image is very strong using L_1 regularisation, errors also appear to be obvious. Ideally the background should not show significant variation in the resistivity. However, the imperfect resistance is caused by the manufacturing process of Au micro-scale electrodes. Similar for a lower conductivity test sample, the best image reconstructed is produced by Gaussian-Laplace regularisation, despite having lower intensity as compared to L_1 regularisation as unwanted errors can be seen clearly in the image reconstructed using this technique.

6.2.3 EIT measurements on MCF7 spheroids using Au micro-scale electrodes on glass substrate

In figure 6.15, the MCF7 spheroid shows a higher resistance compared to the reference solution of MCF7 complete growth medium. The intensity changes are dependent on the conductivity of the MCF7 spheroid and complete growth medium. The green areas represent the conductivity of the media, a baseline measurement taken before the MCF7 spheroid is introduced. The scale is based on the visual spectrum with blue-violet colours representing a higher resistivity than the media and yellow-red colours indicating lower resistivity.

The quality of a reconstructed image from the EIT system can be defined by comparing the reconstructed image with an actual experimental setup. The percentage error was 2.67% where the comparison was performed on the reconstructed image against the actual test setup. The length of MCF7 spheroid can be determined from the size of the chamber, which was 0.71 mm. In the reconstructed image, this value of resistivity represents the outline of the MCF7 spheroid image and the value is -0.15 Ω m, where the minus sign denotes that it is conductive, from the resistivity colour scale.

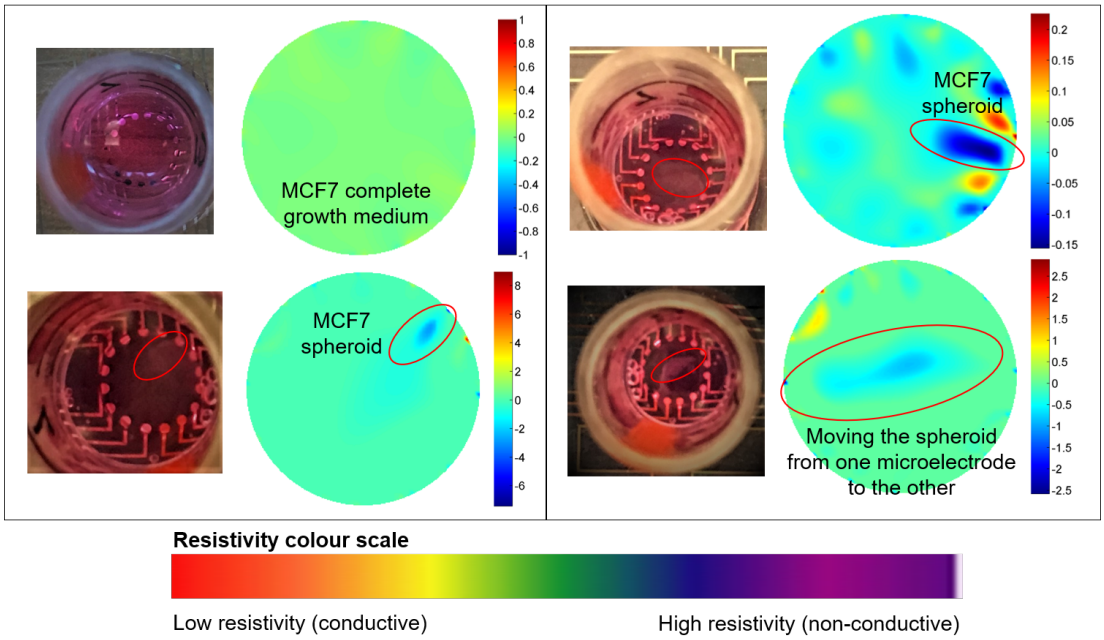

Figure 6.15: EIT imaging of MCF7 spheroids using micro-scale electrode arrays on a glass substrate

With regards to the drug effect experiment on MCF7 spheroids, a Triton-X (surfactant) solution was prepared by diluting 0.5% of Triton-X in complete standard MCF7 growth media. 0.3 ml Triton-X solution was mixed in the chamber filled with a 0.71 mm MCF7 spheroid.

Figure 6.16 shows the effect of Triton-X on the MCF7 spheroid which size was 0.71 mm in diameter. After 1 hour 25 minutes, the spheroid was observed to be in the same condition as the reference understanding that the cell is dead.

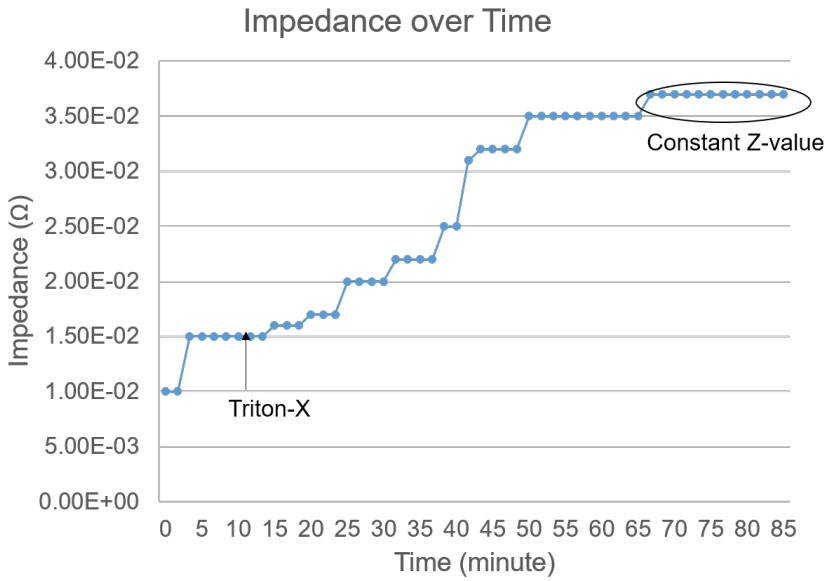

Figure 6.16: Triton-X effect on 0.71 mm MCF7 spheroid

6.2.4 Analysis method

The reconstructed images of MCF7 permeabilisation through the usage of Triton-X is shown in figure 6.17 and shows cell permeabilisation every 5 minutes where t in the figure denotes time in minutes. Triton-X was introduced at $t = 10$ minutes and the impedance magnitude, Z, measured in $\boldsymbol{\omega}$ is increasing over time.

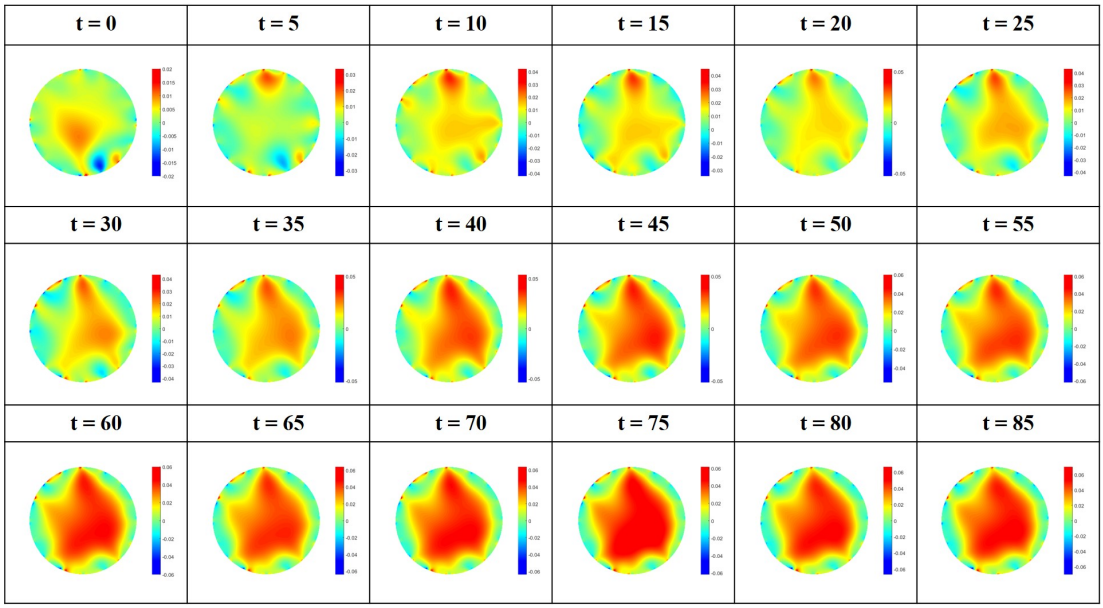

Figure 6.17: Reconstructed images of Triton-X effect on 0.71 mm MCF7 spheroid over 85 minutes

At $t = 10$ minutes when Triton-X was introduced to the MCF7 spheroid, its conductivity started to decrease. The impedance, Z, is observed to be at the highest at $t = 45$ minutes and did not vary much until the end of the experiment, after 85 minutes. The change in conductivity shows the MCF7 spheroid death over time when Triton-X was introduced in the fluid chamber.

6.2.5 EIT measurements on MCF7 spheroids using Flex-MEA

The cell culturing protocol described in 6.2.1.1 was repeated to grow 5.0×10^6 MCF7 cells into cell spheroids. The cells were dispensed in the 96-well spheroid microplate. Figure 6.18 illustrates the placement of Flex-MEA in the well of MCF7 spheroid and 3D microbial cultures. The Flex-MEA is then connected to the EIT system. There is a connection between the EIT system and the computer monitor that displays the reconstructed images.

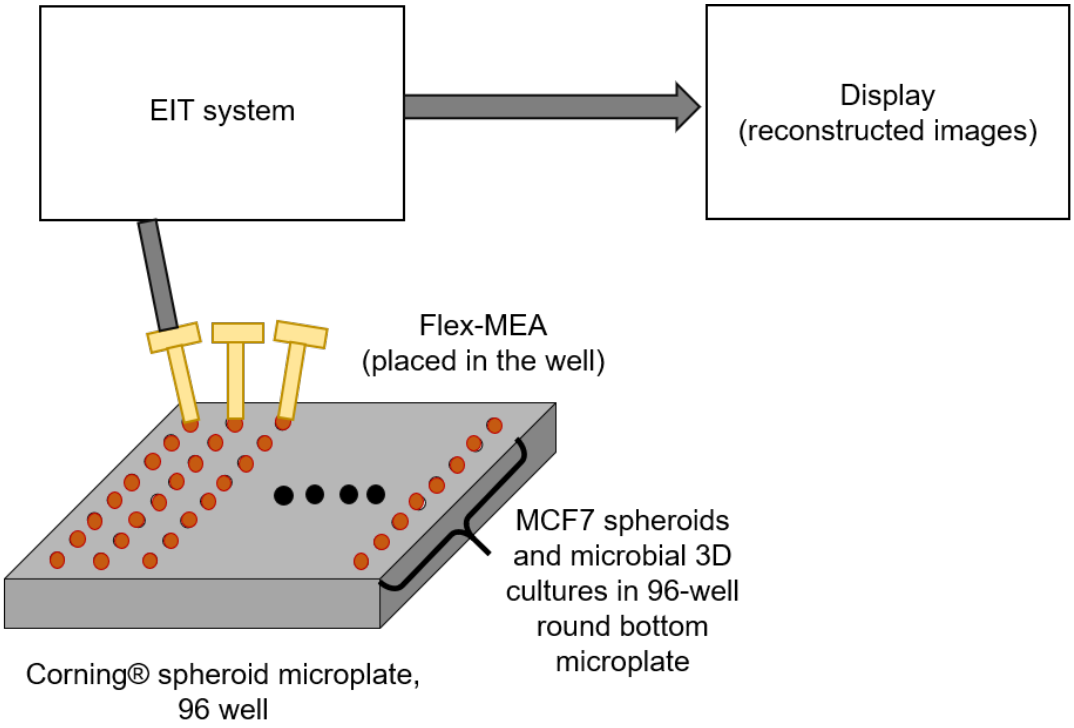

Figure 6.18: Complete experimental setup representing the Flex-MEA, EIT system, display of the reconstructed images and 96-well spheroid microplate

The changes in the MCF7 spheroids were measured over five frequencies; 10 kHz, 30 kHz, 50 kHz, and 70 kHz. The minimal voltage obtained between measurement number 27 and 38, which was below 10 mV for all frequencies, was due to the poor connection in the experimental set-up. From the graph in figure 6.19, it was shown that there is no significant variation against frequency. At high frequency, the induced electric field in the culture medium in the fluid chamber rise and a strong field was present in the MCF7 cell membrane resulting a high potential at higher frequency.

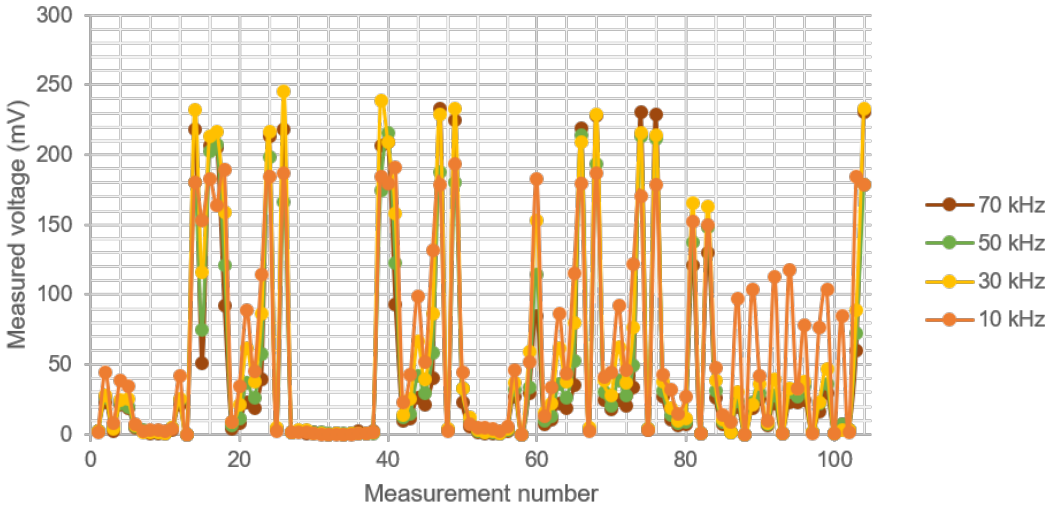

Figure 6.19: Measured voltage across Flex-MEA micro-scale electrodes on MCF7 cell spheroids over five different frequencies – 10 kHz, 30 kHz, 50 kHz, and 70 kHz

The following part of the measurement was introducing three different concentrations 10%, 50%, and 100% of dimethyl sulfoxide (DMSO), a solvent with anti-cancer properties which target the cancer cells [156]. The measurement was performed at 10 kHz. Despite the poor connection in the experimental set-up, that was causing the low measured voltage, figure 6.20 shows a low concentration of DMSO i.e. 10% resulted in higher measured voltage (higher resistivity) and relatively similar as the reference (MCF7 cell spheroid without DMSO). High DMSO concentration resulted in lower measured voltage (low resistivity) which also means introducing concentrated DMSO to the cell spheroid encourages cell death.

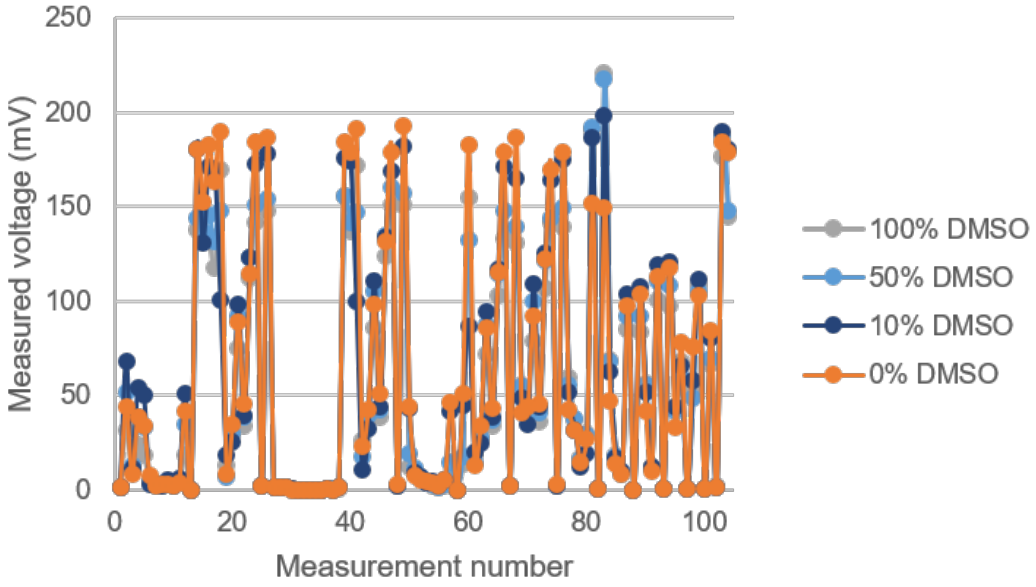

Figure 6.20: Measured voltage across PCB micro-scale electrodes on MCF7 cell spheroids with different DMSO concentrations; 10%, 50%, and 100%. The measurement was performed at 10 kHz

Cell death happens in the centre of the spheroid, the quiescent zone. Since the multi-frequency EIT measurements demonstrate the changes in the cell spheroid, the technique is potentially good and worthwhile to be applied in cell monitoring.

6.3 Micro-bioimpedance tomography on 3D microbial cultures (*Rhodococcus erythropolis*) using Flex-MEA

The Flex-MEA was used to perform the imaging technique for real-time monitoring of bacterial cells. The imaging of bacterial cells can be time-consuming and costly where the conventional methods (fluorescence microscopy, electron microscopy and atomic force microscopy) have bulky equipment.

The food industry is dependent on clean water and soil. The contamination of food

and grain poses a severe economic and health problem for citizens throughout the world. *R. erythropolis*, a type of bacteria which inhabits the soil can be hazardous to both the farm animals and people who eat them. *R. erythropolis* were treated as an exemplar biological system to investigate the application of EIT on microbial cultures using the Flex-MEA to prove the Flex-MEA technology can be implemented on microbial cultures.

R. erythropolis were cultured in Lysogeny Broth (LB) used for bacteria growth, in a 250 ml Erlenmeyer flask. The cells were harvested after 72 hours of growth at 30°C in an innova42 incubator shaker. The incubator agitates the flask, making the nutrients in broth culture homogeneous for bacteria growth.

There are four phases in bacteria growth which are lag, exponential (log), stationary, and death [157]. The lag phase is the start where bacterial cells are metabolically active but not growing. The exponential or log phase is the time where exponential growth of the bacterial cells happens. When the bacterial cells reach a plateu, where the number of dying cells are the same as the number of dividing cells, the bacterial cells are known to be in the stationary phase. The cells are in the death phase when there is an exponential decrease in the number of living bacterial cells. The phases involved in the bacterial cells growth is shown in figure 6.21.

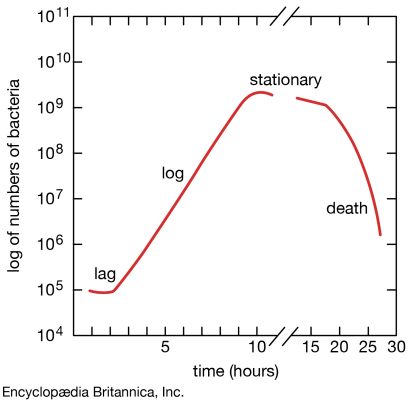

Figure 6.21: The four phases involved in bacteria growth [11]

The cells were left for three days allowing cell immobilisation to be performed when the cells were in the exponential phase. Typically, bacterial cells can be cultured in about one day, but *R. erythropolis* has a slow growth rate and they reached the exponential phase after 3 days. Figures 6.22 and 6.23 were taken from the Biolab at The University of Edinburgh on day 0 and day 3 respectively, of the microbial culture.

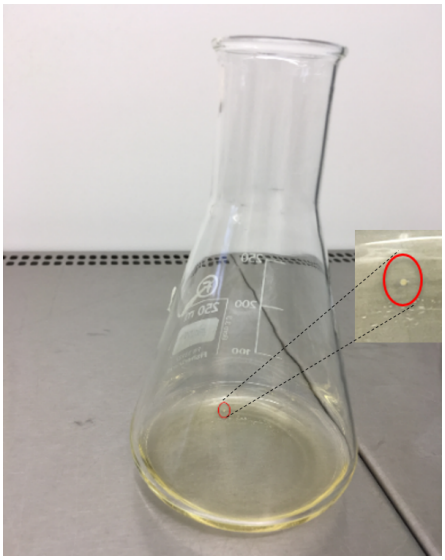

Figure 6.22: *R. erythropolis* culture on day 0 where in the inset is a colony of *R. erythropolis*

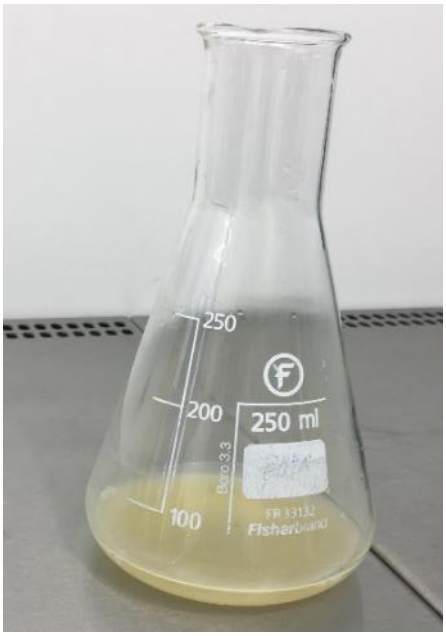

Figure 6.23: *R. erythropolis* culture on day 3

6.3.1 *R. erythropolis* cell immobilisation

LB broth culture and 3% concentration of agarose (LB3A) was prepared and the cells entrapped within LB3A. The cell concentrations were varied for the EIT measurement, and unfilled LB3A gel acts as the control sample. Bacterial cells are known to have a higher growth rate at higher temperatures. The optimum growth rate for *R. erythropolis* is 37°C [158]. Hence, a group of samples were kept in an incubator, and another group of samples were left in the refrigerator which had allowed the study and observation of any significant difference in the EIT measurements. The cells in the incubator are in the "normal" conditions while in the refrigerator they will grow at a slower rate or not at all.

6.3.2 EIT measurement on *R. erythropolis*

Figure 6.24 illustrates the experimental set-up of EIT measurement on *R. erythropolis*.

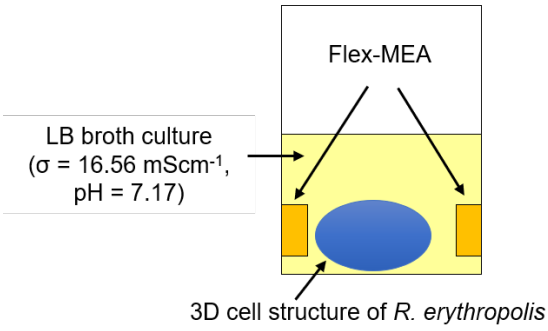

Figure 6.24: The experimental set-up for EIT measurement on *R. erythropolis*

With the Flex-MEA, LB broth culture was first measured as the reference data. Since the fluid chamber was downsized to a 96-well spheroid microplate, it resulted in a slight distortion in conductivity which was, most probably, caused by the fluid meniscus

in the chamber. The measurement was performed at room temperature on the bacterial cells. For bacterial cells that are left in the refrigerator and believed to have a low growth rate, a higher concentration of *R. erythropolis* gave much lower resistivity based on the resistivity colour scale as can be seen in figure 6.25.

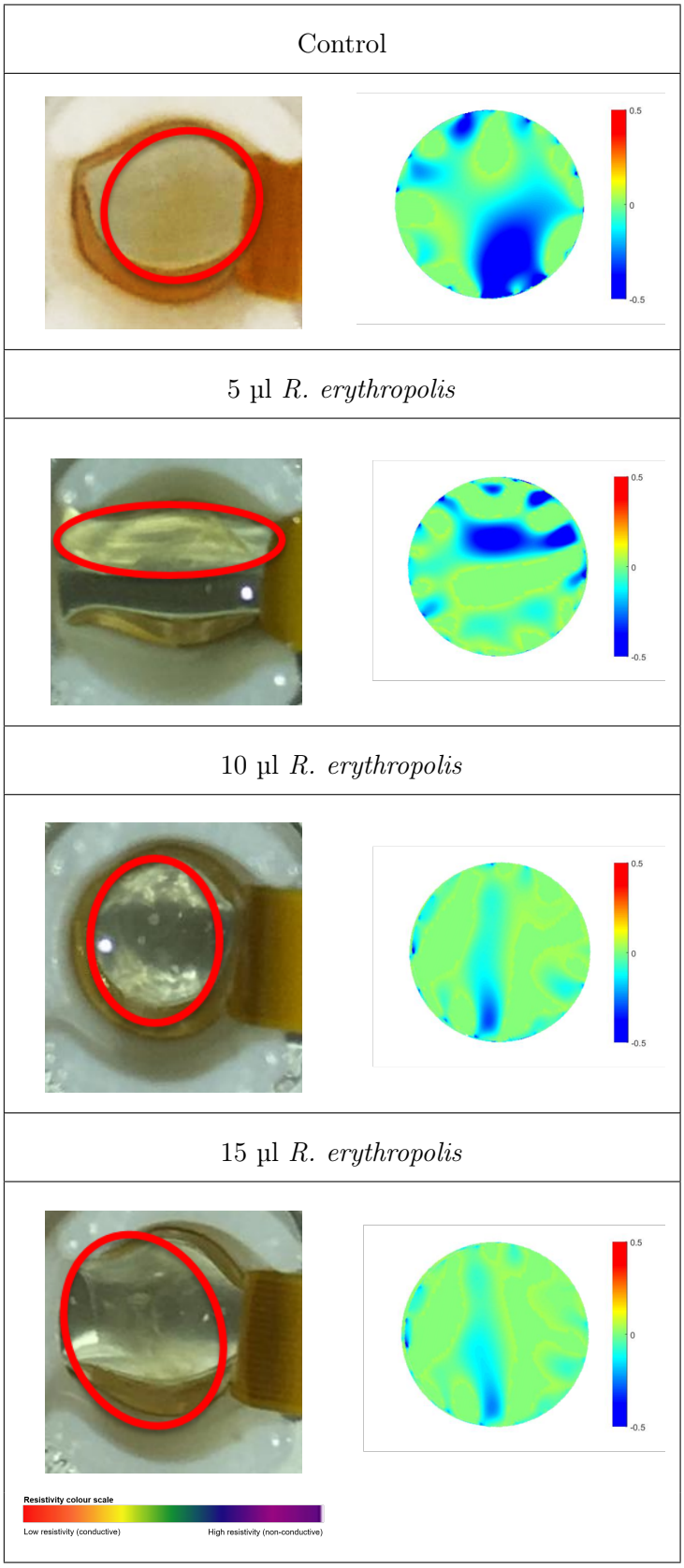

Figure 6.25: Location of *R. erythropolis* in the set-up and reconstructed images at 3°C

These results are similar to samples that were kept in the incubator at 30°C. Higher concentration of *R. erythropolis* gave much lower resistivity as shown in figure 6.26 based on the conductivity distribution of the reconstructed images.

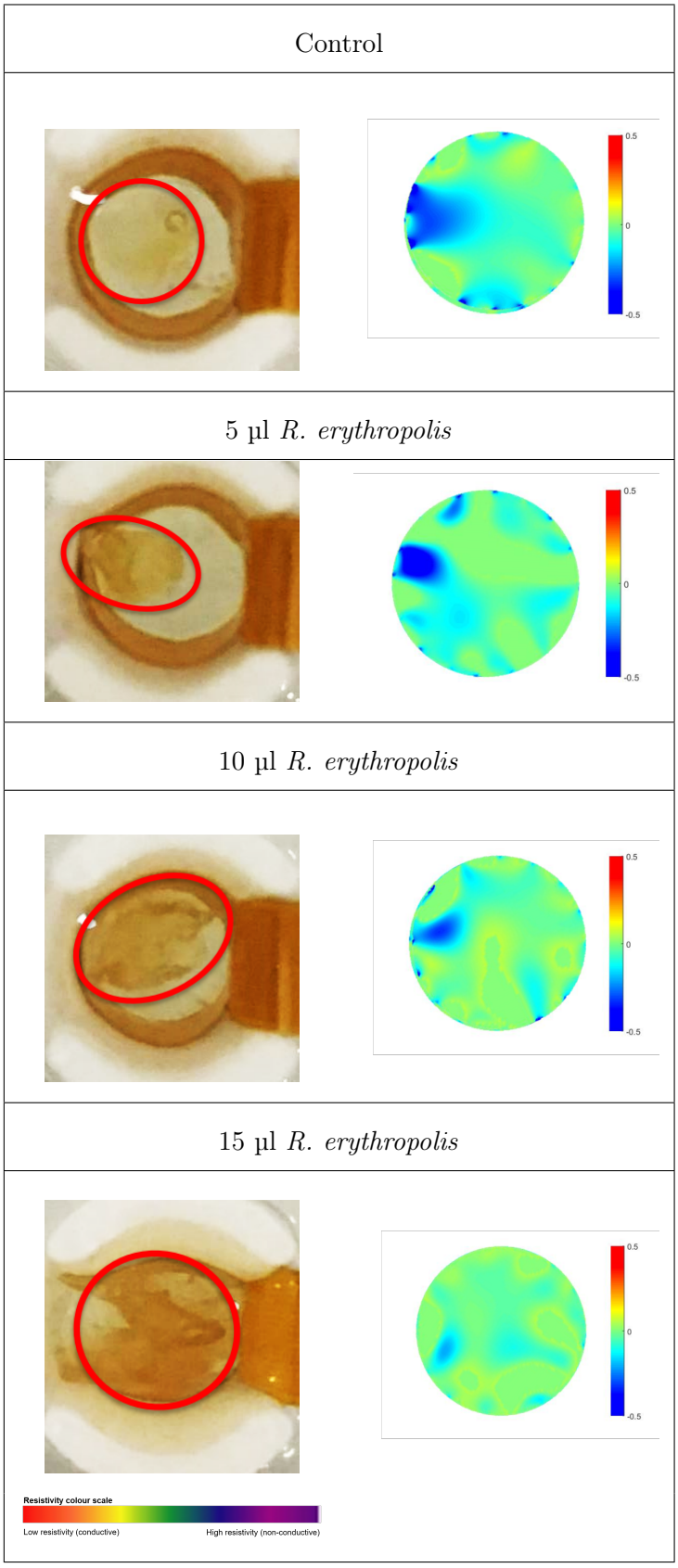

Figure 6.26: Location of *R. erythropolis* in the set-up and reconstructed images at 30°C

Successful detection of *R. erythropolis* has excellent potential not only in the oil industry but also in the pharmaceutical field, particularly in research on vaccine technology to prevent *R. erythropolis* infection in humans.

6.4 Summary

EIT measurements were performed on MCF7 spheroids with cell concentration: 2.4×10^5 cells ml^{-1} and spheroid size: 0.71 mm. Since the fluid chamber is small, the liquid level is not flat, and when the MCF7 spheroid was released into the sensor, fresh culture medium will also be added, hence changing the liquid volume as well as the liquid level. These may cause severe image deformation especially when the cell spheroid is too small.

The image reconstruction algorithm used in the experiment is Tikhonov regularisation [119] as this method produced less unwanted errors as presentedn in 6.2.2. When moving from larger electrodes (on PCB) to micro-scale electrodes (Flex-MEA), it is challenging to achieve high-resolution images in image reconstruction. However, this work has proven that the EIT system is capable of reconstructing the images of MCF7 spheroids placed on the micro-scale electrodes through electrical conductivity distribution.

There are challenges in EIT to reconstruct MCF7 spheroid images from a large scale to smaller scale. In improving the reconstructed images, a more efficient iterative algorithm will be implemented. Future work is to monitor the drug effect on MCF7 spheroids in real-time via EIT imaging.

From the results attained by incorporating Flex-MEA with EIT on microbial

cultures, we are able to say that EIT is the best fit as a portable, non-invasive technique to image the growth of microbial cultures, *R. erythropolis*. Unfilled and filled LB3A gels are more conductive than LB broth culture. Successful measurement of bacterial cell growth and proliferation has excellent potential, in the biomedical field and bioprocessing technology.

Chapter 7

Conclusions and outlook

7.1 Conclusions

Micro-bioimpedance tomography of micro-scale 3D cell cultures and its application in the disease model to replace the use of animal in an experiment is under-explored in the research literature review in chapters 2 and 3. Hence, this research proposed a technique that can be implemented in drug development and eliminating animal testing.

Prior to designing and producing the electrodes for micro-bioimpedance tomography, FEM was performed to evaluate the optimum electrode layout and results presented in chapter 4. A series of EIT devices were designed and presented in chapter 5, from millimetre-scale to micrometre-scale electrode arrays, to determine an optimal electrode arrangement for micro-bioimpedance tomography. Several approaches had been investigated to incorporate the multielectrode arrays with micro-bioimpedance tomography, including, i) varying the morphology of the electrode arrays, ii) comparing the regularisation methods for image reconstruction, and iii) measurements of cell spheroids and

3D microbial structures. The micro-scale electrode arrays were designed with biocompatible outward-facing materials to avoid any physiological changes to the micro-scale cell and microbial cultures during measurements.

The first micro-scale electrodes were fabricated on a PCB (millimetre-scale) and they were NiAu electrodes. The second electrode design was scaled down to micro-scale electrodes to accommodate the micro-bioimpedance tomography of micro-scale 3D cell cultures. These electrodes were manufactured on a glass substrate. The first two designs are representing the planar electrodes. The final micro-scale electrodes design, Flex-MEA, was fabricated on a flexible PCB and represent 3D electrodes.

In a time-dependent analysis, the frequency was set at 10 kHz, 1.5 mA sinusoidal currents applied on two adjacent electrodes with 180° phase difference, at which the cells would respond steadily. When current was sourced through a pair of electrodes, an electric field was distributed with a well of a culture plate. The reconstructed EIT images mapped the variation in conductivity in a sample within the well.

Another factor faced by this research was to produce high-resolution images since the quality of image reconstruction of micro-scale cell, and microbial cultures are weak. In order to solve this situation, the regularisation methods involving Tikhonov, Gaussian-Laplace and L_1 for image reconstruction in micro-scale EIT for biomedical applications had been studied.

For test samples with higher conductivity, the Gaussian-Laplace regularisation was found to give the closest representation of the experimental set-up. However, the intensity derived by Gaussian-Laplace regulation was not as high as L_1 regularisation. Tests, with samples of higher conductivity, were carried out using the L_1 regularisation.

The reconstructed image was found to be more stable. However, errors were still visible. Similarly, for test samples with a lower conductivity, the closest image reconstruction was achieved by Gaussian-Laplace regularisation, despite having a lower intensity as compared to L_1 regularisation. Again, errors were still visible.

These two regularisation methods were seen to produce strong reconstructed images, despite the presence of some errors. However, Tikhonov regularisation seemed to provide the least errors among the three state-of-the-art regularisation methods. Therefore, Tikhonov regularisation was selected as the preferred regularisation method for image reconstruction in this research work. Perturbing issues aroused in this regularisation method, in relation to bio-impedance tomography, were resolved by refining the optimisation algorithm.

Achieving high-resolution images in image reconstruction was found to be very challenging in this study, in particular, when scaling down the arrays from larger electrodes to micro-scale electrodes. Firstly, the image deformation might be caused by culture medium addition when MCF7 spheroid was released into the 6.4 mm diameter chamber, as presented in chapter 6. Secondly, the electrode sensing area was minimal, resulting in a lower voltage differential. Lower voltage differential was possibly due to the lower resistance (R) associated with micro-scale electrodes. However, the interfacial resistance may be larger if it is dependent on surface area which would affect the sensitivity. These are the possible causes that might affect image deformation and prevent in achieving high-resolution images.

The above situation was overcome by a new micro-scale electrode design. It is the PCB fabricated on a flexible PCB with improved electrode arrangement compared with planar electrodes made on a glass substrate. When the PCB electrodes are positioned

on the chamber wall, an electric field is found to be evenly distributed within the 3D cell structure in the chamber, resulting in improved sensitivity. Multiple laboratory tests had been carried out on MCF7 spheroids and 3D *R. erythropolis* cultures. From the results obtained, the PCB showed more stable voltage measurements and produced high-resolution images compared with the fabricated planar electrodes.

A Flex-MEA technology with improved image reconstruction technique on micro-scale 3D cell cultures was developed. This technology gave high-throughput analysis in basic research of drug discovery allowing researchers to conduct a large number of tests in a short period of time and introducing a time-efficient process in finding new drugs.

7.2 Outlook

The research has proven that the final design of PCB, fabricated on a flexible PCB with improved micro-scale electrode geometry arrangement, was found to be very versatile in analysing cancer cells with high-resolution imaging which can be applied both *in vitro* or *in vivo*. When it is designed and structured with advanced multi-electrode geometric configuration, PCB will have a greater potential for a much wider application. Almost all types of organ cells, stem cells or other specimens, such as tumour cells, drugs, that are electrogenic, can be analysed and characterised readily in vitro. The achievement of the work has further illustrated the continuing trend of merging medical and pharmaceutical disciplines with engineering technology. There are other possible opportunities in applying the PCB, such as, understanding cell degeneration, biology of cancer cells, and identifying the effectiveness of anti-cancer drug in treating cancer.

Other future possibility of PCB application is drug-monitoring as in the pharmaceutical technology application.

By incorporating Flex-MEAs with EIT, we can introduce a new technique comprising organ-on-chip technology, tomographic imaging technique and optimising image reconstruction using machine learning, that would help to reduce the cost of drug development. In expanding the research on a broader scope, it would help to develop new drugs, cancer or disease treatment, vaccines, and save millions of animals from being killed in experimental laboratories for improving the quality of life.

Finally, improving systems in the laboratory and incorporating them into real-world applications is the ultimate driving force for electronics and biomedical advances. Integrating these complementary fields will help to surpass the limitations and dramatically expands the freedom of designing medical devices, extending further to a larger area of applications involving environmental monitoring and corrosion monitoring in oil and gas industry apart from medical applications.

List of publications

Y. Yang, J. Jia, S. Smith, **N. Jamil**, W. Gamal & P.O. Bagnaninchi, "A Miniature Electrical Impedance Tomography Sensor and 3-D Image Reconstruction for Cell Imaging", *IEEE Sensors Journal*, vol. 17, no. 2, pp. 514-523, 2017.

N. Jamil, Y. Yang, M. Cela, L.P. Basanta, E.O. Blair, S. Dimartino, J. Jia & S. Smith, "Flexible microelectrode array (Flex-MEA) design for micro-bioimpedance tomography of microbial cultures", *4th Conference on Impedance-Based Cellular Assays*, Edinburgh, Scotland, June 2018.

N. Jamil, Y. Yang, A. Tsiamis, J. Jiabin, & S. Smith, "Comparison of Regularisation Methods in Image Reconstruction for Micro-Bioimpedance Tomography", *IEEE Sensors*, Glasgow, Scotland, October 2017.

N. Jamil, Y. Yang, A. Tsiamis, J. Jiabin, & S. Smith, "Design and fabrication of different platinum microelectrodes morphologies for electrical impedance tomography in biomedical applications", *5th International Conference on Bio-Sensing Technology*, Riva del Garda, Italy, May 2017.

N. Jamil, S. Smith, Y. Yang, J. Jia, P.O. Bagnaninchi & E. González-Fernández, "Design and fabrication of microelectrodes for electrical impedance tomography of cell spheroids", *IEEE EMBS Conference on Biomedical Engineering and Sciences*, pp. 426-431, Kuala Lumpur, Malaysia, December 2016.

N. Jamil, Y. Yang, J. Jia, A.F. Murray, & S. Smith, "Fabrication of gold-plated electrodes on a printed circuit board (PCB) for electrical impedance tomography (EIT) measurement in fluid environment", *MicroTech 2016 - Sensors, MEMS & Advanced Packaging*, Edinburgh, Scotland, March 2016.

A. Buchoux, **N. Jamil**, A. Tsiamis & S. Smith, "Packaging of Silicon Chip by Selectively Curing a Photosensitive Acrylic Resin with a DLP Projector", *MicroTech 2016 - Sensors, MEMS & Advanced Packaging*, Edinburgh, Scotland, March 2016.

A. Tsiamis, Y. Li, **N. Jamil**, S. Smith, H.M. Reekie, J. Terry, A.J. Walton & A.F. Murray, "On-Chip Post-Processing Fabrication Techniques for Extended Gate ISFET pH Sensors", *4th International Conference on Bio-Sensing Technology*, Lisbon, Portugal, May 2015.

Bibliography

[1] "What Is a Cell?." https://www.yourgenome.org/facts/what-is-a-cell. Accessed: 2018-5-11.

[2] G. Cooper, *The Cell: A Molecular Approach.* Sunderland (MA): Sinauer Associates, 2000.

[3] PHRMA, "Biopharmaceutical Research & Development : The Process Behind New Medicines," 2015.

[4] "T25 Flask Sigma Aldrich." http://www.sigmaaldrich.com. Accessed: 2016-12-18.

[5] "Electrical impedance tomography." http://psychology.wikia.com/wiki/Electrical_impedance_tomography. Accessed: 2015-09-18.

[6] "Electrical impedance tomography." https://en.wikipedia.org/wiki/Electrical_impedance_tomography#cite_note-Holder-8. Accessed: 2018-1-1.

[7] A. Adler and A. Boyle, "Electrical Impedance Tomography : Tissue Properties to Image Measures."

[8] A. S. Pandya, A. Arimoto, A. Agarwal & Y. Kinouchi, "A Novel Approach for Measuring Electrical Impedance Tomography for Local Tissue with Artificial Intelligent Algorithm," *International Journal of Biometrics and Bioinformatics*, vol. 3, no. 5, pp. 66–81, 2009.

[9] A. J McKane, T. Biancalani, and T. Rogers, "Stochastic pattern formation and spontaneous polarisation: The linear noise approximation and beyond," *Bulletin of mathematical biology*, vol. 76, 03 2013.

[10] Y. Mamatjan, D. Gürsoy, and A. Adler, "Electrode positions and current patterns for 3D EIT," *12th International Conference in Electrical Impedance Tomography*, 2011.

[11] "Growth of bacterial populations." https://www.britannica.com/science/bacteria/Growth-of-bacterial-populations. Accessed: 2018-7-11.

[12] J. Ferlay, I. Soerjomataram, R. Dikshit, S. Eser, C. Mathers, M. Rebelo, D. M. Parkin, D. Forman, and F. Bray, "Cancer incidence and mortality worldwide: Sources, methods and major patterns in GLOBOCAN 2012," *International Journal of Cancer*, vol. 136, no. 5, pp. E359–E386, 2015.

[13] C. K. Anders and L. a. Carey, "Biology, Metastatic Patterns and Treatment of Patients with Triple-Negative Breast Cancer," *Breast*, vol. 9, no. Suppl 2, pp. S73–S81, 2010.

[14] M. Arora, "Cell Culture Media: A Review," *Mater Methods*, no. 3, p. 175, 2013.

[15] "Studying Cells." https://courses.lumenlearning.com/boundless-biology/chapter/studying-cells/. Accessed: 2015-09-18.

[16] "Cell Biology." https://www.nature.com/scitable/topic/cell-biology-13906536. Accessed: 2017-09-18.

[17] C. Boshoff, "Understanding cancer," *Nature*, vol. 444, no. 7119, pp. 549–549, 2006.

[18] "What is a cell?." https://ghr.nlm.nih.gov/primer/basics/cell. Accessed: 2018-5-11.

[19] "What Is a Cell?." https://www.nature.com/scitable/topicpage/what-is-a-cell-14023083. Accessed: 2018-5-11.

[20] W. Liu, Y. Deng, Y. Liu, W. Gong, and W. Deng, "Stem cell models for drug discovery and toxicology studies," *Journal of Biochemical and Molecular Toxicology*, vol. 27, no. 1, pp. 17–27, 2013.

[21] A.-A. D. Lakraj, B. Jabbari, and D. G. Machado, "Chapter 25 - neuronal networks and therapeutics in neurodegenerative disorders," in *Neuronal Networks in Brain Function, CNS Disorders, and Therapeutics* (C. L. Faingold and H. Blumenfeld, eds.), pp. 335 – 348, San Diego: Academic Press, 2014.

[22] A. N. Orekhov and E. A. Ivanova, "Chapter 5 - antiatherosclerotic efficacy of nutraceuticals," in *Nutraceuticals* (R. C. Gupta, ed.), pp. 61 – 73, Boston: Academic Press, 2016.

[23] S. Srivastava, S. Mishra, J. Dewangan, A. Divakar, P. K. Pandey, and S. K. Rath, "Chapter 2 - principles for in vitro toxicology," in *In Vitro Toxicology* (A. Dhawan and S. Kwon, eds.), pp. 21 – 43, Academic Press, 2018.

[24] J. Hardy, "Julius Petri and his Petri Plate Invention - History of the Petri Dish," 1880.

[25] S. R. Caliari and J. A. Burdick, "A practical guide to hydrogels for cell culture," *Nature Methods*, vol. 13, no. 5, pp. 405–414, 2016.

[26] A. Abbott, "Biology's new dimension," *Nature*, vol. 424, no. August, pp. 870–872, 2003.

[27] B. L. Duell, A. W. Cripps, M. A. Schembri, and G. C. Ulett, "Epithelial cell coculture models for studying infectious diseases: Benefits and limitations," *Journal of Biomedicine and Biotechnology*, vol. 2011, 2011.

[28] M. Bhattacharya, M. M. Malinen, P. Lauren, Y. R. Lou, S. W. Kuisma, L. Kanninen, M. Lille, A. Corlu, C. Guguen-Guillouzo, O. Ikkala, A. Laukkanen, A. Urtti, and M. Yliperttula, "Nanofibrillar cellulose hydrogel promotes three-dimensional liver cell culture," *Journal of Controlled Release*, vol. 164, no. 3, pp. 291–298, 2012.

[29] G. R. Souza, J. R. Molina, R. M. Raphael, M. G. Ozawa, D. J. Stark, C. S. Levin, L. F. Bronk, J. S. Ananta, J. Mandelin, M.-M. Georgescu, J. A. Bankson, J. G. Gelovani, T. C. Killian, W. Arap, and R. Pasqualini, "Three-dimensional tissue culture based on magnetic cell levitation," *Nat Nanotechnol.*, vol. 5, no. 4, pp. 291–296, 2010.

[30] A. Y. Hsiaoa, Y.-C. Tung, X. Qu, L. R. Patel, K. J. Pienta, and S. Takayama, "384 Hanging drop arrays give excellent Z-factors and allow versatile formation of co-culture spheroids," *Biotechnol Bioeng.*, vol. 109, no. 5, pp. 1293–1304, 2012.

[31] E. M. Ahmed, "Hydrogel: Preparation, characterization, and applications: A review," *Journal of Advanced Research*, vol. 6, no. 2, pp. 105 – 121, 2015.

[32] B. L. Roach, A. B. Nover, G. A. Ateshian, and C. T. Hung, *Agarose Hydrogel Characterization for Regenerative Medicine Applications: Focus on Engineering Cartilage*, ch. 16, pp. 258–273. John Wiley & Sons, Ltd, 2016.

[33] W. L. Haisler, D. M. Timm, J. A. Gage, H. Tseng, T. C. Killian, and G. R. Souza, "Three-dimensional cell culturing by magnetic levitation," *Nature Protocols*, vol. 8, no. 10, pp. 1940–1949, 2013.

[34] J. A. Zimmermann and T. C. Mcdevitt, "Pre-conditioning mesenchymal stromal cell spheroids for immunomodulatory paracrine factor secretion," *Cytotherapy*, vol. 16, no. 3, pp. 331–345, 2014.

[35] "Cell division and cancer." https://www.nature.com/scitable/topicpage/cell-division-and-cancer-14046590. Accessed: 2018-5-11.

[36] "What Is Cancer?." https://www.cancer.org/cancer/cancer-basics/what-is-cancer.html. Accessed: 2017-11-14.

[37] "Disease model." http://www.nature.com/subjects/disease-model. Accessed: 2017-06-01.

[38] J. L. Sterneckert, P. Reinhardt, and H. R. Schöler, "Investigating human disease using stem cell models," *Nature Reviews Genetics*, vol. 15, no. 9, pp. 625–639, 2014.

[39] M. J. Prescott, "The Three Rs," *The International Encyclopedia of Primatology*, pp. 1–5, 2017.

[40] M. L. Graham and M. J. Prescott, "The multifactorial role of the 3Rs in shifting the harm-benefit analysis in animal models of disease," *European Journal of Pharmacology*, vol. 759, pp. 19–29, 2015.

[41] "The 3Rs." https://www.nc3rs.org.uk/the-3rs#The\%203Rs\%20definitions. Accessed: 2019-5-1.

[42] "Drug discovery and development." https://www.nature.com/subjects/drug-discovery-and-development. Accessed: 2017-09-18.

[43] Pharmaceutical Research and Manufacturers of America, "Drug Discovery and Development, Drug Discovery," tech. rep., Pharmaceutical Research and Manufacturers of America, 2006.

[44] D. L. Holliday and V. Speirs, "Choosing the right cell line for breast cancer research," *Breast Cancer Research*, vol. 13, no. 215, pp. 1–7, 2011.

[45] B. Alberts, A. Johnson, J. Lewis, M. Raff, K. Roberts, and P. Walter, "Molecular Biology of the Cell. 4th edition," 2002.

[46] H. Page, P. Flood, and E. G. Reynaud, "Three-dimensional tissue cultures: Current trends and beyond," *Cell and Tissue Research*, vol. 352, no. 1, pp. 123–131, 2013.

[47] S. A. Langhans, "Three-dimensional in vitro cell culture models in drug discovery and drug repositioning," *Frontiers in Pharmacology*, vol. 9, p. 6, 2018.

[48] T.-m. Achilli, J. Meyer, and J. R. Morgan, "Advances in the formation, use and understanding of multi- cellular spheroids," *Expert Opin Biol Ther*, vol. 12, no. 10, pp. 1347–1360, 2012.

[49] D. Rogozhnikov, P. J. O'Brien, S. Elahipanah, and M. N. Yousaf, "Scaffold Free Bio-orthogonal Assembly of 3-Dimensional Cardiac Tissue via Cell Surface Engineering," *Scientific Reports*, vol. 6, no. 1, p. 39806, 2016.

[50] M. Bissell, "Mina Bissell," *Nature Medicine*, vol. 11, no. 3, p. 242, 2005.

[51] "Spheroids And 3d Cell Culture: A Brief History." https://www.thermofisher.com/blog/cellculture/a-brief-history-of-spheroids-and-3. Accessed: 2018-01-29.

[52] C. Neeley, "A Brief History of Spheroids," 2016.

[53] C. Neeley, "The use of spheroids in cancer research," 2015.

[54] R. Allison, "Spheroid Cultures for Cancer Research and Treatment," 1990.

[55] "Catabolism." http://goldbook.iupac.org/html/C/C00870.html. Accessed: 2018-5-11.

[56] S. Bhat and A. Kumar, "Biomaterials and bioengineering tomorrow's healthcare," *Biomatter*, vol. 3, no. 3, 2013.

[57] C. Grüber and R. A. Wood, *Role of Vaccines*. Elsevier Inc., 2015.

[58] Kutzler Michele A. and D. B. Weiner, "DNA vaccines: ready for prime time?," *Nat Rev Genet. 2008*, vol. 9, no. 10, pp. 776–788, 2008.

[59] W. W. Leitner, H. Ying, and N. P. Restifo, "DNA and RNA-based vaccines: principles, progress and prospects," *Vaccine*, vol. 18, no. 9-10, pp. 765–777, 1999.

[60] "How vaccines are tested, licensed and monitored." http://vk.ovg.ox.ac.uk/vaccine-development. Accessed: 2018-5-11.

[61] J. Melorose, R. Perroy, and S. Careas, "Study Guide - Biotechnology and Cell Culture," *Study Guide - Biotechnology and Cell Culture*, vol. 1, p. 2604, 2015.

[62] M. C. Phelan, "Basic techniques in mammalian cell tissue culture," *Curr Protoc Cell Biol*, vol. Chapter 1, p. Unit 1 1, 2007.

[63] "Cell Types & Culture Characteristics." https://www.sigmaaldrich.com/technical-documents/protocols/biology/cell-types-culture.html. Accessed: 2018-5-11.

[64] Cellgro, "Dissociation of Cell Monolayers Using Trypsin Solutions," *Corning Incorporated Press*, p. 1, 2012.

[65] J. V. May and D. W. Schomberg, "The effect of plating density on granulosa cell growth and differentiation in vitro.," *Molecular and cellular endocrinology*, vol. 34, no. 3, pp. 201–213, 1984.

[66] C. D. Donaldson and K. N. Bishop, "Cell culture," *British Journal Of Hospital Medicine (London, England: 2005*, vol. 76, no. 1, 2015.

[67] V. Gupta, M. Sengupta, J. Prakash, and B.-C. Tripathy, *Basic and Applied Aspects of Biotechnology*. Springer International Publishing, 2017.

[68] F. A. Khan, *Biotechnology Fundamentals*. CRC Press LLC, 2017.

[69] A. K.-L. Chen, S. Reuveny, and S. K. W. Oh, "Application of human mesenchymal and pluripotent stem cell microcarrier cultures in cellular therapy: Achievements and future direction," *Biotechnology Advances*, vol. 31, no. 7, pp. 1032–1046, 2013.

[70] Y. Fang and R. M. Eglen, "Three-Dimensional Cell Cultures in Drug Discovery and Development," *SLAS DISCOVERY: Advancing Life Sciences R&D*, p. 247255521769679, 2017.

[71] S. Sanyal, "Culture and Assay Systems Used for 3D Cell Culture," *Corning*, 2014.

[72] B. M. P. H. P. Puttaraju and B. C. K. Murthy, *Molecular biology and biochemistry: A lab manual*. New India Publishing Agency, 2008.

[73] Z. Bartlett, "The Hayflick Limit," 2014.

[74] Invitrogen, "Cell Culture Basics Handbook," *ThermoFisher Scientific Inc.*, pp. 1–61, 2010.

[75] T. Yao and Y. Asayama, "Animal-cell culture media: History, characteristics, and current issues," *Reproductive Medicine and Biology*, vol. 16, no. 2, pp. 99–117, 2017.

[76] PAA, "PA Serum Brochure," 2013.

[77] S. L. Gersen and M. B. Keangle, eds., *The principles of clinical cytogenetics.* Humana Press, 2005.

[78] S. S. Ronald Pethig, ed., *Introductory Bioelectronics: For Engineers and Physical Scientists.* John Wiley and Sons Ltd, 2013.

[79] C. Roth, "Cell Passage and Use of Trypsin," 2009.

[80] N. S. Templeton, ed., *Gene and cell therapy: Therapeutic mechanisms and strategies.* Marcel Dekker, Inc, 2005.

[81] X. Bao and S. Palecek, *Chapter 1 – Genetic Engineering in Stem Cell Biomanufacturing.* Elsevier B.V., 2016.

[82] I. A. Cree, ed., *Cancer Cell Culture - Methods and Protocols.* Springer Science+Business Media, second ed., 2011.

[83] C. K. N., *Basic concept of biotechnology.* Laxmi Book Publication, 2015.

[84] Gibco, "Cell culture basics Now includes transfection," 2014.

[85] R. I. Freshney, *Culture of Animal Cells: A Manual of Basic Technique.* Wiley-Liss, New York, 1994.

[86] C. Skourou, P. J. Hoopes, R. R. Strawbridge, and K. D. Paulsen, "Feasibility studies of electrical impedance spectroscopy for early tumor detection in rats," *Physiological Measurement*, vol. 25, no. 1, p. 335, 2004.

[87] H. P. Schwan, "The practical success of impedance techniques from an historical perspective," 1999.

[88] D. A. Borkholder, *Cell Based Biosensors Using Microelectrodes.* PhD thesis, Stanford University, 1998.

[89] W. J.G., *Electrical Impedance Tomography.* Adam Hilger, Bristol, 1990.

[90] A. F. Kanta and A. Decroly, "Stainless steel electrode characterizations by electrochemical impedance spectroscopy for dye-sensitized solar cells," *Electrochimica Acta*, vol. 56, no. 27, pp. 10276–10282, 2011.

[91] G. Voskerician, M. S. Shive, R. S. Shawgo, H. von Recum, J. M. Anderson, M. J. Cima, and R. Langer, "Biocompatibility and biofouling of mems drug delivery devices," *Biomaterials*, vol. 24, no. 11, pp. 1959 – 1967, 2003.

[92] C. Canali, A. Heiskanen, H. B. Muhammad, P. Høyum, F.-J. Pettersen, M. Hemmingsen, A. Wolff, M. Dufva, Ørjan Grøttem Martinsen, and J. Emnéus, "Bioimpedance monitoring of 3d cell culturing—complementary electrode configurations for enhanced spatial sensitivity," *Biosensors and Bioelectronics*, vol. 63, pp. 72 – 79, 2015.

[93] H. Yin, F. L. Wang*, A. L. Wang, J. Cheng, and P. Y. Zhou, "Bioelectrical impedance assay to monitor changes in aspirin-treated human colon cancer ht-29 cell shape during apoptosis," *Analytical Letters*, vol. 40, no. 1, pp. 85–94, 2007.

[94] P. J. Yang, V. V. Halbach, R. T. Higashida, and G. B. Hieshima, "Platinum wire: a new transvascular embolic agent.," *American Journal of Neuroradiology*, vol. 9, no. 3, pp. 547–550, 1988.

[95] C.-Y. Chen, E. Tamiya, K. Ishihara, Y. Kosugi, Y.-C. Su, N. Nakabayashi, and I. Karube, "A biocompatible needle-type glucose sensor based on platinum-electroplated carbon electrode," *Applied Biochemistry and Biotechnology*, vol. 36, p. 211, Sep 1992.

[96] A. R. Kherlopian, T. Song, Q. Duan, M. A. Neimark, M. J. Po, J. K. Gohagan, and A. F. Laine, "A review of imaging techniques for systems biology.," *BMC systems biology*, vol. 2, p. 74, 2008.

[97] M. Weyland and P. a. Midgley, "Extending energy-filtered transmission electron microscopy (EFTEM) into three dimensions using electron tomography.," *Micros. Microanal.*, vol. 9, pp. 542–555, 2003.

[98] F. Bistolfi, "Alessandro Vallebona," *Fisica in Medicina*, vol. 2, pp. 115 – 123, 2005.

[99] B. Pollak, "Experiences with Planography," *Diseases of the Chest*, vol. 24, no. 6, pp. 663–669, 1953.

[100] J. T. Littleton and M. L. Durizsch Littleton, "Conventional Tomography," 1996.

[101] "The Nobel Prize in Physiology or Medicine 1979." https://www.nobelprize.org/nobel_prizes/medicine/laureates/1979/. Accessed: 2017-06-30.

[102] R. Bayford, I. Roitt, T. Rademacher, A. Demosthenous, and R. Iles, "Detection of cancer with electrical impedance tomography," Sept. 8 2015. US Patent 9,125,583.

[103] S. N. Prasad, D. Houserkova, and J. Campbell, "Breast imaging using 3D electrical impedence tomography.," *Biomedical papers of the Medical Faculty of the University Palack??, Olomouc, Czechoslovakia*, vol. 152, no. 1, pp. 151–154, 2008.

[104] V. Cherepenin, A. Karpov, A. Korjenevsky, V. Kornienko, A. Mazaletskaya, D. Mazourov, and D. Meister, "A 3d electrical impedance tomography (eit) system for breast cancer detection," *Physiological Measurement*, vol. 22, no. 1, p. 9, 2001.

[105] Y. Yang, J. Jia, S. Smith, S. Member, N. Jamil, W. Gamal, and P. Bagnaninchi, "A Miniature Electrical Impedance Tomography Sensor and 3D Image Reconstruction for Cell Imaging," *IEEE Sensors Journal*, vol. 17, no. 2, pp. 514–523, 2017.

[106] T. Sun, S. Tsuda, K.-P. Zauner, and H. Morgan, "On-chip electrical impedance tomography for imaging biological cells," *Biosensors & Bioelectronics*, vol. 25, no. 5, pp. 1109–1115, 2010.

[107] V. Cherepenin, A. Karpov, A. Korjenevsky, and V. Kornienko, "A 3D electrical impedance tomography (EIT) system," *Physiological Measurement*, vol. 22, pp. 9–18, 2001.

[108] A. P. Bagshaw, A. D. Liston, R. H. Bayford, A. Tizzard, A. P. Gibson, A. T. Tidswell, M. K. Sparkes, H. Dehghani, C. D. Binnie, and D. S. Holder, "Electrical impedance tomography of human brain function using reconstruction algorithms based on the finite element method," *NeuroImage*, vol. 20, no. 2, pp. 752–764, 2003.

[109] N. Kerrouche, C. McLeod, and W. Lionheart, "Time series of EIT chest images using singular value decomposition and Fourier transform," *Physiol. Meas.*, vol. 22, no. 1, pp. 147–157, 2001.

[110] M. Soleimani, C. Gómez-Laberge, and A. Adler, "Imaging of conductivity changes and electrode movement in EIT," *Physiological Measurement*, vol. 27, no. 5, 2006.

[111] B. H. Brown and A. D. Seagar, "The Sheffield data collection system," *Clinical Physics and Physiological Measurement*, 1987.

[112] P. Hua, J. G. Webster, and W. J. Tompkins, "A regularised electrical impedance tomography reconstruction algorithm," *Clinical Physics and Physiological Measurement*, pp. 0–5, 1988.

[113] B. Buntz, "Biomaterials and the Future of Medical Devices." https://www.mddionline.com/biomaterials-and-future-medical-devices. Accessed: 2017-06-30.

[114] C. Fillers, "Conductive Plastic / Polymer Additives Conductive Plastic / Polymer Additives."

[115] M. L. Huffman and B. J. Venton, "Carbon-Fiber Microelectrodes for In Vivo Applications," *Analyst*, vol. 134, no. 1, pp. 18–24, 2010.

[116] D. D. Zhou, X. T. Cui, A. Hines, and R. J. Greenberg, *Conducting polymers in neural stimulation applications*. Springer Science+Business Media, 2010.

[117] P. Metherall, D. C. Barber, R. H. Smallwood, and B. H. Brown, "Three-dimensional electrical impedance tomography," *Nature*, vol. 380, pp. 509–512, 1996.

[118] N. Polydorides and W. R. B. Lionheart, "A Matlab toolkit for three-dimensional electrical impedance tomography: a contribution to the Electrical Impedance and Diffuse Optical Reconstruction Software project," *Measurement Science and Technology*, vol. 13, no. 12, pp. 1871–1883, 2002.

[119] M. Vauhkonen, D. Vadász, P. A. Karjalainen, E. Somersalo, and J. P. Kaipio, "Tikhonov regularization and prior information in electrical impedance tomography.," *IEEE transactions on medical imaging*, vol. 17, no. 2, pp. 285–93, 1998.

[120] B. M. Graham and A. Adler, "Electrode placement configurations for 3D EIT," *Physiological measurement*, vol. 28, no. 7, pp. S29–S44, 2007.

[121] Q. Wang and Wang H, "Image Reconstruction Based on L1 Regularization for Electrical Impedance Tomography (EIT)," *Instrumentation and Measurement Technology Conference (I2MTC), 2011 IEEE*, pp. 5–9, 2011.

[122] L. Borcea, "Electrical impedance tomography," *Inverse Problems*, vol. 18, no. 6, pp. R99–R136, 2002.

[123] C. J. Kotre, "A sensitivity coefficient method for the reconstruction of electrical impedance tomograms," *Clinical Physics and Physiological Measurement*, vol. 10, no. 3, pp. 275–281, 1989.

[124] L. Zhang, "Image reconstruction algorithm for electrical impedance tomography using updated sensitivity matrix," *Soft Computing and Pattern Recognition (SoCPaR), 2011 International Conference of*, pp. 248–252, 2011.

[125] E. V. D. Berg and M. P. Friedlander, "Probing the Pareto Frontier for Basis Pursuit Solutions," *Society for Industrial and Applied Mathematics*, vol. 31, no. 2, pp. 890–912, 2008.

[126] "The Finite Element Method (FEM)." https://www.comsol.com/multiphysics/finite-element-method. Accessed: 2017-12-02.

[127] T. D. Shook and R. S. Reddy Gorla, "Finite element analysis and redesign of a compressor hub spinner," *Finite Elements in Analysis and Design*, vol. 28, no. 1, pp. 19–31, 1997.

[128] O. de Weck and I. Y. Kim, "Finite Element Method," *Engineering Design and Rapid Prototyping*, vol. 810, p. 26, 2004.

[129] F. Rattay, S. M. Danner, U. S. Hofstoetter, and K. Minassian, *Finite Element Modeling for Extracellular Stimulation*, pp. 1–12. New York, NY: Springer New York, 2013.

[130] V. B. C. Tan, M. X. Tong, K. M. Lim, and C. T. Lim, "Finite Element Modeling of Electronic Packages Subjected to Drop Impact," *Packaging (Boston, Mass.)*, vol. 28, no. 3, pp. 555–560, 2005.

[131] "Modeling and Simulation." https://www.mathworks.com/discovery/modeling-and-simulation.html. Accessed: 2017-12-02.

[132] R. N. Nanhorngué, F. Pesavento, and B. A. Schrefler, "Sensitivity analysis applied to finite element method model for coupled multiphase system," *International Journal for Numerical and Analytical Methods in Geomechanics*, vol. 37, pp. 2205–2222, 2013.

[133] W. Becker, J. Rowson, J. Oakley, A. Yoxall, G. Manson, and K. Worden, "Bayesian sensitivity analysis of a large nonlinear model," 2008.

[134] A. J. Bard and L. R. Faulkner, *Electrochemical Methods: Fundamentals and Applications*. John Wiley and Sons Inc, Dec. 2001.

[135] R. Shukla, V. Bansal, M. Chaudhary, A. Basu, R. R. Bhonde, and M. Sastry, "Biocompatibility of gold nanoparticles and their endocytotic fate inside the cellular compartment: A microscopic overview," *Langmuir*, vol. 21, no. 23, pp. 10644–10654, 2005. PMID: 16262332.

[136] I. Rose and C. Whittington, *Nickel Plating Handbook*. Nickel Institute, 2014.

[137] P. A. Kohl, "Electrodeposition of Gold," *Modern Electroplating: Fifth Edition*, pp. 115–130, 2011.

[138] J. Meija, T. B. Coplen, M. Berglund, W. A. Brand, P. De Bièvre, M. Gröning, N. E. Holden, J. Irrgeher, R. D. Loss, T. Walczyk, and T. Prohaska, "Atomic weights of the elements 2013 (IUPAC Technical Report)," *Pure and Applied Chemistry*, vol. 88, no. 3, pp. 265–291, 2016.

[139] "Potassium cyanide." https://pubchem.ncbi.nlm.nih.gov/compound/potassium_cyanide. Accessed: 2018-17-11.

[140] J. H. Clark and M. J. Braithwaite, *Applications of Hydrogen Peroxide and Derivatives*. RSC Clean Technology Monographs, The Royal Society of Chemistry, 1999.

[141] "TARGET 3001! PCB Layout CAD." http://ibfriedrich.com/en/index.html. Accessed: 2017-12-12.

[142] T. R. Kucklick, "Assessing Biocompatibility," *The Medical Device R&D Handbook, Second Edition*, pp. 1–27, 2013.

[143] a. Mohr, W. Finger, K. Fohr, W. Nisch, and W. Gopel, "Performance Of A Thin Film Microelectrode Array For Monitoring Electrogenic Cells In Vitro," *Proceedings of the International Solid-State Sensors and Actuators Conference - TRANSDUCERS '95*, vol. 2, pp. 265–269, 1995.

[144] L. Wang, J. Zhu, C. Deng, W.-l. Xing, and J. Cheng, "An automatic and quantitative on-chip cell migration assay using self-assembled monolayers combined with real-time cellular impedance sensing," *Lab on a Chip*, vol. 8, no. 6, p. 872, 2008.

[145] A. R. A. Rahman, C.-M. Lo, and S. Bhansali, "A micro-electrode array biosensor for impedance spectroscopy of human umbilical vein endothelial cells," *Sensors and Actuators B*, vol. 118, no. 1-2, pp. 115–120, 2006.

[146] M. Kuperstein and D. A. Whittington, "A Practical 24 Channel Microelectrode for Neural Recording in Vivo," *IEEE Transactions on Biomedical Engineering*, vol. BME-28, no. 3, pp. 288–293, 1981.

[147] P. Linderholm, T. Braschler, J. Vannod, Y. Barrandon, M. Brouard, and P. Renaud, "Two-dimensional impedance imaging of cell migration and epithelial stratification," *Lab on a Chip*, vol. 6, no. 9, p. 1155, 2006.

[148] W. Gamal, *Real-time bioimpedance measurements of stem cell-based disease models-on-a-chip*. PhD thesis, The University of Edinburgh, 2015.

[149] N. F. Sheppard, R. C. Tucker, and C. Wu, "Electrical conductivity measurements using microfabricated interdigitated electrodes," *Analytical Chemistry*, vol. 65, no. 9, pp. 1199–1202, 1993.

[150] G. C. Mendes, T. R. Brandão, and C. L. Silva, "Ethylene oxide sterilization of medical devices: A review," *American Journal of Infection Control*, vol. 35, no. 9, pp. 574 – 581, 2007.

[151] Y. Yang and J. Jia, "A multi-frequency electrical impedance tomography system for real-time 2D and 3D imaging," *Review of Scientific Instruments*, vol. 88, no. 8, 2017.

[152] A. R. Frangi, P. J. Riu, J. Rosell, and M. A. Viergever, "Propagation of measurement noise through backprojection reconstruction in electrical impedance tomography," *IEEE Transactions on Medical Imaging*, vol. 21, pp. 566–578, June 2002.

[153] "MCF7 (ATCC® HTB-22™)." https://www.lgcstandards-atcc.org/Products/All/HTB-22.aspx?geo_country=gb#documentation. Accessed: 2016-09-08.

[154] N. Jamil, S. Smith, Y. Yang, J. Jia, P. Bagnaninchi, and E. Gonzalez-Fernandez, "Design and fabrication of microelectrodes for electrical impedance tomography of cell spheroids," *IECBES 2016 - IEEE-EMBS Conference on Biomedical Engineering and Sciences*, pp. 426–431, 2017.

[155] A. Hernández, E. Martró, L. Matas, M. Martín, and V. Ausina, "Assessment of in-vitro efficacy of 1 % Virkon® against bacteria, fungi, viruses and spores by means of AFNOR guidelines," *Journal of Hospital Infection*, vol. 46, pp. 203–209, 2000.

[156] "DMSO/Sodium Bicarbonate IV Therapy." http://medicorcancer.com/dmso-therapy/. Accessed: 2018-17-11.

[157] "Encyclopaedia Britannica, Bacteria-Growth of bacterial populations." https://www.britannica.com/science/bacteria/Growth-of-bacterial-populations. Accessed: 2018-17-11.

[158] C. C. de Carvalho, "Adaptation of rhodococcus erythropolis cells for growth and bioremediation under extreme conditions," *Research in Microbiology*, vol. 163, no. 2, pp. 125 – 136, 2012.